



Measurement of the properties of Higgs boson production at $\sqrt{s} = 13$ TeV in the $H \rightarrow \gamma\gamma$ channel using 139 fb^{-1} of pp collision data with the ATLAS experiment

The ATLAS Collaboration

Measurements of Higgs boson production cross-sections are carried out in the diphoton decay channel using 139 fb^{-1} of pp collision data at $\sqrt{s} = 13$ TeV collected by the ATLAS experiment at the LHC. The analysis is based on the definition of 101 distinct signal regions using machine-learning techniques. The inclusive Higgs boson signal strength in the diphoton channel is measured to be $1.04^{+0.10}_{-0.09}$. Cross-sections for gluon-gluon fusion, vector-boson fusion, associated production with a W or Z boson, and top associated production processes are reported. An upper limit of 10 times the Standard Model prediction is set for the associated production process of a Higgs boson with a single top quark, which has a unique sensitivity to the sign of the top quark Yukawa coupling. Higgs boson production is further characterized through measurements of Simplified Template Cross-Sections (STXS). In total, cross-sections of 28 STXS regions are measured. The measured STXS cross-sections are compatible with their Standard Model predictions, with a p -value of 93%. The measurements are also used to set constraints on Higgs boson coupling strengths, as well as on new interactions beyond the Standard Model in an effective field theory approach. No significant deviations from the Standard Model predictions are observed in these measurements, which provide significant sensitivity improvements compared to the previous ATLAS results.

Contents

1	Introduction	3
2	ATLAS detector	4
3	Data and simulation samples	5
3.1	Data	5
3.2	Simulation samples	5
4	Event reconstruction and selection	7
4.1	Photon reconstruction and identification	7
4.2	Event selection and selection of the diphoton primary vertex	8
4.3	Reconstruction and selection of hadronic jets, b -jets, leptons, top quarks and missing transverse momentum	9
5	Design of the measurement	10
5.1	Overview	10
5.2	Categorization	11
6	Modelling of diphoton mass distributions	20
6.1	Modelling of the signal shape	20
6.2	Modelling of the continuum background shape	21
7	Systematic uncertainties	24
7.1	Experimental systematic uncertainties	24
7.2	Theory modelling uncertainties	26
8	Results	27
8.1	Statistical procedure	28
8.2	Overall Higgs boson signal strength	29
8.3	Production cross-sections	29
8.4	Cross-sections in STXS regions	32
9	Interpretation of the results in the κ-framework	39
10	Interpretation of the results in the Standard Model effective field theory framework	41
10.1	Interpretation framework	41
10.2	Measurements of single SMEFT parameters	43
10.3	Simultaneous measurement of SMEFT parameters	46
11	Conclusion	51
	Appendix	52
A	Additional production mode cross-section and STXS measurement results	53

B	Additional κ-framework interpretations	56
B.1	Parameterization of STXS cross-section parameters and the $H \rightarrow \gamma\gamma$ branching ratio	56
B.2	Parameterization with universal coupling modifiers to weak gauge bosons and fermions	57
B.3	Generic parameterization using ratios of coupling modifiers	58
C	Effective field theory interpretation	60
C.1	Measurement of single SMEFT parameters	60
C.2	Simultaneous measurement of SMEFT parameters	62
C.3	Results including SMEFT propagator corrections	66

1 Introduction

The experimental characterization of the Higgs boson discovered by the ATLAS and CMS experiments [1, 2] is not only crucial for our understanding of the mechanism of electroweak symmetry breaking [3–5] but also for providing insight into physics beyond the Standard Model (SM). Despite a small Higgs boson to diphoton ($H \rightarrow \gamma\gamma$) branching ratio of $(0.227 \pm 0.007)\%$ [6] in the SM, measurements in the diphoton final state have yielded some of the most precise determinations of Higgs boson properties [7–11], thanks to the excellent performance of photon reconstruction and identification with the ATLAS detector.

The signature of the Higgs boson in the diphoton final state is a narrow peak in the diphoton invariant mass ($m_{\gamma\gamma}$) distribution with a width consistent with detector resolution, rising above a smoothly falling background. The diphoton mass resolution for such a resonance is typically between 1 GeV and 2 GeV, depending on the event kinematics. The mass and event rate of the Higgs boson signal can be extracted through fits of the $m_{\gamma\gamma}$ distribution. Properties of the Higgs boson have been studied extensively in the diphoton final state by the ATLAS and CMS experiments [10–19].

This paper reports measurements of Higgs boson production cross-sections in the diphoton decay channel, using a data set of proton–proton collisions at $\sqrt{s} = 13$ TeV collected by the ATLAS experiment from 2015 to 2018, a period known as Run 2 of the Large Hadron Collider (LHC). The integrated luminosity of this data set is 139 fb^{-1} [20, 21], a roughly fourfold increase compared to the data set used in the previous ATLAS publication of such measurements in the diphoton channel [10]. Apart from the increased data set size, the most significant improvement in the sensitivity is due to redesigned and refined event selection and categorization techniques compared to Ref. [10]. Uncertainties on the modeling of continuum background have been reduced through the use of a smoothing procedure based on a Gaussian kernel [22]. The performance of the reconstruction and selection of the physics objects used in these measurements has also been generally improved.

The analysis is optimized to measure production cross-sections in the Simplified Template Cross-Section (STXS) framework [6, 23–25], in which the Higgs boson production phase space is partitioned by production process as well as by kinematic and event properties. By combining several STXS regions, the analysis provides strong sensitivity to the cross-sections of the main Higgs boson production modes, gluon-gluon fusion (ggF), vector-boson fusion (VBF), and associated production with a vector boson (VH where $V = W$ or Z), or a top quark pair ($t\bar{t}H$). The analysis is furthermore specifically optimized for the detection of single-top associated production of the Higgs boson (tH), which has a unique sensitivity to the sign of the top-quark Yukawa coupling. While the analysis does not reach sensitivity to the small tH event rate predicted by the SM, it can set constraints on enhanced tH rates due to potential effects from physics beyond the Standard Model (BSM). A measurement of the inclusive Higgs boson production rate within

$|y_H| < 2.5$ in the diphoton channel is also reported. Thanks to the increased integrated luminosity and an improved analysis method, a total of 28 STXS regions are measured in this analysis, compared to 10 in Ref. [10]. Uncertainties and correlations of the production mode cross-section measurements are reduced, and in particular, the uncertainties in the measurements of VH and top-associated production modes are reduced by more than a factor of four.

Two sets of interpretations of these measurements are also performed to provide constraints on potential effects arising from BSM physics: one in terms of Higgs boson coupling strengths within the κ -framework [6], and the other in terms of Wilson coefficients describing potential BSM interactions in the context of a Standard Model effective field theory (SMEFT) model [26–28].

This paper is organized as follows. Section 2 describes the ATLAS detector, Section 3 details the data and Monte Carlo simulation samples used in this analysis, Section 4 explains the object reconstruction and event selection. The design of the measurement is discussed in Section 5, and the modelling of the diphoton mass distribution is discussed in Section 6. Systematic uncertainties are described in Section 7, and Section 8 presents the measurement results. Sections 9 and 10 respectively report the results of interpretations in the context of the κ -framework and the SMEFT model. Conclusions are presented in Section 11.

2 ATLAS detector

The ATLAS detector [29] at the LHC covers nearly the entire solid angle around the collision point.¹ It consists of an inner tracking detector surrounded by a thin superconducting solenoid, electromagnetic and hadronic calorimeters, and a muon spectrometer incorporating three large superconducting toroidal magnets.

The inner-detector system (ID) is immersed in a 2 T axial magnetic field and provides charged-particle tracking in the range $|\eta| < 2.5$. The high-granularity silicon pixel detector covers the vertex region and typically provides four measurements per track, the first hit normally being in the insertable B-layer installed before Run 2 [30, 31]. It is followed by the silicon microstrip tracker, which usually provides eight measurements per track. These silicon detectors are complemented by the transition radiation tracker (TRT), which enables radially extended track reconstruction up to $|\eta| = 2.0$. The TRT also provides electron identification information based on the fraction of hits (typically 30 in total) above a higher energy-deposit threshold corresponding to transition radiation.

The calorimeter system covers the pseudorapidity range $|\eta| < 4.9$. Within the region $|\eta| < 3.2$, electromagnetic calorimetry is provided by barrel and endcap high-granularity lead/liquid-argon (LAr) calorimeters, with an additional thin LAr presampler covering $|\eta| < 1.8$ to correct for energy loss in material upstream of the calorimeters. Hadronic calorimetry is provided by the steel/scintillator-tile calorimeter, segmented into three barrel structures within $|\eta| < 1.7$, and two copper/LAr hadronic endcap calorimeters. The solid angle coverage is completed with forward copper/LAr and tungsten/LAr calorimeter modules optimized for electromagnetic and hadronic measurements respectively.

¹ ATLAS uses a right-handed coordinate system with its origin at the nominal interaction point (IP) in the centre of the detector and the z -axis along the beam pipe. The x -axis points from the IP to the centre of the LHC ring, and the y -axis points upwards. Cylindrical coordinates (r, ϕ) are used in the transverse plane, ϕ being the azimuthal angle around the z -axis. The pseudorapidity is defined in terms of the polar angle θ as $\eta = -\ln \tan(\theta/2)$. Angular distance is measured in units of $\Delta R \equiv \sqrt{(\Delta\eta)^2 + (\Delta\phi)^2}$.

The muon spectrometer (MS) comprises separate trigger and high-precision tracking chambers measuring the deflection of muons in a magnetic field generated by superconducting air-core toroids. The field integral of the toroids ranges between 2.0 and 6.0 T·m across most of the detector. A set of precision chambers covers the region $|\eta| < 2.7$ with three layers of monitored drift tubes, complemented by cathode-strip chambers in the forward region, where the background is highest. The muon trigger system covers the range $|\eta| < 2.4$ with resistive-plate chambers in the barrel, and thin-gap chambers in the endcap regions.

Interesting events are selected to be recorded by the first-level trigger system implemented in custom hardware, followed by selections made by algorithms implemented in software in the high-level trigger [32]. The first-level trigger accepts events from the 40 MHz bunch crossings at a rate below 100 kHz, which the high-level trigger reduces in order to record events to disk at about 1 kHz. An extensive software suite [33] is used in the reconstruction and analysis of real and simulated data, in detector operations, and in the trigger and data acquisition systems of the experiment.

3 Data and simulation samples

3.1 Data

This study uses a data set of $\sqrt{s} = 13$ TeV proton–proton collisions recorded by the ATLAS detector during a period ranging from 2015 to 2018, corresponding to Run 2 of the LHC. After data quality requirements [34] are applied to ensure that all detector components are in good working condition, the data set amounts to an integrated luminosity of $139.0 \pm 2.4 \text{ fb}^{-1}$ [20, 21]. The mean number of interactions per bunch crossing, averaged over all colliding bunch pairs, was $\langle \mu \rangle = 33.7$ for this data set.

Events are selected if they pass either a diphoton or single-photon trigger. The diphoton trigger has transverse energy thresholds of 35 GeV and 25 GeV for the leading and subleading photon candidates, respectively [35], with photon identification selections based on calorimeter shower shape variables. In 2015–2016, a *loose* photon identification requirement was used in the trigger, while in 2017–2018, a tighter requirement was used to cope with higher instantaneous luminosity. The single-photon trigger requires the transverse energy of the leading photon be greater than 120 GeV in data collected between 2015 and 2017, with the threshold rising to 140 GeV for data collected in 2018. The photon candidate used in the trigger decision is required to pass the *loose* photon identification requirement mentioned above. On average, the trigger efficiency is greater than 98% for events that pass the diphoton event selection described in Section 4. The addition of the single-photon trigger improves the selection efficiency by 1% overall, and by up to 2% for high- p_T Higgs boson candidates.

3.2 Simulation samples

Major Higgs boson production processes, including ggF, VBF, VH , $t\bar{t}H$, and $b\bar{b}H$, were generated using POWHEG BOX v2 [36–39]. The ggF simulation achieves next-to-next-to-leading-order (NNLO) accuracy for inclusive ggF observables by reweighting the Higgs boson rapidity spectrum in HJ-MiNLO [40–42] to that of HNNLO [43]. The Higgs boson transverse momentum spectrum obtained with this sample is found to be compatible with the fixed-order HNNLO calculation and the HRES 2.3 calculation [44, 45] performing resummation at next-to-next-to-leading-logarithm accuracy matched to a NNLO fixed-order calculation (NNLL+NNLO). The VBF process was simulated at next-to-leading-order (NLO) accuracy in QCD. The

simulation of the WH and $qq/qg \rightarrow ZH$ processes is accurate to NLO in QCD with up to one extra jet in the event, while the simulation for the $gg \rightarrow ZH$ process was performed at leading order in QCD. The $t\bar{t}H$ and $b\bar{b}H$ processes were simulated at NLO in the strong coupling constant α_s in the five-flavour scheme. The PDF4LHC15 sets [46] of parton distribution functions (PDFs) were used for all the processes listed above. The NNLO set was used for ggF, and the NLO set for other processes.

The $tHqb$ (tHW) samples were produced with MADGRAPH5_AMC@NLO 2.6 [47] in the four-flavour (five-flavour) scheme with the NNPDF3.0_{NNLO} PDF. The same flavour scheme was used in the matrix element calculation and the PDF. The top quark and W boson decays were handled by MADSPIN [48] to account for spin correlations in the decay products. The overlap of the tHW process with $t\bar{t}H$ at NLO was removed by using a diagram removal technique [49, 50]. The $pp \rightarrow tHb$ process has a small cross-section and was not considered in the modelling of tH production.

All generated events for the processes listed above were interfaced to PYTHIA 8.2 [51, 52] to model parton showering, hadronization and the underlying event using the AZNLO set of parameter values tuned to data [53]. The decays of bottom and charm hadrons were simulated using the EVTGEN 1.6.0 program [54]. Systematic uncertainties related to the signal modeling are estimated using a set of samples where HERWIG7 [55, 56] is used for parton showering.

Major Higgs boson production processes were also simulated using alternative generator programs. The ggF process was also generated with MADGRAPH5_AMC@NLO, using an NLO-accurate matrix element for up to two additional partons and applying the FxFx merging scheme to obtain an inclusive sample [47, 57]. The generation used an effective vertex with a point-like coupling between the Higgs boson and gluons in the infinite top-mass limit. The events were showered using PYTHIA 8.2 with the A14 set of tuned parameters [58]. The VBF alternative sample was generated with MADGRAPH5_AMC@NLO at NLO accuracy in the matrix element. It was then showered with HERWIG 7.1.6. The VH alternative sample was simulated with MADGRAPH5_AMC@NLO, and the simulation is accurate to NLO in QCD for zero or one additional parton merged with the FxFx merging scheme. The $gg \rightarrow ZH$ process was also simulated at LO with MADGRAPH5_AMC@NLO and showered with PYTHIA 8.2. The $t\bar{t}H$ alternative sample was simulated with MADGRAPH5_AMC@NLO at NLO and the parton showering was performed with PYTHIA 8.2.

All Higgs boson signal events were generated with a Higgs boson mass (m_H) of 125 GeV and an intrinsic width (Γ_H) of 4.07 MeV [59]. The cross-sections of Higgs production processes are reported for a centre-of-mass energy of $\sqrt{s} = 13$ TeV and a Higgs boson with mass $m_H = 125.09$ GeV [60]. These cross-sections [6, 50, 61–93], shown in Table 1, are used together with the Higgs boson branching ratio to diphotons [6, 94–99] to normalize the simulated signal events.

Prompt diphoton production ($\gamma\gamma$) was simulated with the SHERPA 2.2.4 [100] generator. In this set-up, NLO-accurate matrix elements for up to one parton, and LO-accurate matrix elements for up to three partons were calculated with the Comix [101] and OPENLOOPS [102–104] libraries. They were matched with the SHERPA parton shower [105] using the MEPS@NLO prescription [106–109] with a dynamic merging cut [110] of 10 GeV. Photons were required to be isolated according to a smooth-cone isolation criterion [111]. Samples were generated using the NNPDF3.0_{NNLO} PDF set [112], along with the dedicated set of tuned parton-shower parameters developed by the SHERPA authors.

The production of $V\gamma\gamma$ events was simulated with the SHERPA 2.2.4 [100] generator. QCD LO-accurate matrix elements for up to one additional parton emission were matched and merged with the SHERPA parton shower based on the Catani–Seymour dipole factorization [101, 105] using the MEPS@LO prescription [106–109]. Samples were generated using the same PDF set and parton-shower parameters as the $\gamma\gamma$ sample. The production of $t\bar{t}\gamma\gamma$ events was modelled using the MADGRAPH5_AMC@NLO 2.3.3

generator at LO with the NNPDF2.3LO [113] PDF. The parton-showering and underlying-event simulation were performed using PYTHIA 8.2.

The effect of multiple interactions in the same and neighbouring bunch crossings (pile-up) was modelled by overlaying the original hard-scattering event with simulated inelastic proton–proton (pp) events generated with PYTHIA 8.1 using the NNPDF2.3LO PDF set and the A3 tune [114]. The generated signal and background events were passed through a simulation of the ATLAS detector [115] using the GEANT4 toolkit [116]. The only exception is the prompt diphoton sample, where the generated events were processed using a fast simulation of the ATLAS detector [117], where the full simulation of the calorimeter is replaced with a parameterization of the calorimeter response.

A summary of the simulated signal and background samples is shown in Table 1.

Table 1: Event generators and PDF sets used to model signal and background processes. The cross-sections of Higgs boson production processes [6, 61, 62, 68, 75–77, 80, 82, 86–93, 118, 119] are reported for a centre-of-mass energy of $\sqrt{s} = 13$ TeV and a Higgs boson mass of $m_H = 125.09$ GeV. The order of the calculated cross-section is reported in each case. The cross-sections for the background processes are omitted, since the background normalization is determined in fits to the data.

Process	Generator	Showering	PDF set	σ [pb] $\sqrt{s} = 13$ TeV	Order of σ calculation
ggF	NNLOPS	PYTHIA 8.2	PDF4LHC15	48.5	N ³ LO(QCD)+NLO(EW)
VBF	POWHEG BOX	PYTHIA 8.2	PDF4LHC15	3.78	approximate-NNLO(QCD)+NLO(EW)
WH	POWHEG BOX	PYTHIA 8.2	PDF4LHC15	1.37	NNLO(QCD)+NLO(EW)
$qq/qg \rightarrow ZH$	POWHEG BOX	PYTHIA 8.2	PDF4LHC15	0.76	NNLO(QCD)+NLO(EW)
$gg \rightarrow ZH$	POWHEG BOX	PYTHIA 8.2	PDF4LHC15	0.12	NLO(QCD)
$t\bar{t}H$	POWHEG BOX	PYTHIA 8.2	PDF4LHC15	0.51	NLO(QCD)+NLO(EW)
$b\bar{b}H$	POWHEG BOX	PYTHIA 8.2	PDF4LHC15	0.49	NNLO(QCD)
$tHqb$	MADGRAPH5_AMC@NLO	PYTHIA 8.2	NNPDF3.0NNLO	0.074	NLO(QCD)
tHW	MADGRAPH5_AMC@NLO	PYTHIA 8.2	NNPDF3.0NNLO	0.015	NLO(QCD)
$\gamma\gamma$	SHERPA	SHERPA	NNPDF3.0NNLO		
$V\gamma\gamma$	SHERPA	SHERPA	NNPDF3.0NNLO		
$t\bar{t}\gamma\gamma$	MADGRAPH5_AMC@NLO	PYTHIA 8	NNPDF2.3LO		

4 Event reconstruction and selection

Events in this analysis are selected using the following procedure. Reconstructed photon candidates are first required to satisfy a set of *preselection*-level identification criteria. The two highest- p_T preselected photons are then used to define the diphoton system, and an algorithm is used to identify the event primary vertex. Finally, the photons are required to satisfy isolation criteria and additional identification criteria. Jets (including b -tagged jets), muons, electrons, and missing transverse energy (E_T^{miss}) are used in the analysis in order to categorize diphoton events and measure Higgs boson properties.

4.1 Photon reconstruction and identification

Photons are reconstructed from energy deposits in the calorimeter that are formed using a dynamical, topological cell-clustering algorithm [120]. The photon candidate is classified as *converted* if it is matched to either two tracks forming a conversion vertex, or one track with the signature of an electron track without

hits in the innermost pixel layer; otherwise, it is classified as *unconverted*. The photon candidate’s energy is calibrated using a procedure described in Ref. [120].

Reconstructed photons must satisfy $|\eta| < 2.37$ in order to fall inside the region of the electromagnetic (EM) calorimeter with a finely segmented first layer, and outside the range $1.37 < |\eta| < 1.52$ corresponding to the transition region between the barrel and endcap EM calorimeters. Photon candidates are distinguished from jet backgrounds using identification criteria based on calorimeter shower shape variables [120]. A *loose* working point is used for preselection, and the final selection of photon candidates is made using a *tight* selection. The efficiency of the *tight* identification for unconverted (converted) photons ranges from about 84% (85%) at $p_T = 25$ GeV to 94% (98%) for $p_T > 100$ GeV.

The final selection of photons includes both calorimeter- and track-based isolation requirements to further suppress jets misidentified as photons. The calorimeter isolation variable is defined as the total energy of calorimeter clusters in a cone of size $\Delta R = 0.2$ around the photon candidate, excluding the energy in a fixed-size window containing the photon shower; a correction is applied for leakage of photon energy from this window into the surrounding cone [120]. Contributions from pile-up and the underlying event are subtracted [120–124]. The calorimeter-based isolation must be less than 6.5% of the photon transverse energy for each photon candidate. The track-based isolation variable is defined as the scalar sum of the transverse momenta of tracks within a $\Delta R = 0.2$ cone around the photon candidate. The tracks considered in the isolation variable are restricted to those with $p_T > 1$ GeV that are matched to the selected diphoton primary vertex described below and not associated with the photon conversion vertex, if present. Each photon must have a track isolation less than 5% of the photon transverse energy.

4.2 Event selection and selection of the diphoton primary vertex

Events are selected by first requiring at least two photons satisfying the *loose* identification preselection criteria. The two highest- p_T preselected photons are designated as the candidates for the diphoton system. The *diphoton primary vertex* of the event is determined using a neural-network algorithm [7]. Information about the reconstructed vertices in the event and the trajectories of the two photons, measured using the depth segmentation of the calorimeter and completed by photon conversion information if present, is used as input to the network. [7]. The algorithm is trained on simulation and leads to an 8% improvement in the mass resolution for inclusive Higgs boson production, relative to the default primary vertex selection [125], and results in better analysis sensitivity. Its performance was validated using studies of $Z \rightarrow ee$ events in data and simulation, in which the electrons were treated as photon candidates and their track information ignored. This performance is weakly dependent on the event pile-up, and its residual dependence is well described by simulation.

The two preselected photon candidates are required to satisfy the *tight* identification criteria and the isolation selection described above. Finally, the highest- p_T and second-highest- p_T photon candidates are required to satisfy $p_T/m_{\gamma\gamma} > 0.35$ and 0.25, respectively. As discussed in Sections 5 and 6, events that fail the tight identification or the isolation selection are used as a control sample for background estimation and modelling purposes.

The trigger, photon and event selections described above are used to define the events that are selected for further analysis for Higgs boson properties. In total, about 1.2 million events are selected in this data set with a diphoton invariant mass between 105 and 160 GeV. The predicted efficiency for a SM Higgs boson signal with $|y_H| < 2.5$ is 39%.

4.3 Reconstruction and selection of hadronic jets, b -jets, leptons, top quarks and missing transverse momentum

Jets are reconstructed using a particle-flow algorithm [126] from noise-suppressed positive-energy topological clusters [127] in the calorimeter using the anti- k_r algorithm [128, 129] with a radius parameter $R = 0.4$. Energy deposited in the calorimeter by charged particles is subtracted and replaced by the momenta of tracks that are matched to those topological clusters. The jet four-momentum is corrected for the non-compensating calorimeter response, signal losses due to noise threshold effects, energy lost in non-instrumented regions, and contributions from pile-up [130]. Jets are required to have $p_T > 25$ GeV and an absolute value of rapidity y less than 4.4. A jet-vertex-tagger (JVT) multivariate discriminant [131] is applied to jets with $p_T < 60$ GeV and $|\eta| < 2.4$, to suppress jets from pile-up; in the $|\eta|$ range beyond 2.5, a forward version of the JVT [132] is applied to jets with $p_T < 120$ GeV. Jets with $|\eta| < 2.5$ containing b -hadrons are identified using the DL1r b -tagging algorithm and its 60%, 70%, 77% and 85% efficiency working points, which are combined into a pseudo-continuous b -tagging score [133].

Electrons are reconstructed by matching tracks in the ID to topological clusters formed using the same dynamical, topological cell-clustering algorithm as in the photon reconstruction [120]. Electron candidates are required to have $p_T > 10$ GeV and $|\eta| < 2.47$, excluding the EM calorimeter transition region of $1.37 < |\eta| < 1.52$, and must satisfy the *medium* identification selection based on a likelihood discriminant using calorimeter shower shapes and track parameters [120]. Isolation criteria are applied to electrons, using calorimeter- and track-based information. The reconstructed track matched to the electron candidate must be consistent with the diphoton vertex, which is ensured by requiring its longitudinal impact parameter z_0 relative to the vertex to satisfy $|z_0 \sin \theta| < 0.5$ mm. In addition, the electron track's transverse impact parameter with respect to the beam axis divided by its uncertainty, $|d_0|/\sigma_{d_0}$, must be less than 5.

Muons are reconstructed by matching tracks from the MS and ID subsystems. In the pseudorapidity range of $2.5 < |\eta| < 2.7$, muons without an ID track but whose MS track is compatible with originating from the interaction point are also considered. Muon candidates are required to have $p_T > 10$ GeV and $|\eta| < 2.7$, and must satisfy the *medium* identification requirements [134]. Muons are required to satisfy calorimeter- and track-based isolation requirements that are 95%–97% efficient for muons with $10 \leq p_T \leq 60$ GeV and 99% efficient for $p_T > 60$ GeV. Muon tracks must satisfy $|z_0 \sin \theta| < 0.5$ mm and $|d_0|/\sigma_{d_0} < 3$.

Top quark candidates are reconstructed and identified using a boosted decision tree (BDT) discriminant, using the same procedure as in Ref. [14] applied to the particle-flow jets described above. The BDT targets both leptonic top quark signatures, in which the top quark decays to a W boson that decays to an electron or a muon, and hadronic signatures in which the W boson decays to hadrons or to a τ -lepton.

An overlap removal procedure is performed in order to avoid double-counting objects. First, electrons overlapping with any photons ($\Delta R < 0.4$) that pass the isolation and identification requirements are removed. Jets overlapping with the selected photons ($\Delta R < 0.4$) and electrons ($\Delta R < 0.2$) are removed. In the calculation of the ΔR between a jet and another object, the jet rapidity is used. Electrons overlapping with the remaining jets ($\Delta R < 0.4$) are removed to match the requirements imposed when measuring isolated electron efficiencies. Finally, muons overlapping with photons or jets ($\Delta R < 0.4$) are removed.

The missing transverse momentum is defined as the negative vector sum of the transverse momenta of the selected photon, electron, muon and jet objects, plus the transverse momenta of remaining low- p_T particles, estimated using tracks matched to the diphoton primary vertex but not assigned to any of the selected objects [135]. Its magnitude is denoted by E_T^{miss} .

Finally, an event veto is applied to suppress the overlap between the selection described here and that of the search for Higgs boson pair production in the $b\bar{b}\gamma\gamma$ final state [136], to facilitate the statistical combination of the two results at a later stage. Most of the vetoed events would enter the $t\bar{t}H$ and tH classes defined in Section 5. This veto has a negligible impact on the analysis results.

5 Design of the measurement

5.1 Overview

The analysis is designed to measure the production cross-sections in the STXS framework [24]. The regions considered in this paper are based on the Stage 1.2 STXS binning. They are defined in the Higgs boson rapidity range of $|y_H| < 2.5$, separately for mutually exclusive Higgs boson production processes: the $gg \rightarrow H$ process, which includes both ggF production and $gg \rightarrow ZH$ production followed by a hadronic decay of the Z boson; the electroweak $qq' \rightarrow Hqq'$ process, encompassing both VBF production and $q\bar{q}' \rightarrow VH$ production followed by a hadronic decay of the vector boson; the $V(\rightarrow \text{leptons})H$ process, corresponding to $pp \rightarrow VH$ production followed by a leptonic decay of the vector boson (in the case of ZH , including both decays to charged leptons and to neutrinos); and top-associated $t\bar{t}H$ and tH production. The Higgs boson decay information is not used in the definition of STXS regions. For each process, non-overlapping fiducial regions are defined. These are based on the kinematics of the Higgs boson and of the associated jets and W and Z bosons, as well as the numbers of jets, leptons and top quarks. Jets are reconstructed at the particle level from all stable particles with a lifetime greater than 10 ps, excluding the decay products of the Higgs boson and leptons from W and Z boson decays, using the anti- k_t algorithm with a jet radius parameter $R = 0.4$, and must have a transverse momentum larger than 30 GeV.

Compared to the Stage 1.2 STXS definition, two sets of modified STXS regions are defined: a set of *analysis regions* which is used in the design of the analysis strategy, and is defined below; and a set of *measurement regions*, in which some analysis regions are merged, which are used to present the measurement results and are defined at the beginning of Section 8.4. The 45 STXS analysis regions are listed in Figure 1. They follow the Stage 1.2 definitions with the following modifications:

- The $b\bar{b}H$ production mode is experimentally difficult to separate from $gg \rightarrow H$, and these two production modes have similar selection acceptance and efficiency. The two modes are therefore measured as a single process, with each STXS region of the combined process corresponding to the sum of $gg \rightarrow H$ and $b\bar{b}H$ contributions.
- For $gg \rightarrow H$ and $qq' \rightarrow Hqq'$ processes, STXS regions requiring two or more jets are not split by the transverse momentum of the system consisting of the Higgs boson and two highest- p_T jets, p_T^{Hjj} , since the measurement does not provide sufficient sensitivity to this split. In addition, the STXS region defined by $m_{jj} \geq 700$ GeV, where m_{jj} is the invariant mass of the two highest- p_T jets, is split into two bins corresponding to m_{jj} above or below 1 TeV. An additional splitting at $m_{jj} = 700$ GeV is also introduced in the $p_T^H \geq 200$ GeV region of the $qq' \rightarrow Hqq'$ process.
- The $gg \rightarrow ZH$ and $q\bar{q} \rightarrow ZH$ production modes with a leptonic Z boson decay similarly cannot be distinguished by the analysis selections, and are therefore considered as a single $pp \rightarrow ZH$ process. In addition, each region of this process is split into separate regions for charged ($pp \rightarrow H\ell\ell$) and neutral ($pp \rightarrow H\nu\bar{\nu}$) dileptons.

- Production of tH is split into separate $pp \rightarrow tHW$ and $pp \rightarrow tHqb$ contributions, since the two processes have different acceptances for the analysis selections. The s -channel $pp \rightarrow tHb$ process is neglected due to its small cross-section.
- The $V(\rightarrow \text{leptons})H$ regions are not separated according to the number of jets in the event.

5.2 Categorization

The events passing the selection described in Section 4 are classified into mutually exclusive event *categories*, each targeted towards a particular STXS region.² This follows a technique similar to the one used in Ref. [10], but the definition of the categories has been improved significantly. The categorization in Ref. [10] was implemented sequentially over production modes, in order of increasing cross-section. In the present analysis, the categories are instead defined using a unified technique covering all processes simultaneously, and are designed to maximize a global criterion of sensitivity in the measurement of the cross-sections in all STXS regions.

The technique proceeds in several steps. First, simulated Higgs boson production event samples are used to train a multiclass BDT to separate signal events coming from different STXS regions. This multiclass BDT classifier outputs one discriminant value for each STXS region. The output discriminant values are then used to assign signal events to various STXS *classes*. Each of these detector-level classes targets events from a particular STXS region defined at the particle level. Finally, each class is further divided into multiple categories using a binary multivariate classifier. This classifier is trained to separate signal from continuum background and Higgs boson events from other STXS regions in each class.

The inputs to all the classifiers are variables describing the kinematic and identification properties of the reconstructed particles presented in Section 4:

- the kinematics of the diphoton system;
- the numbers of reconstructed jets, b -jets, electrons, muons and top quarks;
- the kinematics of the system composed of the two photons and one or more jets, if jets are present, and of the system composed of the two highest- p_T jets in the event, if at least two jets are present;
- the kinematics of the reconstructed leptons and top quarks;
- the reconstruction score of the top quarks, computed from the kinematics of the top quark decay products as described in Ref. [14];
- other event quantities such as the missing transverse momentum.

Among the top-associated production processes, the $tHqb$ mode can be separated from both $t\bar{t}H$ and tHW due to differences in kinematics and event topology, in particular the presence of a forward jet and the absence of a second well reconstructed top quark candidate in the event.

In order to avoid distorting the smoothly falling shapes of the background $m_{\gamma\gamma}$ distributions, any variable found to have a linear correlation coefficient of 5% or more with $m_{\gamma\gamma}$ in the signal or background training samples is removed from the list of inputs to the binary classifiers. The training variables used in the analysis are summarized in Tables 2 and 3.

² In this paper, *categories* refers to event groupings defined from reconstructed quantities, while *regions* refers to the particle-level selections defined in the STXS framework.

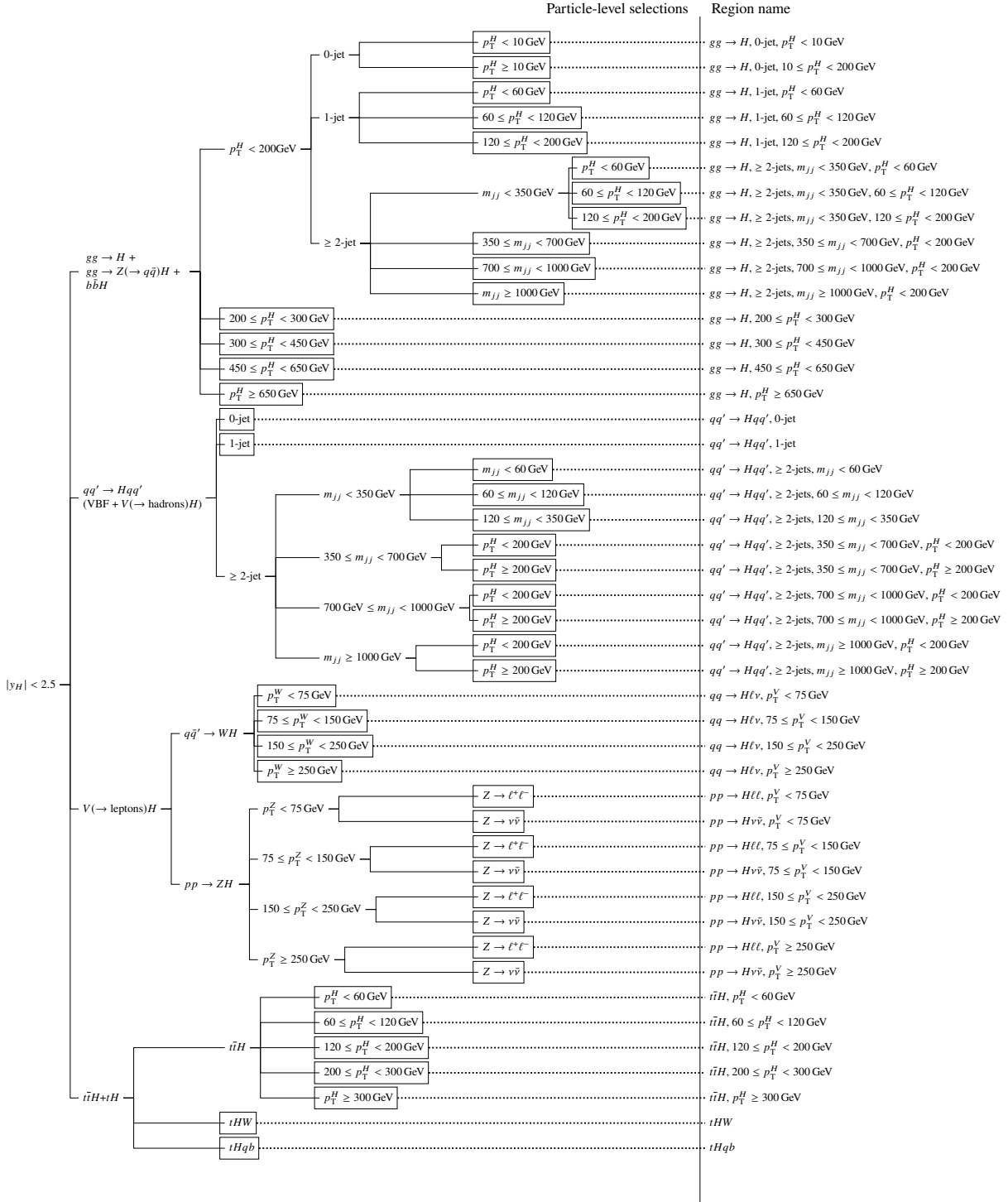


Figure 1: Summary of the STXS regions considered in the analysis design. The left part of the plot shows the selections applied to particle-level quantities in simulated signal events, with the selections applied sequentially along the branches of the graph. The final selection for each region is indicated by a box, and the name of each region, used in the rest of this paper, is shown on the right.

Table 2: Training variables used as input to the multiclass BDT. The dagger symbol † denotes variables that have two versions with different jet p_T requirements. One version of such a variable is defined using jets with $p_T > 25$ GeV, and the other version is defined using jets with $p_T > 30$ GeV. Both versions are used in the training of the multiclass BDT. The two highest- p_T photons are denoted as γ_1 and γ_2 , the two highest- p_T jets as j_1 and j_2 , the two highest- p_T top quarks as t_1 and t_2 and the most forward jet as j_F . $\Delta R(W, b)$ is the ΔR between the W and b components of a top-quark candidate.

$\eta_{\gamma_1}, \eta_{\gamma_2}, p_T^{\gamma\gamma}, y_{\gamma\gamma},$
$p_{T,jj}^\dagger, m_{jj},$ and $\Delta y, \Delta\phi, \Delta\eta$ between j_1 and $j_2,$
$p_{T,\gamma\gamma j_1}, m_{\gamma\gamma j_1}, p_{T,\gamma\gamma jj}^\dagger, m_{\gamma\gamma jj}$
$\Delta y, \Delta\phi$ between the $\gamma\gamma$ and jj systems,
minimum ΔR between jets and photons,
invariant mass of the system comprising all jets in the event,
dilepton $p_T,$ di- e or di- μ invariant mass (leptons are required to be oppositely charged),
E_T^{miss}, p_T and transverse mass of the lepton + E_T^{miss} system,
p_T, η, ϕ of top-quark candidates, $m_{t_1 t_2}$
Number of jets†, of central jets ($ \eta < 2.5$)†, of b -jets† and of leptons,
p_T of the highest- p_T jet, scalar sum of the p_T of all jets,
scalar sum of the transverse energies of all particles ($\sum E_T$), E_T^{miss} significance,
$\left E_T^{\text{miss}} - E_T^{\text{miss}}(\text{primary vertex with the highest } \sum p_{T,\text{track}}^2) \right > 30 \text{ GeV}$
Top reconstruction BDT of the top-quark candidates,
$\Delta R(W, b)$ of $t_2,$
$\eta_{j_F}, m_{\gamma\gamma j_F}$
Average number of interactions per bunch crossing.

The multiclass BDT used in the initial step of the classification is trained on a data set obtained by merging the ggF, VBF, VH , $t\bar{t}H$ and tH signal samples described in Section 3.2. A weight is applied to the events in each STXS region so that the regions have equal event yields in the training sample. This configuration improves the performance of the discrimination. For each event, the output of the BDT consists of a set of class discriminants y_i , where the index i runs over the 45 STXS regions defined in Table 1. This output is then normalized into the parameters $z_i = \exp(y_i) / \sum_j \exp(y_j)$, a procedure also known as a softmax layer. The training is performed by minimizing the cross-entropy of the z_i with respect to the true STXS region assignments³ using the LightGBM package [137].

A second training phase is then performed to optimize the classification procedure in terms of the analysis sensitivity itself. The sensitivity is estimated as the inverse determinant $|C|^{-1}$ of the covariance matrix of the measurement of the signal event yields in each region. This D -optimality (determinant) criterion leads in particular to a reduction of the expected statistical uncertainty of the measurement, and is suggested by the fact that $|C|^{-1}$ is a known measure of the information provided by the measurement [138]. The classification procedure is performed so that events are assigned to the STXS class i corresponding to the maximum value of $w_i z_i$, where the w_i are a set of per-class weights. These weights are initially set to 1,

³ The cross-entropy loss function is computed as $-\sum_{k=1}^n \omega_k \sum_{i=1}^{45} \delta_{i,k} \ln(z_i)$, where k runs over the n events in the training sample, ω_k are event weights applied to balance the class yields as described in the text, i runs over the classes, and $\delta_{k,i}$ has a value of 1 if class i is the correct assignment for event k , and 0 otherwise.

Table 3: Training variables used for the binary classifiers. The sets of classes to which the classifiers are applied are specified in the first column, and the corresponding variables in each case are listed in the second column. The asterisk symbol * denotes tH training variables that are only used for the classifiers suppressing the continuum background. Other tH training variables are used in all three tH classifiers. The $\gamma\gamma$ and jj notations refer to the systems composed of the two highest- p_T photons and jets, respectively. The two highest- p_T photons are denoted as γ_1 and γ_2 , the two highest- p_T top quarks as t_1 and t_2 , and the most forward jet as j_F . The differences in η and ϕ between γ_1 and γ_2 are denoted respectively as $\Delta\phi_{\gamma\gamma}$ and $\Delta\eta_{\gamma\gamma}$. $\Delta R(W, b)$ is the ΔR between the W and b components of a top-quark candidate.

STXS classes	Variables
Individual STXS classes from $gg \rightarrow H$ $qq' \rightarrow Hqq'$ $qq \rightarrow H\ell\nu$ $pp \rightarrow H\ell\ell$ $pp \rightarrow H\nu\bar{\nu}$	All multiclass BDT variables, $p_T^{\gamma\gamma}$ projected to the thrust axis of the $\gamma\gamma$ system ($p_T^{\gamma\gamma}$), $\Delta\eta_{\gamma\gamma}, \eta^{Z\text{epp}} = \frac{\eta_{\gamma\gamma} - \eta_{jj}}{2}$, $\phi_{\gamma\gamma}^* = \tan\left(\frac{\pi - \Delta\phi_{\gamma\gamma} }{2}\right) \sqrt{1 - \tanh^2\left(\frac{\Delta\eta_{\gamma\gamma}}{2}\right)}$, $\cos\theta_{\gamma\gamma}^* = \left \frac{(E^{\gamma_1 + p_z^{\gamma_1}}) \cdot (E^{\gamma_2 - p_z^{\gamma_2}}) - (E^{\gamma_1 - p_z^{\gamma_1}}) \cdot (E^{\gamma_2 + p_z^{\gamma_2}})}{m_{\gamma\gamma} + \sqrt{m_{\gamma\gamma}^2 + (p_T^{\gamma\gamma})^2}} \right $ Number of electrons and muons.
all $t\bar{t}H$ and tHW STXS classes combined	p_T, η, ϕ of γ_1 and γ_2 , p_T, η, ϕ and b -tagging scores of the six highest- p_T jets, $E_T^{\text{miss}}, E_T^{\text{miss}}$ significance, E_T^{miss} azimuthal angle, Top reconstruction BDT scores of the top-quark candidates, p_T, η, ϕ of the two highest- p_T leptons.
$tHqb$	$p_T^{\gamma\gamma} / m_{\gamma\gamma}, \eta_{\gamma\gamma}$, p_T , invariant mass, BDT score and $\Delta R(W, b)$ of t_1 , p_T, η of t_2 , p_T, η of j_F , Angular variables: $\Delta\eta_{\gamma\gamma t_1}, \Delta\theta_{\gamma\gamma t_2}, \Delta\theta_{t_1 j_F}, \Delta\theta_{t_2 j_F}, \Delta\theta_{\gamma\gamma j_F}$ Invariant mass variables: $m_{\gamma\gamma j_F}, m_{t_1 j_F}, m_{t_2 j_F}, m_{\gamma\gamma t_1}$ Number of jets with $p_T > 25$ GeV, Number of b -jets with $p_T > 25$ GeV*; Number of leptons*, E_T^{miss} significance*

and then iteratively updated so as to maximize $|C|^{-1}$: for each value of the w_i , a simulated data set is generated for each region by mixing events from each signal sample in proportion to their SM production cross-sections, together with a sample of simulated continuum background events normalized to data in the control region $95 \leq m_{\gamma\gamma} < 105$ GeV. A simplified statistical model approximating the full model described in Section 6 is then used to estimate $|C|^{-1}$, and the procedure is iterated until a maximum is found for $|C|^{-1}$.

Figure 2 shows distributions of the weighted multiclass discriminant output $w_i z_i$ for four representative STXS classes, illustrating the discrimination provided by the multiclass BDT. While events with high BDT output values for a given region tend to be selected in the corresponding class, this does not manifest itself as a sharp cut, due to the interplay between the selections for the different classes. Compared to the simple selection based only on the z_i , the selection based on the $w_i z_i$ provides both higher purity and higher

selection efficiency for classes associated with rare processes such as tH , $t\bar{t}H$, VH and VBF, as well as production at high values of p_T^H or m_{jj} . This leads to measurements with generally smaller uncertainties and lower correlations.

This multiclass training allows the selection of target process events that otherwise would fail a requirement based on detector-level quantities corresponding to the STXS region definition. For example, in the STXS region $gg \rightarrow H$, 1-jet, $p_T^H < 60$ GeV, detector-level events that originate from the target process but have no reconstructed jets would fail requirements defined by the number of jets and p_T^H ; however, those events could be selected by the multiclass discriminant. For this STXS region, 20% of events from the target process have no reconstructed jets. The recovery of these events leads to a reduction of about 6% in the measurement uncertainty. It is also robust against pile-up in the determination of jet multiplicity in $gg \rightarrow H$.

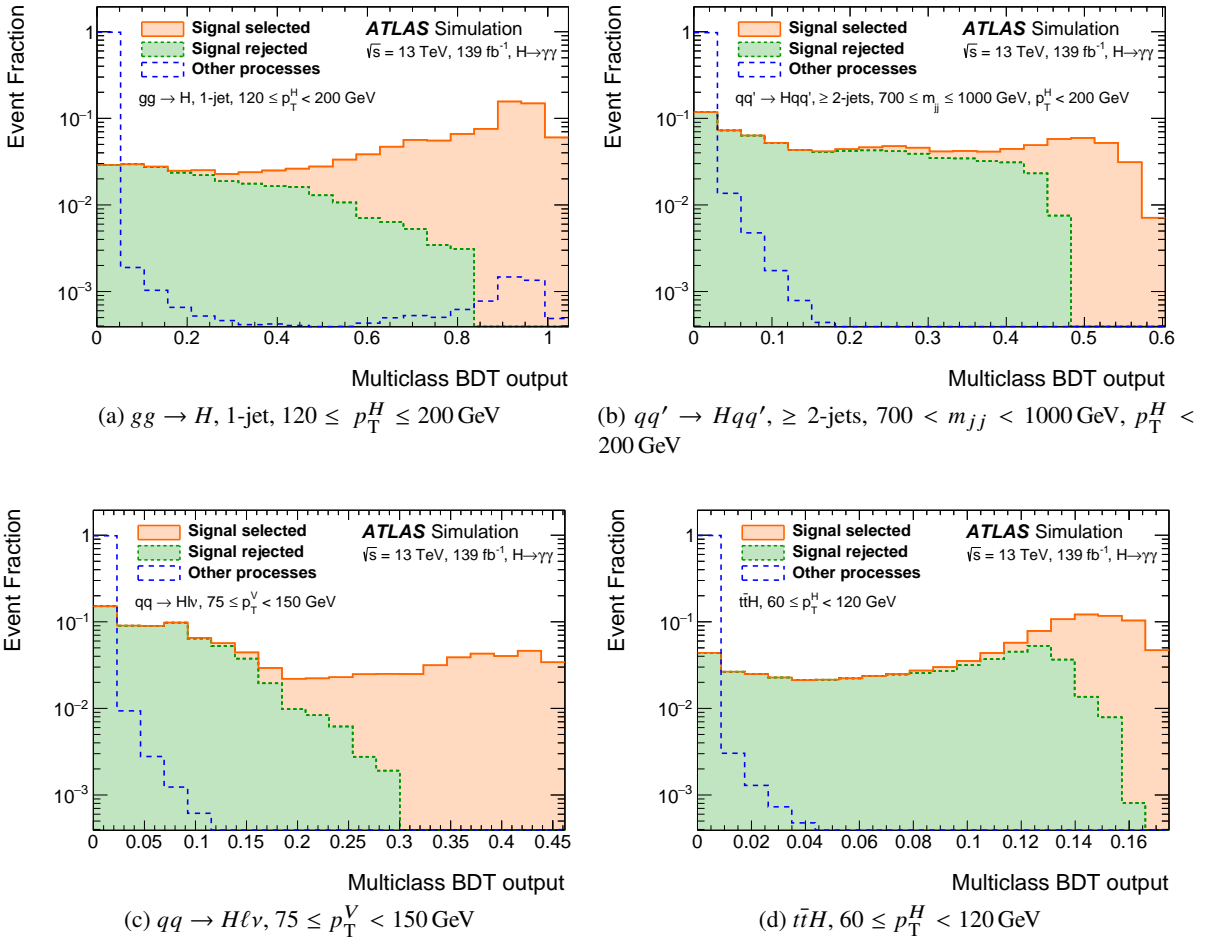


Figure 2: Distributions of the weighted multiclass discriminant output $w_i z_i$, where z_i is the raw discriminant output and w_i the per-class weight defined in the text, for four representative STXS classes. In each plot, the distribution is shown separately for events corresponding to the target STXS region (solid) and events in other STXS regions (long-dashed). The target STXS region is further broken down into the subset of events assigned to the correct class at detector level (orange-solid), and the subset of events that are assigned to other classes (green-dashed). The orange-solid component is stacked on top of the dashed component. An event is assigned to the class with the largest $w_i z_i$ value.

After the classes are defined, binary classifiers are then trained and used to further divide each class into multiple categories, to improve the measurement sensitivity. For each of the classes targeting $gg \rightarrow H$, $qq' \rightarrow Hqq'$ and $V(\rightarrow \text{leptons})H$ processes, a binary BDT classifier is trained to distinguish between simulated signal events of the corresponding STXS region and both simulated continuum background events and Higgs boson events from other STXS regions.

For the $t\bar{t}H$ and tHW classes, a binary BDT classifier is trained to separate $t\bar{t}H$ signal and the continuum background using all events assigned to various $t\bar{t}H$ classes targeting different p_T^H regions. Similarly, a binary BDT classifier is trained to separate tHW signal and the continuum background using events assigned to the tHW class.

To enhance the sensitivity to the sign of the top-Yukawa coupling modifier κ_t (defined in more detail in Section 9), a specialization is introduced for the $tHqb$ class. First, the class is divided into two sub-classes based on a neural-network (NN) binary classifier that separates $tHqb$ production with $\kappa_t = 1$ from $tHqb$ production with $\kappa_t = -1$. In each sub-class, the events are then further divided into categories based on NN binary classifiers trained to separate the corresponding $tHqb$ signal events from continuum background events and Higgs boson events from other processes.

The binary classifiers used to suppress continuum background processes in the $t\bar{t}H$, tHW , and $tHqb$ classes are trained on events from control regions in data, which provide larger event yields than the available simulated background samples. These regions are defined using the same selections as the classes, but reversing the photon identification requirement, the photon isolation requirement, or both.

In each class, events are then assigned to categories corresponding to ranges of binary classifier output values. Up to three categories are defined in this way, depending on the targeted STXS region. The category boundaries in the BDT output are determined by scanning over all possible values and finding the set that maximizes the sum in quadrature of the expected significance values in all categories. The expected significance is computed as $Z = \sqrt{2((S+B)\ln(1+S/B) - S)}$ [139], where S and B are the expected signal yield and background yield in the targeted STXS region in the smallest range of $m_{\gamma\gamma}$ around the signal peak position that contains 90% of signal events. The background B includes contributions from continuum background and Higgs boson events from other STXS regions. The continuum background is computed from the $m_{\gamma\gamma}$ distribution in simulation, normalized to the data control region $95 \leq m_{\gamma\gamma} < 105$ GeV. A class is split into two categories if this leads to an improvement of more than 5% in the expected significance, and into three categories if a further improvement of at least 5% relative to the two-category configuration can be achieved. The categories are referred to as *High-purity*, *Med-purity* and, in the case of a 3-category split, *Low-purity* in order of decreasing BDT output values. No events are removed at the categorization stage, since the lower-purity categories bring non-negligible contributions to the analysis sensitivity. Figure 3 shows binary BDT discriminant distributions as well as category boundaries for four representative STXS classes.

The categorization for the $tHqb$ class follows a different procedure, which aims to maximize both the sensitivity to a $tHqb$ signal and the sensitivity to the sign of κ_t . A boundary is placed in the NN classifier that separates the $tHqb$ signal with $\kappa_t = 1$ from the $tHqb$ signal with $\kappa_t = -1$. Different boundaries are also placed in the two binary NN classifiers that separate $tHqb$ signals from continuum background. These boundaries are determined simultaneously. Finally, a *low-purity top* category is formed by grouping together the events with the lowest binary classifier output values in both the $t\bar{t}H$ and tH classes.

The entire categorization procedure results in the definition of 101 categories in total. The expected signal and background yields in these categories are summarized in Table 4. The expected signal purity, defined as the expected signal yield divided by the expected yield from both the signal and background processes,

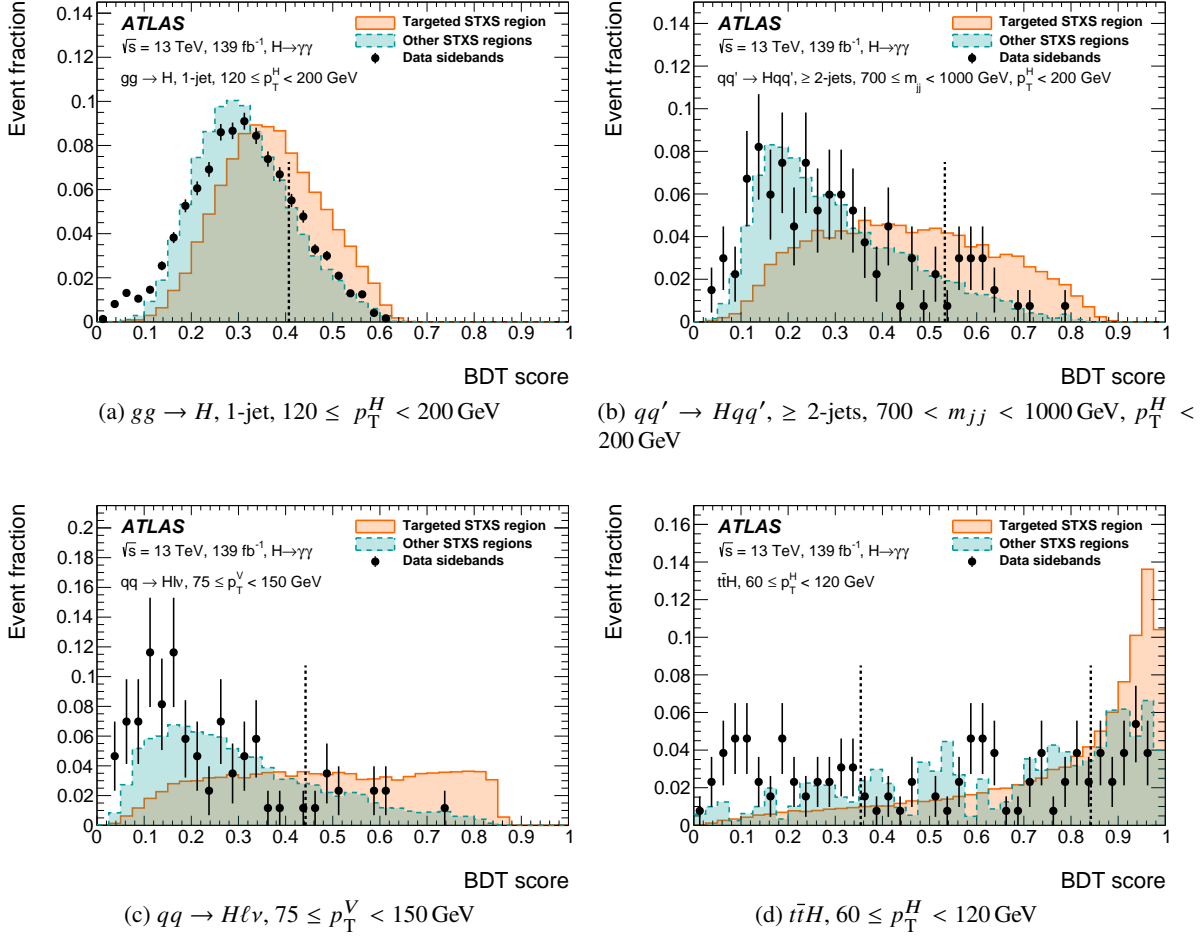


Figure 3: Binary BDT discriminant distributions in four representative STXS classes. The binary BDT discriminant distribution is shown for simulated signal events in the target STXS region (solid) and in other STXS regions (dashed), and by the events in the diphoton mass sidebands ($105 \leq m_{\gamma\gamma} < 120 \text{ GeV}$ or $130 \leq m_{\gamma\gamma} < 160 \text{ GeV}$) representing background (dots). The vertical lines delimit the categories defined in the analysis within each class.

in the smallest $m_{\gamma\gamma}$ window containing 90% of signal events, ranges from 0.03% to 78%. Figure 4 shows the contributions to the expected event yields from each of the 28 merged STXS regions defined in Section 8.4. The contributions are shown as fractions of events originating from each STXS region, in groups of analysis categories targeting the same region. They are obtained as a weighted sum of the fractions for each category in the group, with weights given by the signal-over-background ratio f in each category as defined in Table 4.

Table 4: Expected signal (S) and background (B) yields in each category, within the smallest mass window containing 90% of signal events, the half-width of which is given by σ . The signal purity $f = S/(S + B)$ and expected significance $Z = \sqrt{2((S + B) \ln(1 + S/B) - S)}$ are also shown. Only the signal process corresponding to the targeted STXS region is considered in the signal yield.

Category	S	B	σ [GeV]	f [%]	Z	Category	S	B	σ [GeV]	f [%]	Z
<i>gg</i> \rightarrow H						≥ 2 -jets, $350 \leq m_{jj} < 700$ GeV, $p_T^H \geq 200$ GeV, High-purity	1.31	2.19	2.48	37	0.81
0-jet, $p_T^H < 10$ GeV	695	26 000	3.43	2.6	4.3	≥ 2 -jets, $350 \leq m_{jj} < 700$ GeV, $p_T^H \geq 200$ GeV, Med-purity	1.40	9.22	2.49	13	0.45
0-jet, $p_T^H \geq 10$ GeV	1440	47 000	3.41	3.0	6.6	≥ 2 -jets, $350 \leq m_{jj} < 700$ GeV, $p_T^H \geq 200$ GeV, Low-purity	1.16	65.5	2.54	1.7	0.14
1-jet, $p_T^H < 60$ GeV, High-purity	168	4250	3.20	3.8	2.6	≥ 2 -jets, $700 \leq m_{jj} < 1000$ GeV, $p_T^H \geq 200$ GeV, High-purity	2.51	3.02	2.43	45	1.3
1-jet, $p_T^H < 60$ GeV, Med-purity	197	11 500	3.38	1.7	1.8	≥ 2 -jets, $700 \leq m_{jj} < 1000$ GeV, $p_T^H \geq 200$ GeV, Med-purity	1.49	47.4	2.54	3.0	0.22
1-jet, $60 \leq p_T^H < 120$ GeV, High-purity	186	3310	3.10	5.3	3.2	≥ 2 -jets, $m_{jj} \geq 1000$ GeV, $p_T^H \geq 200$ GeV, High-purity	5.65	1.57	2.39	78	3.3
1-jet, $60 \leq p_T^H < 120$ GeV, Med-purity	180	7780	3.37	2.3	2.0	≥ 2 -jets, $m_{jj} \geq 1000$ GeV, $p_T^H \geq 200$ GeV, Med-purity	2.96	6.31	2.55	32	1.1
1-jet, $120 \leq p_T^H < 200$ GeV, High-purity	23.0	182	2.61	11	1.7	<i>qq</i> \rightarrow $H\ell\nu$					
1-jet, $120 \leq p_T^H < 200$ GeV, Med-purity	40.7	717	3.00	5.4	1.5	$p_T^V < 75$ GeV, High-purity	1.91	4.91	3.17	28	0.81
≥ 2 -jets, $m_{jj} < 350$ GeV, $p_T^H < 60$ GeV, High-purity	23.5	1050	3.08	2.2	0.72	$p_T^V < 75$ GeV, Med-purity	2.59	20.2	3.28	11	0.57
≥ 2 -jets, $m_{jj} < 350$ GeV, $p_T^H < 60$ GeV, Med-purity	43.1	4360	3.39	0.98	0.65	$75 \leq p_T^V < 150$ GeV, High-purity	2.62	2.05	3.02	56	1.6
≥ 2 -jets, $m_{jj} < 350$ GeV, $p_T^H < 60$ GeV, Low-purity	47.5	16 800	3.51	0.28	0.37	$75 \leq p_T^V < 150$ GeV, Med-purity	2.08	12.4	3.23	14	0.58
≥ 2 -jets, $m_{jj} < 350$ GeV, $60 \leq p_T^H < 120$ GeV, High-purity	49.1	901	3.03	5.2	1.6	$150 \leq p_T^V < 250$ GeV, High-purity	1.74	2.06	2.78	46	1.1
≥ 2 -jets, $m_{jj} < 350$ GeV, $60 \leq p_T^H < 120$ GeV, Med-purity	93.9	6440	3.30	1.4	1.2	$150 \leq p_T^V < 250$ GeV, Med-purity	0.16	2.90	3.17	5.2	0.09
≥ 2 -jets, $m_{jj} < 350$ GeV, $120 \leq p_T^H < 200$ GeV, High-purity	15.5	74.8	2.64	17	1.7	$p_T^V \geq 250$ GeV, High-purity	1.36	1.79	2.41	43	0.91
≥ 2 -jets, $m_{jj} < 350$ GeV, $120 \leq p_T^H < 200$ GeV, Med-purity	22.7	343	2.97	6.2	1.2	$p_T^V \geq 250$ GeV, Med-purity	0.02	3.12	3.15	0.78	0.01
≥ 2 -jets, $350 \leq m_{jj} < 700$ GeV, $p_T^H < 200$ GeV, High-purity	4.31	47.5	2.72	8.3	0.62	<i>pp</i> \rightarrow $H\ell\ell$					
≥ 2 -jets, $350 \leq m_{jj} < 700$ GeV, $p_T^H < 200$ GeV, Med-purity	15.4	380	3.02	3.9	0.78	$p_T^V < 75$ GeV, High-purity	1.14	1.82	3.25	39	0.78
≥ 2 -jets, $350 \leq m_{jj} < 700$ GeV, $p_T^H < 200$ GeV, Low-purity	10.5	1080	3.31	0.97	0.32	$p_T^V < 75$ GeV, Med-purity	1.06	215	3.29	0.49	0.07
≥ 2 -jets, $700 \leq m_{jj} < 1000$ GeV, $p_T^H < 200$ GeV, High-purity	2.34	33.3	2.84	6.6	0.40	$75 \leq p_T^V < 150$ GeV, High-purity	1.07	1.58	3.08	40	0.77
≥ 2 -jets, $700 \leq m_{jj} < 1000$ GeV, $p_T^H < 200$ GeV, Med-purity	4.23	136	3.07	3.0	0.36	$75 \leq p_T^V < 150$ GeV, Med-purity	0.02	1.81	3.06	1.2	0.02
≥ 2 -jets, $700 \leq m_{jj} < 1000$ GeV, $p_T^H < 200$ GeV, Low-purity	3.34	429	3.26	0.77	0.16	$150 \leq p_T^V < 250$ GeV, High-purity	0.71	1.79	2.78	28	0.50
≥ 2 -jets, $m_{jj} \geq 1000$ GeV, $p_T^H < 200$ GeV, High-purity	1.14	14.5	2.97	7.3	0.30	$150 \leq p_T^V < 250$ GeV, Med-purity	0.10	16.5	2.88	0.62	0.03
≥ 2 -jets, $m_{jj} \geq 1000$ GeV, $p_T^H < 200$ GeV, Med-purity	2.52	47.5	3.10	5.0	0.36	$p_T^V \geq 250$ GeV	0.27	2.06	2.48	12	0.18
≥ 2 -jets, $m_{jj} \geq 1000$ GeV, $p_T^H < 200$ GeV, Low-purity	2.49	142	3.37	1.7	0.21	<i>pp</i> \rightarrow $H\nu\bar{\nu}$					
$200 \leq p_T^H < 300$ GeV, High-purity	15.3	38.0	2.28	29	2.3	$p_T^V < 75$ GeV, High-purity	0.60	170	3.50	0.35	0.05
$200 \leq p_T^H < 300$ GeV, Med-purity	29.4	236	2.64	11	1.9	$p_T^V < 75$ GeV, Med-purity	1.15	1020	3.57	0.11	0.04
$300 \leq p_T^H < 450$ GeV, High-purity	1.52	2.13	2.02	42	0.95	$p_T^V < 75$ GeV, Low-purity	0.87	2630	3.67	0.03	0.02
$300 \leq p_T^H < 450$ GeV, Med-purity	6.75	17.7	2.16	28	1.5	$75 \leq p_T^V < 150$ GeV, High-purity	0.58	2.30	2.97	20	0.37
$300 \leq p_T^H < 450$ GeV, Low-purity	4.66	43.1	2.46	9.8	0.70	$75 \leq p_T^V < 150$ GeV, Med-purity	1.83	17.8	3.26	9.3	0.43
$450 \leq p_T^H < 650$ GeV, High-purity	1.00	1.25	1.85	45	0.81	$75 \leq p_T^V < 150$ GeV, Low-purity	2.18	288	3.44	0.75	0.13
$450 \leq p_T^H < 650$ GeV, Med-purity	0.800	2.00	1.98	29	0.53	$150 \leq p_T^V < 250$ GeV, High-purity	0.92	2.00	2.75	32	0.61
$450 \leq p_T^H < 650$ GeV, Low-purity	0.830	10.7	2.19	7.2	0.25	$150 \leq p_T^V < 250$ GeV, Med-purity	0.75	2.54	2.94	23	0.45
$p_T^H \geq 650$ GeV	0.220	1.08	1.73	17	0.20	$150 \leq p_T^V < 250$ GeV, Low-purity	0.26	11.7	3.28	2.2	0.08
<i>qq'</i> \rightarrow Hqq'						$p_T^V \geq 250$ GeV, High-purity	0.67	1.55	2.46	30	0.50
0-jet, High-purity	0.330	25.0	3.33	1.3	0.07	$p_T^V \geq 250$ GeV, Med-purity	0.05	1.97	3.05	2.6	0.04
0-jet, Med-purity	1.27	471	3.35	0.27	0.06	<i>t\bar{t}H</i>					
0-jet, Low-purity	10.7	18 800	3.48	0.06	0.08	$p_T^H < 60$ GeV, High-purity	3.04	4.01	3.18	43	1.4
1-jet, High-purity	1.08	2.78	2.99	28	0.61	$p_T^H < 60$ GeV, Med-purity	2.78	13.3	3.37	17	0.74
1-jet, Med-purity	3.50	26.1	3.11	12	0.67	$60 \leq p_T^H < 120$ GeV, High-purity	4.30	4.09	3.06	51	1.9
1-jet, Low-purity	2.88	145	3.24	2.0	0.24	$60 \leq p_T^H < 120$ GeV, Med-purity	2.99	8.61	3.31	26	0.97
≥ 2 -jets, $m_{jj} < 60$ GeV, High-purity	0.350	2.10	2.71	14	0.24	$120 \leq p_T^H < 200$ GeV, High-purity	4.65	3.52	2.73	57	2.1
≥ 2 -jets, $m_{jj} < 60$ GeV, Med-purity	0.670	19.0	2.79	3.4	0.15	$120 \leq p_T^H < 200$ GeV, Med-purity	1.66	4.16	2.93	29	0.77
≥ 2 -jets, $m_{jj} < 60$ GeV, Low-purity	1.92	243	2.93	0.78	0.12	$200 \leq p_T^H < 300$ GeV	3.39	2.26	2.46	60	1.9
≥ 2 -jets, $60 \leq m_{jj} < 120$ GeV, High-purity	3.45	6.34	2.65	35	1.3	$p_T^H \geq 300$ GeV	2.73	1.66	2.12	62	1.8
≥ 2 -jets, $60 \leq m_{jj} < 120$ GeV, Med-purity	4.99	43.0	2.85	10	0.75	<i>tH</i>					
≥ 2 -jets, $60 \leq m_{jj} < 120$ GeV, Low-purity	2.99	87.3	3.01	3.3	0.32	$tHqb$, High-purity	0.55	2.16	3.04	20	0.36
≥ 2 -jets, $120 \leq m_{jj} < 350$ GeV, High-purity	2.98	24.4	2.93	11	0.59	$tHqb$, Med-purity	0.14	2.78	3.45	4.9	0.09
≥ 2 -jets, $120 \leq m_{jj} < 350$ GeV, Med-purity	6.73	204	2.94	3.2	0.47	$tHqb$, BSM ($\kappa_r = -1$)	0.12	1.86	3.25	6.0	0.09
≥ 2 -jets, $120 \leq m_{jj} < 350$ GeV, Low-purity	8.78	1360	2.99	0.64	0.24	tHW	0.16	6.91	2.74	2.3	0.06
≥ 2 -jets, $350 \leq m_{jj} < 700$ GeV, $p_T^H < 200$ GeV, High-purity	2.52	2.75	2.96	48	1.4	Low-purity top					
≥ 2 -jets, $350 \leq m_{jj} < 700$ GeV, $p_T^H < 200$ GeV, Med-purity	9.15	34.7	3.06	21	1.5	tH	5.18	65.8	3.32	7.3	0.63
≥ 2 -jets, $350 \leq m_{jj} < 700$ GeV, $p_T^H < 200$ GeV, Low-purity	5.97	106	3.27	5.3	0.57						
≥ 2 -jets, $700 \leq m_{jj} < 1000$ GeV, $p_T^H < 200$ GeV, High-purity	2.91	3.00	2.90	49	1.5						
≥ 2 -jets, $700 \leq m_{jj} < 1000$ GeV, $p_T^H < 200$ GeV, Med-purity	5.60	22.7	3.11	20	1.1						
≥ 2 -jets, $m_{jj} \geq 1000$ GeV, $p_T^H < 200$ GeV, High-purity	10.8	3.89	3.01	74	4.2						
≥ 2 -jets, $m_{jj} \geq 1000$ GeV, $p_T^H < 200$ GeV, Med-purity	10.7	19.0	3.23	36	2.3						

STXS Region

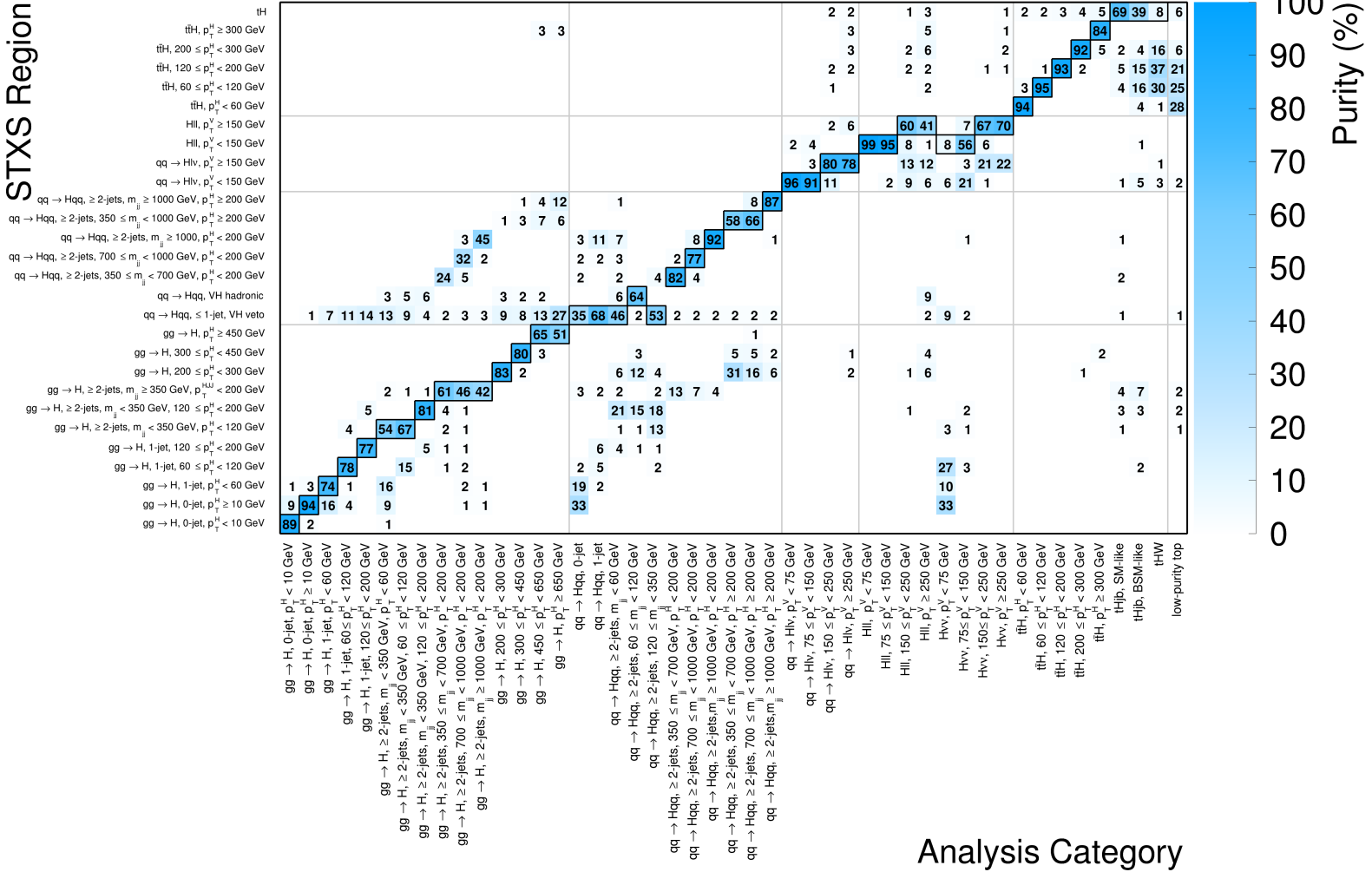


Figure 4: Contributions of STXS regions to the expected event yields in groups of analysis categories. The vertical axis lists the 28 merged STXS regions defined in Section 8.4, while the horizontal axis lists groups of analysis categories that target the same STXS region, weighted by their f value as given in Table 4. Entries correspond to the percentage of the signal yield in each group of analysis categories (on the x -axis) that is contributed by a given STXS region (on the y -axis). Entries with a value below 1% are not shown. The entries in each column, corresponding to the same group of analysis categories, add up to 100 (%), except for rounding effects and values below 1%.

6 Modelling of diphoton mass distributions

The $m_{\gamma\gamma}$ distribution in each category is described by an extended probability density function (pdf) in which the signal and background shapes are analytic functions of $m_{\gamma\gamma}$. As in the previous measurement [10], the analytic functions are defined over the range of $105 < m_{\gamma\gamma} < 160$ GeV. The analysis results are obtained by a simultaneous fit of these pdfs to the $m_{\gamma\gamma}$ distributions in the categories defined in Section 5.2. Systematic uncertainties related to signal yield, signal shape and background modelling are incorporated into the likelihood model as nuisance parameters. For each of these nuisance parameters, a Gaussian or log-normal constraint pdf is included in the likelihood function. Gaussian constraints are used for uncertainties related to the background modelling, the peak position of the signal $m_{\gamma\gamma}$ distribution, and the Higgs boson mass. Log-normal constraints are used for other uncertainties, including multiplicative uncertainties in expected signal yields and in the $m_{\gamma\gamma}$ mass resolution. Asymmetric log-normal forms are used when the corresponding uncertainties are themselves asymmetric. The Higgs boson mass m_H is assumed to be 125.09 ± 0.24 GeV, as measured in Ref. [60].

The effects of interference between the $H \rightarrow \gamma\gamma$ signal process and continuum $\gamma\gamma$ production lead to a small change in the expected Higgs boson production rate (a 2% reduction in the inclusive rate [140]) as well as a shift in the signal peak position that is small compared to the uncertainty in m_H [141]. Both effects are neglected.

In each category i , the normalization of the background pdf is a free parameter in the fit, as well as the parameters describing the shapes of the background pdfs, as discussed in Section 6.2 below. The normalization of the signal pdf is expressed as

$$N_i = \sum_t (\sigma_t \times B_{\gamma\gamma}) \epsilon_{it} \mathcal{L} K_i(\theta_{\text{yield}}) + N_{\text{spur},i} \theta_{\text{spur},i} \quad (1)$$

where the sum runs over STXS regions, $(\sigma_t \times B_{\gamma\gamma})$ is the measurement parameter for region t , ϵ_{it} describes the efficiency for events from region t to be reconstructed in category i , and \mathcal{L} is the integrated luminosity of the fitted sample. The factor $K_i(\theta_{\text{yield}})$ corresponds to multiplicative corrections to the signal yields from systematic uncertainty effects detailed in Section 7, as a function of nuisance parameters collectively denoted by θ_{yield} ; $N_{\text{spur},i}$ is the value of the background modelling uncertainty described in Section 6.2, implemented as an additive correction to the signal yield proportional to the nuisance parameter $\theta_{\text{spur},i}$. The values of the measurement parameters are obtained from a maximum-likelihood fit to the data.

6.1 Modelling of the signal shape

The signal component in each category corresponds to the sum of the contributions from each STXS region, which are all assumed to follow the same $m_{\gamma\gamma}$ distribution in this category. The shape is described using a double-sided Crystal Ball (DSCB) function [142, 143], consisting of a Gaussian distribution in the region around the peak position, continued by power-law tails at lower and higher $m_{\gamma\gamma}$ values. An intrinsic shape difference between the DSCB function and signal $m_{\gamma\gamma}$ distribution is found to cause only a negligible bias in the estimated signal yield [10].

The parameters of the Crystal Ball function in each category are obtained by a fit to a mixture of the ggF, VBF, VH , $t\bar{t}H$ and tH samples, described in Section 3.2, in proportion to their SM cross-sections. A shift of 0.09 GeV is applied to the position of the signal peak to account for the difference between the reference Higgs boson mass used in this analysis ($m_H = 125.09$ GeV) and the mass for which the samples were

generated ($m_H = 125$ GeV). Simulated signal $m_{\gamma\gamma}$ distributions and their corresponding DSCB functions are shown for two groups of categories in Figure 5.

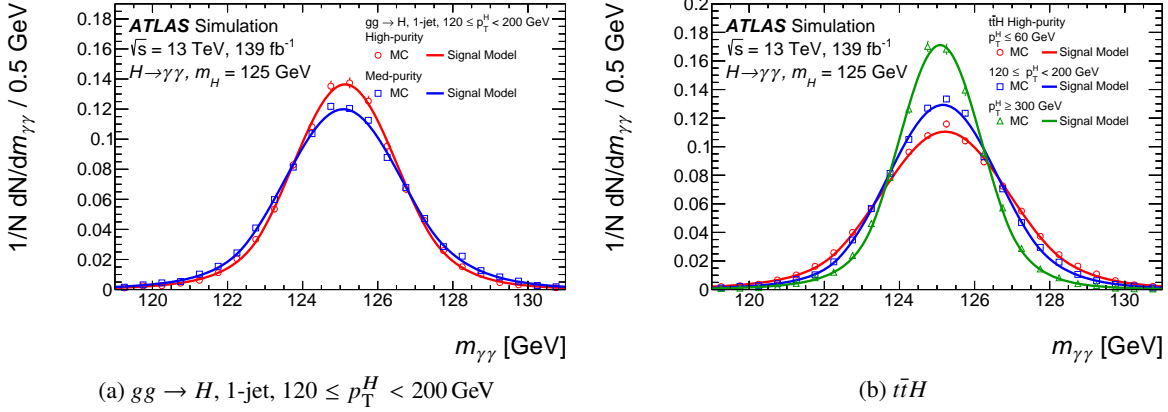


Figure 5: Shape of the signal $m_{\gamma\gamma}$ distribution for two groups of categories. 5(a) compares the signal $m_{\gamma\gamma}$ shapes for the two categories targeting the $gg \rightarrow H, 1\text{-jet}, 120 \leq p_T^H < 200 \text{ GeV}$ region. 5(b) compares the signal $m_{\gamma\gamma}$ shapes for three High-purity categories targeting different p_T^H regions of the $t\bar{t}H$ process. The markers represent distributions in MC samples with $m_H = 125$ GeV, while the solid lines represent the corresponding fitted DSCB functions.

6.2 Modelling of the continuum background shape

The background in the selected diphoton sample mainly consists of continuum $\gamma\gamma$ production, γj and jj production where one or more jets in the event are misidentified as photons. In the categories targeting $V(\rightarrow \text{leptons})H$ production, the main contribution is from the $V\gamma\gamma$ processes, while in categories targeting $t\bar{t}H$ and tH production the main contributions are from $t\bar{t}\gamma\gamma$ and other processes involving top quarks. The modelling of this continuum background follows the same procedure as in previous analyses [10]. This procedure involves two main steps: first, a background $m_{\gamma\gamma}$ template is constructed from a combination of simulation samples and data control samples; secondly, a background function is selected from a number of candidate functions, using the *spurious-signal test*, with the goal of identifying an analytic function that is flexible enough to fit the $m_{\gamma\gamma}$ distribution in data and results in a sufficiently small potential bias compared to the statistical uncertainty.

In categories targeting the $gg \rightarrow H$ and $qq' \rightarrow Hqq'$ processes, the template is defined as a combination of $\gamma\gamma$, γj , and jj processes, each of which is weighted according to its fraction in the selected analysis category. The fractions of these processes are determined by a data-driven method, known as the double two-dimensional sideband method [144], which uses three control regions in data in which one (for the γj process) or both (for the jj process) photons fail to satisfy the identification and/or isolation criteria, respectively. The fraction of the total background that is from the $\gamma\gamma$ process ranges between 75% and 95%, the fraction from the γj process is between 2% and 25%, and the jj process contributes less than 6%.

While a simulation sample is used to model the $\gamma\gamma$ process in this study, it is computationally prohibitive to generate sufficiently large samples of γj and jj production events passing analysis selections due to their large cross-sections and the high jet-rejection performance of the ATLAS photon identification algorithms. To avoid this issue, the $m_{\gamma\gamma}$ shapes of the γj or jj components are obtained from data control samples

defined by inverting the identification requirement of one or both photons as described above. The ratio of the $m_{\gamma\gamma}$ distribution of the γj and jj components to that of the simulated $\gamma\gamma$ sample is well described by a linear function of $m_{\gamma\gamma}$. A linear fit to the ratio of these distributions is therefore used to provide an $m_{\gamma\gamma}$ -dependent weight that is applied to the $\gamma\gamma$ sample to obtain a final template that also accounts for the γj and jj components. Changing the fraction of the γj and jj components within the uncertainties of their determination is found to have a negligible impact on the spurious-signal test described below.

For categories targeting the $V(\rightarrow \text{leptons})H$ STXS regions, the background template is built using simulated events of $V\gamma\gamma$ and prompt $\gamma\gamma$ production. Since the available yields for the latter are not sufficient to build the template directly, the following procedure is followed: first the ratio of the $m_{\gamma\gamma}$ distribution of both samples to that of the $V\gamma\gamma$ sample alone is fitted to a linear function of $m_{\gamma\gamma}$; the fit result is then applied to the $m_{\gamma\gamma}$ distribution of the $V\gamma\gamma$ sample as an $m_{\gamma\gamma}$ -dependent weight to obtain the final template describing both contributions. For categories targeting the $t\bar{t}H$ and tH processes, the diphoton events are primarily from $t\bar{t}\gamma\gamma$ production. As such, a sample of simulated $t\bar{t}\gamma\gamma$ events is used to construct the background template for those categories. Contributions from processes with jets misidentified as photons are not considered in categories targeting VH , $t\bar{t}H$ and tH STXS regions as they do not significantly alter the background shape. The background templates constructed for four categories targeting the $gg \rightarrow H$, $qq' \rightarrow Hqq'$, VH and $t\bar{t}H$ processes are shown as examples in Figure 6. While the background template and data $m_{\gamma\gamma}$ distribution have slightly different shapes in some categories, the selected background analytic functions are flexible enough to absorb these small differences.

The background templates are defined over the range $105 < m_{\gamma\gamma} < 160$ GeV with 220 uniform-width bins. A template smoothing procedure based on a Gaussian kernel [22] is applied to analysis categories where the average bin occupancy in the background template is at least 20 entries. This procedure suppresses statistical fluctuations in the background templates, decreasing the systematic uncertainty on the modeling of the background. A study using pseudo-experiments generated with known template shapes was performed to verify that the smoothing procedure does not introduce a significant bias in the estimate of the spurious signal.

Three families of analytic functions are tested as candidates to model the $m_{\gamma\gamma}$ distribution for a given analysis category. They include power-law functions, Bernstein polynomials [145], and exponential functions of a polynomial. These functions and the number of degrees of freedom tested are summarized in Table 5. The coefficients of these functions are considered to be independent across categories, regardless of the functions chosen, and in all cases are treated as free parameters in the fits to data. The main criterion used to

Table 5: Summary of the functions used for the modelling of the continuum background component. The free parameters used to define the function shape are denoted as a or a_i , and their total number by N_{pars} . For the definition of the Bernstein polynomials, $x = (m_{\gamma\gamma} - m_{\text{min}})/(m_{\text{max}} - m_{\text{min}})$, where $m_{\text{min}} = 105$ GeV and $m_{\text{max}} = 160$ GeV are respectively the lower and upper bounds of the fitted $m_{\gamma\gamma}$ range.

Type	Function	N_{pars}	Acronym
Power law	$m_{\gamma\gamma}^a$	1	PowerLaw
Bernstein polynomial	$(1-x)^n + a_1nx(1-x)^{n-1} + \dots + a_nx^n$	$n = 1-5$	Bern1-Bern5
Exponential	$\exp(am_{\gamma\gamma})$	1	Exp
Exponential of second-order polynomial	$\exp(a_1m_{\gamma\gamma} + a_2m_{\gamma\gamma}^2)$	2	ExpPoly2
Exponential of third-order polynomial	$\exp(a_1m_{\gamma\gamma} + a_2m_{\gamma\gamma}^2 + a_3m_{\gamma\gamma}^3)$	3	ExpPoly3

select the functional form in each category is a bias test performed by fitting the background template using a model with free parameters for both the signal and the background event yields. In this fit, the background

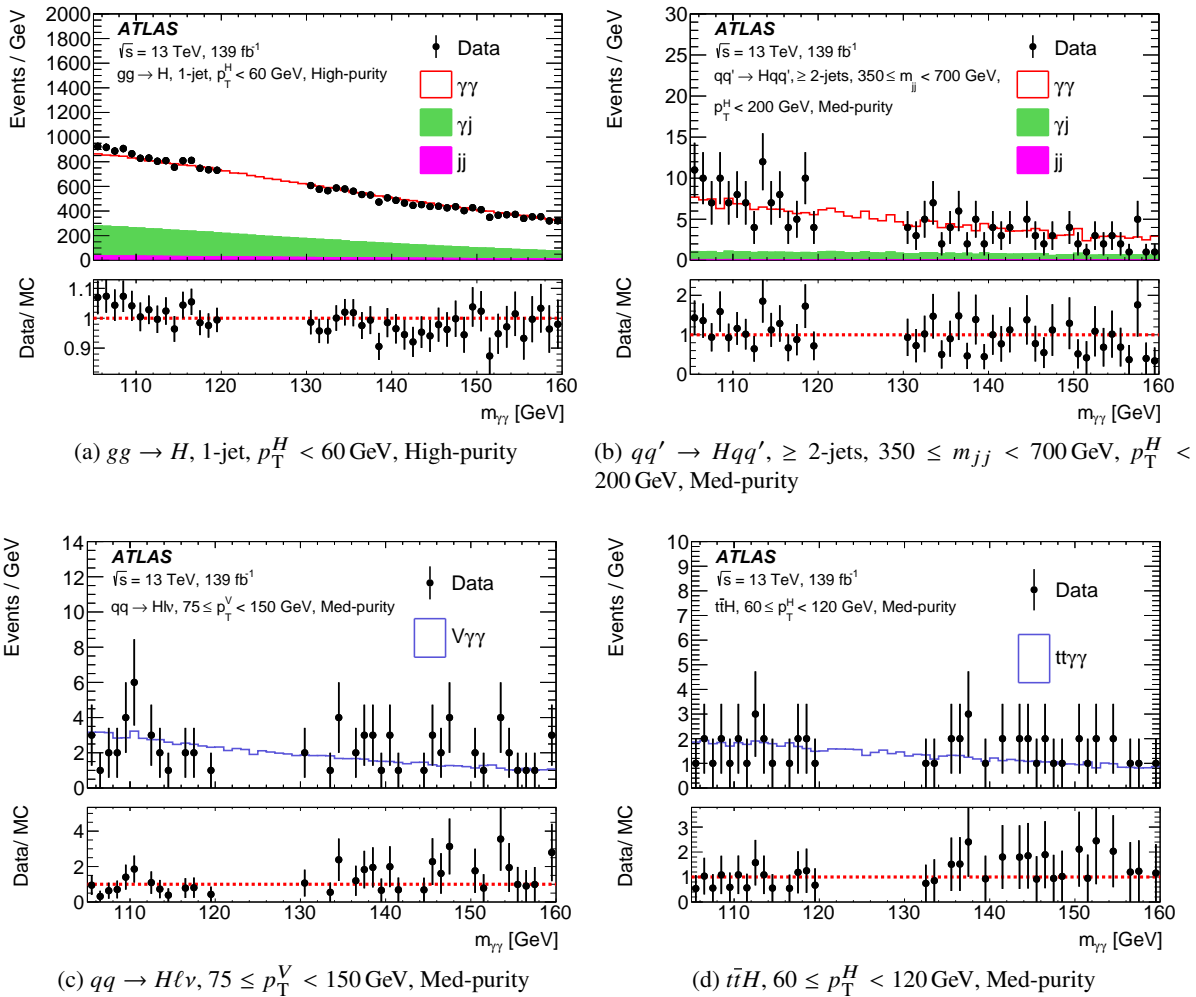


Figure 6: The diphoton invariant mass $m_{\gamma\gamma}$ distribution in data (black points) and continuum background templates (histograms) in four representative STXS categories. The data are shown excluding the region $120 < m_{\gamma\gamma} < 130$ GeV containing the signal. In panels 6(a) and 6(b), stacked histograms corresponding to the $\gamma\gamma$ (white), γj (green) and jj (magenta) background contributions are shown. In panel 6(c), the histogram represents contributions from $V\gamma\gamma$ and other sources of prompt $\gamma\gamma$ production. In 6(d), the histogram corresponds to simulated $t\bar{t}\gamma\gamma$ events. The templates do not represent the background shapes used in the analysis, but are used to identify flexible functions used to model the background in each category as described in the text.

template is normalized to the number of events observed in data in this category. The potential bias due to the mis-modelling of background $m_{\gamma\gamma}$ distribution is estimated from the fitted signal yield (the *spurious* signal). This test is performed for m_H values ranging from 123 GeV to 127 GeV, in steps of 0.5 GeV. In order to avoid accidentally small bias values at the nominal Higgs boson mass of $m_H = 125.09$ GeV, the maximum absolute value of fitted signal yield $|S_{\text{spur}}|$ over the range $123 < m_H < 127$ GeV is considered as the potential bias. For categories where the original background $m_{\gamma\gamma}$ templates (before normalization to the data yields) have at least 20 entries per bin on average, the background functions are required to yield a value of $|S_{\text{spur}}|$ that is smaller than either 10% of the total expected Higgs boson signal yield (S_{exp}) or 20% of the statistical uncertainty of the fitted signal yield (σ_{exp}). If multiple functions pass these requirements, the one with the smallest number of degrees of freedom is chosen.

An additional check is performed for the nine categories in which a fit of the analytic function to the background template is found to yield a χ^2 p -value that is below 1%.⁴ For each of these categories, a set of samples is randomly drawn from the background template, each with a number of events equal to the observed yield in the data sidebands. The fit of the analytic function and the computation of the χ^2 are then repeated for each sample. In all nine categories, more than 90% of the samples yield a χ^2 p -value above 5%, which shows that the low p -values observed in the fit to the nominal background template are related to features compatible with statistical fluctuations. For categories where the average number of entries per bin is less than 20, candidate background functions are limited to `Exp`, `ExpPoly2` and `ExpPoly3` (as defined in Table 5) in order to avoid unphysical fits due to large statistical fluctuations in the sidebands. The function is chosen using a Wald test [146]: first the quantity $q_{12} = -2 \ln L_1/L_2$ is computed from the maximum likelihood values L_1 and L_2 of background-only fits to the data sideband regions using respectively the `Exp` and `ExpPoly2` descriptions of the backgrounds. The `ExpPoly2` model is chosen if the p -value computed from q_{12} is less than 0.05, assuming that q_{12} follows a χ^2 distribution with one degree of freedom. Similarly, the `ExpPoly3` form is chosen over `ExpPoly2` if the p -value for the corresponding Wald test is 0.05 or less. For 32 out of the 101 categories, the Wald-test-based condition was used and the `Exp` function was selected in each case.

In all cases, the $|S_{\text{spur}}|$ value of the selected background function provides an estimate of the possible bias in the fitted signal yield introduced by the intrinsic difference between the background $m_{\gamma\gamma}$ shape and the selected function. It is used to define the systematic uncertainty for the background modelling in category i , denoted as $N_{\text{spur},i}$ in Eq. (1). The selected functional form for each category is shown in Table 6.

7 Systematic uncertainties

Systematic uncertainties considered in this analysis can be grouped into two categories: uncertainties in the modelling of the $m_{\gamma\gamma}$ distribution for the signal and background processes, and uncertainties in the expected signal yields in each category arising from either experimental or theory sources. These systematic uncertainties are incorporated into the likelihood model of the measurement as nuisance parameters, as explained in Section 6. More details about the uncertainties are provided in this section.

7.1 Experimental systematic uncertainties

Experimental systematic uncertainties relevant to the modelling of the signal $m_{\gamma\gamma}$ distribution include the uncertainties in the energy scale and energy resolution of photon candidates, as well as in the Higgs boson mass. The photon energy scale uncertainties are propagated to the peak position of the signal DSCB shape, with an impact that is usually less than 0.3% relative to the peak position value, depending on the category. The photon energy resolution uncertainties are propagated to the Gaussian width of the signal DSCB shape, with a relative impact between 1% and 15%, depending on the category. The estimation and implementation of the photon energy scale and resolution uncertainties follow the procedure outlined in Ref. [120]. The total uncertainty in the measured Higgs boson mass, 0.24 GeV, is considered as an additional uncertainty of the peak position of the signal DSCB shape.

⁴ The χ^2 is computed in a background template uniformly binned over $105 < m_{\gamma\gamma} < 160$ GeV. It has 55 bins, and the number of degrees of freedom used in the computation is $54 - N_{\text{pars}}$, where the N_{pars} is the number of free function parameters. The normalization of the template removes one degree of freedom. The background $m_{\gamma\gamma}$ templates before the smoothing procedure are used.

Table 6: Selected background functional form, number of observed data events in the range $105 < m_{\gamma\gamma} < 160$ GeV (N_{data}), and modelling uncertainty (N_{spur}) for each of the 101 analysis categories. The last column indicates whether the Wald test is used to determine the functional form, as described in the text.

Category	Function	N_{data}	N_{spur}	Wald	Category	Function	N_{data}	N_{spur}	Wald
<i>gg</i> \rightarrow <i>H</i>									
0-jet, $p_T^H < 10$ GeV	ExpPoly2	191623	64.8		≥ 2 -jets, $350 \leq m_{jj} < 700$ GeV, $p_T^H \geq 200$ GeV, High-purity	Exp	18	0.189	✓
0-jet, $p_T^H \geq 10$ GeV	ExpPoly2	349266	50.4		≥ 2 -jets, $350 \leq m_{jj} < 700$ GeV, $p_T^H \geq 200$ GeV, Med-purity	Exp	84	0.513	✓
1-jet, $p_T^H < 60$ GeV, High-purity	ExpPoly2	32644	20.7		≥ 2 -jets, $350 \leq m_{jj} < 700$ GeV, $p_T^H \geq 200$ GeV, Low-purity	Exp	595	0.721	
1-jet, $p_T^H < 60$ GeV, Med-purity	ExpPoly2	85229	24.9		≥ 2 -jets, $700 \leq m_{jj} < 1000$ GeV, $p_T^H \geq 200$ GeV, High-purity	Exp	19	0.110	✓
1-jet, $60 \leq p_T^H < 120$ GeV, High-purity	Exp	26236	23.7		≥ 2 -jets, $700 \leq m_{jj} < 1000$ GeV, $p_T^H \geq 200$ GeV, Med-purity	Exp	411	0.193	
1-jet, $60 \leq p_T^H < 120$ GeV, Med-purity	ExpPoly2	56669	21.3		≥ 2 -jets, $m_{jj} \geq 1000$ GeV, $p_T^H \geq 200$ GeV, High-purity	Exp	23	1.30	✓
1-jet, $120 \leq p_T^H < 200$ GeV, High-purity	ExpPoly2	1570	1.48		≥ 2 -jets, $m_{jj} \geq 1000$ GeV, $p_T^H \geq 200$ GeV, Med-purity	Exp	56	0.329	✓
1-jet, $120 \leq p_T^H < 200$ GeV, Med-purity	ExpPoly2	6163	5.33		<i>qq</i> \rightarrow <i>H</i> ℓ ν				
≥ 2 -jets, $m_{jj} < 350$ GeV, $p_T^H < 60$ GeV, High-purity	ExpPoly2	8513	1.51		$0 \leq p_T^V < 75$ GeV, High-purity	Exp	40	0.277	
≥ 2 -jets, $m_{jj} < 350$ GeV, $p_T^H < 60$ GeV, Med-purity	ExpPoly2	31163	13.6		$0 \leq p_T^V < 75$ GeV, Med-purity	Exp	158	0.609	
≥ 2 -jets, $m_{jj} < 350$ GeV, $p_T^H < 60$ GeV, Low-purity	ExpPoly2	120357	15.7		$75 \leq p_T^V < 150$ GeV, High-purity	Exp	15	0.069	
≥ 2 -jets, $m_{jj} < 350$ GeV, $60 \leq p_T^H < 120$ GeV, High-purity	ExpPoly2	7582	2.26		$75 \leq p_T^V < 150$ GeV, Med-purity	Exp	104	0.255	
≥ 2 -jets, $m_{jj} < 350$ GeV, $60 \leq p_T^H < 120$ GeV, Med-purity	ExpPoly2	48362	6.21		$150 \leq p_T^V < 250$ GeV, High-purity	Exp	17	0.128	✓
≥ 2 -jets, $m_{jj} < 350$ GeV, $120 \leq p_T^H < 200$ GeV, High-purity	ExpPoly2	728	0.004		$150 \leq p_T^V < 250$ GeV, Med-purity	Exp	21	0.150	
≥ 2 -jets, $m_{jj} < 350$ GeV, $120 \leq p_T^H < 200$ GeV, Med-purity	PowerLaw	3007	0.983		$p_T^V \geq 250$ GeV, High-purity	Exp	16	0.237	✓
≥ 2 -jets, $350 \leq m_{jj} < 700$ GeV, $p_T^H < 200$ GeV, High-purity	Exp	432	0.487		$p_T^V \geq 250$ GeV, Med-purity	Exp	27	0.054	✓
≥ 2 -jets, $350 \leq m_{jj} < 700$ GeV, $p_T^H < 200$ GeV, Med-purity	ExpPoly2	3084	1.33		<i>pp</i> \rightarrow <i>H</i> $\ell\ell$				
≥ 2 -jets, $350 \leq m_{jj} < 700$ GeV, $p_T^H < 200$ GeV, Low-purity	Exp	7999	5.78		$0 \leq p_T^V < 75$ GeV, High-purity	Exp	12	0.027	
≥ 2 -jets, $700 \leq m_{jj} < 1000$ GeV, $p_T^H < 200$ GeV, High-purity	Exp	302	0.560		$0 \leq p_T^V < 75$ GeV, Med-purity	PowerLaw	1620	2.28	
≥ 2 -jets, $700 \leq m_{jj} < 1000$ GeV, $p_T^H < 200$ GeV, Med-purity	Exp	1033	1.44		$75 \leq p_T^V < 150$ GeV, High-purity	Exp	13	0.015	
≥ 2 -jets, $700 \leq m_{jj} < 1000$ GeV, $p_T^H < 200$ GeV, Low-purity	Exp	3187	4.32		$75 \leq p_T^V < 150$ GeV, Med-purity	Exp	18	0.016	
≥ 2 -jets, $m_{jj} \geq 1000$ GeV, $p_T^H < 200$ GeV, High-purity	Exp	113	0.192		$150 \leq p_T^V < 250$ GeV, High-purity	Exp	14	0.059	✓
≥ 2 -jets, $m_{jj} \geq 1000$ GeV, $p_T^H < 200$ GeV, Med-purity	Exp	332	0.804		$150 \leq p_T^V < 250$ GeV, Med-purity	Exp	136	0.194	
≥ 2 -jets, $m_{jj} \geq 1000$ GeV, $p_T^H < 200$ GeV, Low-purity	PowerLaw	1020	1.09		$p_T^V \geq 250$ GeV	Exp	14	0.311	✓
$200 \leq p_T^H < 300$ GeV, High-purity	Exp	420	1.68		<i>pp</i> \rightarrow <i>H</i> $\nu\bar{\nu}$				
$200 \leq p_T^H < 300$ GeV, Med-purity	Exp	2296	0.714		$0 \leq p_T^V < 75$ GeV, High-purity	Exp	1174	12.3	✓
$300 \leq p_T^H < 450$ GeV, High-purity	Exp	25	0.407	✓	$0 \leq p_T^V < 75$ GeV, Med-purity	Exp	6897	4.13	
$300 \leq p_T^H < 450$ GeV, Med-purity	Exp	186	0.259		$0 \leq p_T^V < 75$ GeV, Low-purity	ExpPoly3	18084	9.95	
$300 \leq p_T^H < 450$ GeV, Low-purity	Exp	422	0.121		$75 \leq p_T^V < 150$ GeV, High-purity	Exp	16	0.407	✓
$450 \leq p_T^H < 650$ GeV, High-purity	Exp	15	0.138	✓	$75 \leq p_T^V < 150$ GeV, Med-purity	Exp	124	1.30	✓
$450 \leq p_T^H < 650$ GeV, Med-purity	Exp	25	0.391	✓	$75 \leq p_T^V < 150$ GeV, Low-purity	Exp	2019	1.96	
$450 \leq p_T^H < 650$ GeV, Low-purity	Exp	109	0.031		$150 \leq p_T^V < 250$ GeV, High-purity	Exp	16	0.121	✓
$p_T^H \geq 650$ GeV	Exp	14	0.448	✓	$150 \leq p_T^V < 250$ GeV, Med-purity	Exp	17	0.184	✓
<i>qq'</i> \rightarrow <i>H</i> qq'					$150 \leq p_T^V < 250$ GeV, Low-purity	Exp	87	0.644	✓
0-jet, High-purity	Exp	176	0.180		$p_T^V \geq 250$ GeV, High-purity	Exp	15	0.237	✓
0-jet, Med-purity	ExpPoly2	3238	4.73		$p_T^V \geq 250$ GeV, Med-purity	Exp	18	0.201	✓
0-jet, Low-purity	ExpPoly2	133314	49.7		<i>t</i> \bar{t} <i>H</i>				
1-jet, High-purity	Exp	19	0.125	✓	$p_T^H < 60$ GeV, High-purity	Exp	35	0.040	
1-jet, Med-purity	Exp	187	0.361		$p_T^H < 60$ GeV, Med-purity	Exp	96	0.192	
1-jet, Low-purity	PowerLaw	1040	1.97		$60 \leq p_T^H < 120$ GeV, High-purity	Exp	34	0.038	
≥ 2 -jets, $m_{jj} < 60$ GeV, High-purity	Exp	17	0.499	✓	$60 \leq p_T^H < 120$ GeV, Med-purity	Exp	74	0.274	
≥ 2 -jets, $m_{jj} < 60$ GeV, Med-purity	Exp	157	0.489		$120 \leq p_T^H < 200$ GeV, High-purity	Exp	39	0.018	
≥ 2 -jets, $m_{jj} < 60$ GeV, Low-purity	PowerLaw	1978	1.29		$120 \leq p_T^H < 200$ GeV, Med-purity	Exp	37	0.057	
≥ 2 -jets, $60 \leq m_{jj} < 120$ GeV, High-purity	Exp	53	0.165	✓	$200 \leq p_T^H < 300$ GeV	Exp	23	0.261	
≥ 2 -jets, $60 \leq m_{jj} < 120$ GeV, Med-purity	Exp	329	0.520		$p_T^H \geq 300$ GeV	Exp	19	0.180	✓
≥ 2 -jets, $60 \leq m_{jj} < 120$ GeV, Low-purity	PowerLaw	709	1.15		<i>t</i> <i>H</i>				
≥ 2 -jets, $120 \leq m_{jj} < 350$ GeV, High-purity	Exp	214	1.08		<i>tHqb</i> , High-purity	Exp	17	0.371	✓
≥ 2 -jets, $120 \leq m_{jj} < 350$ GeV, Med-purity	ExpPoly2	1671	1.07		<i>tHqb</i> , Med-purity	Exp	19	0.320	✓
≥ 2 -jets, $120 \leq m_{jj} < 350$ GeV, Low-purity	PowerLaw	11195	6.34		<i>tHqb</i> , BSM ($\kappa_t = -1$)	Exp	14	0.496	✓
≥ 2 -jets, $350 \leq m_{jj} < 700$ GeV, $p_T^H < 200$ GeV, High-purity	Exp	25	0.162	✓	<i>tHW</i>	Exp	38	0.070	
≥ 2 -jets, $350 \leq m_{jj} < 700$ GeV, $p_T^H < 200$ GeV, Med-purity	Exp	260	0.443		<i>Low-purity top</i>				
≥ 2 -jets, $350 \leq m_{jj} < 700$ GeV, $p_T^H < 200$ GeV, Low-purity	Exp	753	1.17		Low-purity top	Exp	500	0.870	
≥ 2 -jets, $700 \leq m_{jj} < 1000$ GeV, $p_T^H < 200$ GeV, High-purity	Exp	25	0.670	✓					
≥ 2 -jets, $700 \leq m_{jj} < 1000$ GeV, $p_T^H < 200$ GeV, Med-purity	Exp	166	0.713						
≥ 2 -jets, $m_{jj} \geq 1000$ GeV, $p_T^H < 200$ GeV, High-purity	Exp	48	1.47	✓					
≥ 2 -jets, $m_{jj} \geq 1000$ GeV, $p_T^H < 200$ GeV, Med-purity	Exp	142	0.270						

The modelling of the background $m_{\gamma\gamma}$ distribution with an analytic function can produce a potential bias in the fitted signal yield. An uncertainty in the modelling of the background, computed using the spurious-signal method described in Section 6.2, is included as an additive contribution to the signal yield in each category as shown in Eq. (1). This uncertainty is considered to be uncorrelated between different categories. Out of the 101 analysis categories, 46 categories have a background modelling uncertainty that is no more than 10% of the background statistical uncertainty, and only 2 categories ($qq' \rightarrow Hqq'$, ≥ 2 -jets, $m_{jj} \geq 1000$ GeV, $p_T^H \geq 200$ GeV, High-purity and $pp \rightarrow H\nu\bar{\nu}$, $0 \leq p_T^V < 75$ GeV, High-purity) have a background modelling uncertainty that is at least 50% of the background statistical uncertainty.

Experimental uncertainties affecting the expected signal yields include: the efficiency of the diphoton trigger [35], the photon identification efficiencies [120], the photon isolation efficiencies, the impact of the

photon energy scale and resolution uncertainties on the selection efficiency [120], the modelling of pile-up in the simulation, which is evaluated by varying by $\pm 9\%$ the value of the visible inelastic cross-section used to reweight the pile-up distribution in the simulation to that in the data [147], the jet energy scale and resolution [130], the efficiency of the jet vertex tagger, the efficiency of the b -tagging algorithm [133], the electron [120] and muon [134] reconstruction, identification and isolation efficiencies, the electron [120] and muon [134] energy and momentum scale and resolution, as well as the contribution to E_T^{miss} from charged-particle tracks that are not associated with high- p_T electrons, muons, jets, or photons [135]. The uncertainty in the combined 2015–2018 integrated luminosity is 1.7% [20], obtained using the LUCID-2 detector [21] for the primary luminosity measurements.

7.2 Theory modelling uncertainties

The main theory uncertainties arise from missing higher-order terms in the perturbative QCD calculations, the modelling of parton showers, the PDFs and the value of α_s . For measurements of the $t\bar{t}H$ and tH processes, the modelling of heavy-flavour jets in the ggF, VBF, and VH processes is also important.

QCD uncertainties for each production mode are estimated by varying the renormalization and factorization scales used in the event generation, and the resulting variations in the predicted event yield in each STXS regions are considered as uncertainties.

For the $gg \rightarrow H$ processes, the QCD uncertainty model is implemented using four components [6, 148–150] accounting for modelling uncertainties in the jet multiplicity, three describing uncertainties in the modelling the p_T^H distribution, one [151, 152] accounting for the uncertainty in the distribution of the p_T^{Hjj} variable, four accounting for the uncertainty in the distribution of the m_{jj} variable, and six covering modelling uncertainties in STXS regions with high p_T^H (> 300 GeV). Following the principles of the Stewart–Tackmann procedure [151], two components account for uncertainties in the inclusive $gg \rightarrow H$ event yields, while the others describe *migration* uncertainties in the fraction of events passing the selections defining the STXS regions. The model provides a full description of the uncertainty in each STXS region, in which the uncertainty components are each assigned to one nuisance parameter that is treated as statistically independent from the others. These uncertainties are typically less than 22% of the expected signal yield in analysis categories targeting the $gg \rightarrow H$ process.

For each of the WH , $qq/qg \rightarrow ZH$, and $gg \rightarrow ZH$ processes, the QCD uncertainty model includes four independent components to account for uncertainties in the distribution of p_T^V , and two independent components for uncertainties in the jet multiplicity distribution. For $qq' \rightarrow Hqq'$ (VBF and $V(\rightarrow \text{hadrons})H$) processes, the QCD uncertainty model includes a similar set of independent components: two for the modelling of the jet multiplicity and the p_T^{Hjj} distribution, one for migration between the $p_T^H < 200$ GeV and $p_T^H \geq 200$ GeV regions, and six for the modelling of the m_{jj} distribution. These uncertainties are less than 10% of the expected signal yield in analysis categories targeting these processes, with the exception of the $gg \rightarrow ZH$ process where the uncertainty can be as large as 26%.

For the $t\bar{t}H$ process, QCD uncertainties include five components covering migrations between $t\bar{t}H$ STXS regions with different p_T^H . These uncertainties are less than 10% of the expected signal yield in the $t\bar{t}H$ STXS regions in their targeted analysis categories. In the case of tHW , $tHqb$ and $b\bar{b}H$, an overall QCD uncertainty is used, taking the value from Ref. [6].

To check the robustness of the uncertainty model, a comparison between the efficiency factors of the nominal Higgs signal sample and the alternative sample generated by MADGRAPH5_AMC@NLO, as

described in Section 3.2, is performed for the VBF, VH , and $t\bar{t}H$ processes. The differences between the efficiency factors of the nominal and alternative samples are significantly larger than the uncertainties from QCD scale variations and can reach values of up to 20% in some phase-space regions of the VBF process. The differences between the efficiency factors of the nominal and alternative samples are therefore considered as an additional systematic uncertainty. A similar comparison was not performed for the $gg \rightarrow H$ process since the corresponding alternative samples are already used in the derivation of the QCD uncertainty model described above.

The modelling of the parton shower, underlying event, and hadronization is assessed separately for each Higgs boson production mode by comparing the acceptance times efficiency factors of simulated signal samples showered by PYTHIA 8 with those of samples showered by HERWIG 7. The uncertainties estimated from the differences between these factors typically do not exceed 20%, and increase with jet multiplicity.

Uncertainties on the PDFs and the value of α_s are taken from Ref. [6] for the tHW , $tHqb$ and $b\bar{b}H$ processes. For other modes, the uncertainties are estimated using the PDF4LHC15 recommendations [46]. Their effects are usually small compared to the those of the two other main sources of uncertainty mentioned at the start of this subsection.

In categories targeting the $t\bar{t}H$ and tH processes, the predicted ggF, VBF and VH yields are each assigned a conservative 100% uncertainty (correlated between categories), which is due to the theoretical uncertainty associated with the radiation of additional heavy-flavour jets in these Higgs boson production modes. This is supported by measurements using $H \rightarrow ZZ^* \rightarrow 4\ell$ [153], $t\bar{t}b\bar{b}$ [154], and Vb [155, 156] events. The impact of this uncertainty on the results is generally negligible compared to the statistical uncertainties, since the contributions from non- $t\bar{t}H$ processes are generally low.

A total uncertainty of 2.9% is assigned to the $H \rightarrow \gamma\gamma$ decay branching ratio, based on calculations from the HDECAY [94–96] and PROPHECY4F [97–99] programs, which also includes the uncertainty arising from its dependence on quark masses and α_s .

Theory uncertainties, such as missing higher-order QCD corrections and PDF-induced uncertainties, affect both the expected signal yields from each production process and the signal acceptance factors (ϵ_{it} in Eq. (1)) in each category. Uncertainties in signal acceptance factors are included in all the measurements presented in this paper. Signal yield uncertainties, including the uncertainty in the $H \rightarrow \gamma\gamma$ branching ratio, are included only for the measurement of the Higgs boson signal strength and interpretations within the κ -framework and SMEFT models, which rely on comparisons between the observed event yields and their SM predictions. Uncertainties on the parton shower, underlying event, and hadronization effects are included in all the measurements, without a separation into yield and acceptance components. In addition, cross-section measurements spanning multiple STXS regions require assumptions about the expected event yields in each region, as explained in Section 8.4, which introduces a weak dependence on the signal yield uncertainties.

Table 7 shows the expected experimental and theoretical systematic uncertainties of the cross-section measurements in the SM hypothesis, computed as described in Section 8.1.

8 Results

Results are presented in terms of several descriptions of Higgs boson production: the overall signal strength of Higgs boson production measured in the diphoton decay channel (Section 8.2), separate cross-sections

Table 7: Expected contributions from the main sources of systematic uncertainty to the total uncertainty in the measurement of the cross-section times $H \rightarrow \gamma\gamma$ branching ratio for each of the main Higgs boson production processes. The uncertainty from each source ($\Delta\sigma$) is shown as a fraction of the total expected cross-section (σ).

	ggF + $b\bar{b}H$	VBF	WH	ZH	$t\bar{t}H$	tH
Uncertainty source	$\Delta\sigma$ [%]	$\Delta\sigma$ [%]	$\Delta\sigma$ [%]	$\Delta\sigma$ [%]	$\Delta\sigma$ [%]	$\Delta\sigma$ [%]
Theory uncertainties						
Higher-order QCD terms	± 1.4	± 4.1	± 4.1	± 12	± 2.8	± 16
Underlying event and parton shower	± 2.5	± 16	± 2.5	± 4.0	± 3.6	± 48
PDF and α_s	$< \pm 1$	± 2.0	± 1.4	± 2.3	$< \pm 1$	± 5.8
Matrix element	$< \pm 1$	± 3.2	$< \pm 1$	± 1.2	± 2.5	± 8.2
Heavy-flavour jet modelling in non- $t\bar{t}H$ processes	$< \pm 1$	$< \pm 1$	$< \pm 1$	$< \pm 1$	$< \pm 1$	± 13
Experimental uncertainties						
Photon energy resolution	± 3.0	± 3.0	± 3.8	± 4.8	± 3.0	± 12
Photon efficiency	± 2.7	± 2.7	± 3.3	± 3.6	± 2.9	± 9.3
Luminosity	± 1.8	± 2.0	± 2.4	± 2.7	± 2.2	± 6.6
Pile-up	± 1.4	± 2.2	± 2.0	± 2.3	± 1.4	± 7.3
Background modelling	± 2.0	± 4.6	± 3.6	± 7.2	± 2.5	± 63
Photon energy scale	$< \pm 1$	$< \pm 1$	$< \pm 1$	± 1.3	$< \pm 1$	± 5.6
Jet/ E_T^{miss}	$< \pm 1$	± 6.8	$< \pm 1$	± 2.2	± 3.5	± 22
Flavour tagging	$< \pm 1$	$< \pm 1$	$< \pm 1$	$< \pm 1$	± 1.5	± 3.4
Leptons	$< \pm 1$	$< \pm 1$	$< \pm 1$	$< \pm 1$	$< \pm 1$	± 1.8
Higgs boson mass	$< \pm 1$	$< \pm 1$	$< \pm 1$	$< \pm 1$	$< \pm 1$	$< \pm 1$

for the main Higgs boson production modes (Section 8.3), and cross-sections in a set of merged STXS regions defined for each production process (Section 8.4).

8.1 Statistical procedure

The results for each measurement reported in this paper are obtained by expressing the signal event yields in each analysis category in terms of the measurement parameters, and fitting the model to the data in all categories simultaneously. Both positive and negative values are allowed for all parameters, unless otherwise indicated. Best-fit values are reported along with uncertainties corresponding to 68% confidence level (CL) intervals obtained from a profile likelihood technique [139]. The endpoints of the intervals are defined by the condition $-2 \ln \Lambda(\mu) = 1$, where $\Lambda(\mu)$ is the ratio of the profile likelihood at a value μ of the parameters of interest to the profile likelihood at the best-fit point. Similarly, 95% CL intervals are defined by the condition $-2 \ln \Lambda(\mu) = 3.84$. In some cases, uncertainties are presented as a decomposition into separate components: the *statistical* component is obtained from a fit in which the nuisance parameters associated with systematic uncertainties are fixed to their best-fit values; the *systematic* component, corresponding to the combined effect of systematic uncertainties, is computed as the square root of the difference between the squares of the total uncertainty and the statistical uncertainty. Uncertainty components corresponding to smaller groups of nuisance parameters are obtained by iteratively fixing the parameters in each group, subtracting the square of the uncertainty obtained in this configuration from that obtained when the parameters are profiled, and taking the square root.

Expected results for the SM are obtained from a fit to an Asimov data set [139, 157] built from the likelihood model with signal and background components. The nuisance parameters of the likelihood model are determined in a fit to the observed data where the STXS parameters defining the signal normalization in each category are left free. The STXS parameters are set to their SM expectations to generate the Asimov data set. Compatibility with the Standard Model is assessed from the value of the profile likelihood ratio of the model in data under the SM hypothesis; a p -value for compatibility with the SM is computed assuming that the profile likelihood follows a χ^2 distribution with a number of degrees of freedom equal to the number of parameters of interest [139]. In the case of cross-section measurements, uncertainties in the SM predictions are not accounted for in the p -value computation.

8.2 Overall Higgs boson signal strength

To quantify the overall size of the Higgs boson signal in the diphoton channel, the inclusive signal strength, μ , defined as the ratio of the observed value of the product of the Higgs boson production cross-section and the $H \rightarrow \gamma\gamma$ branching ratio ($\sigma \times B_{\gamma\gamma}$) in $|y_H| < 2.5$ to that of its SM prediction, is measured by simultaneously fitting the $m_{\gamma\gamma}$ distributions of the 101 analysis categories. The signal strength μ is treated in the likelihood function as a single parameter of interest which scales the expected yields in all STXS regions and is found to be

$$\mu = 1.04_{-0.09}^{+0.10} = 1.04 \pm 0.06 \text{ (stat.)}_{-0.05}^{+0.06} \text{ (theory syst.)}_{-0.04}^{+0.05} \text{ (exp. syst.)}.$$

The overall $m_{\gamma\gamma}$ distribution of the selected diphoton sample is shown in Figure 7. The events are weighted by the $\ln(1 + S/B)$ of their category, where S and B are the expected signal and background yields within the smallest $m_{\gamma\gamma}$ window containing 90% of the signal events, shown in Table 4. This choice of event weight is designed to enhance the contribution of events from categories with higher signal-to-background ratio in a way that approximately matches the impact of these events in the categorized analysis of the data.

Table 8 further breaks down the impact of systematic uncertainties on the signal-strength measurement. The leading sources of experimental systematic uncertainty are the photon energy resolution uncertainty (2.8%) and photon efficiency uncertainty (2.6%), while the leading sources of theoretical uncertainty are the QCD scale uncertainty (3.8%) and $H \rightarrow \gamma\gamma$ branching ratio uncertainty (3.0%).

8.3 Production cross-sections

The mechanism of Higgs boson production is probed by considering the ggF, VBF, WH , ZH , $t\bar{t}H$, and tH production processes separately. The measurement is reported in terms of the $(\sigma \times B_{\gamma\gamma})$ value in each case, with the cross-sections defined in $|y_H| < 2.5$. As in the STXS region definition, the contribution from the $b\bar{b}H$ process is included in the ggF component. Figure 8 shows the $m_{\gamma\gamma}$ distributions for analysis categories targeting different production modes separately. The same weighting procedure as in Figure 7 is used, except that the signal yield only includes the contributions from the targeted production process, while other signal production processes are included in the background yield.

The best-fit values of the production cross-sections and their uncertainties are summarized in Figure 9 and Table 9. A negative best-fit value is observed for the cross-section of the ZH process, which corresponds to a total observed event yield that is below the background expectation. The p -value for compatibility of the

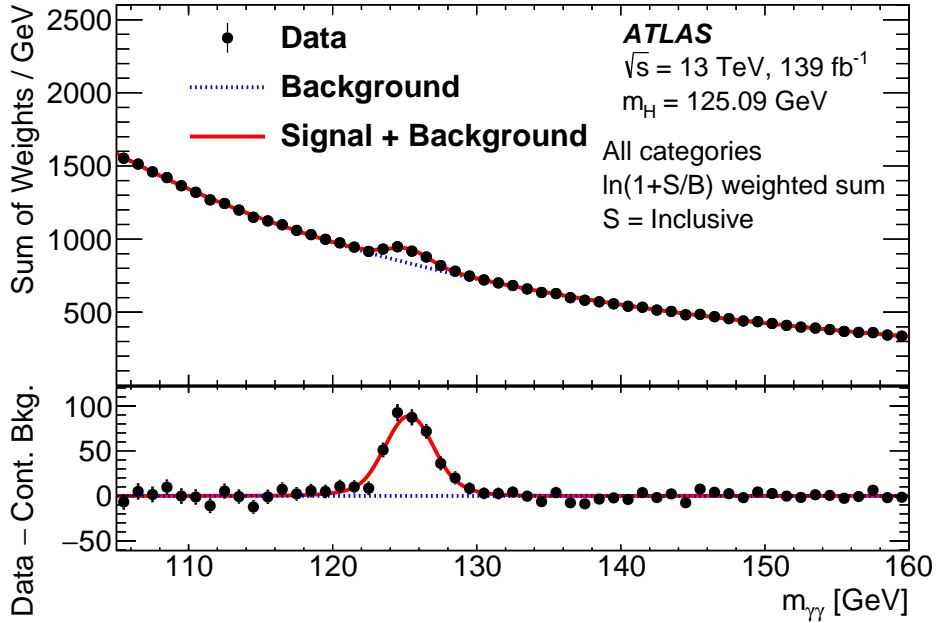


Figure 7: The inclusive diphoton invariant mass distribution of events from all analysis categories. The data events (dots) in each category are weighted by $\ln(1 + S/B)$, where S and B are the expected signal and background yields in this category within the smallest $m_{\gamma\gamma}$ window containing 90% of the signal events. The expected signal is considered inclusively over all STXS regions. The fitted signal-plus-background pdfs from all categories are also weighted and summed, shown as the solid line. The blue dotted line represents the weighted sum of the fitted background functions from all categories. The error bars on the data points are computed following Ref. [158].

cross-section measurement and the SM prediction is 55%. The correlations between these measurements are shown in Figure 10. Compared to Ref. [10], correlations between measurements are reduced, and in particular, the anti-correlation between the ggF and VBF measurements is now -13% , corresponding to a 30% reduction. This is driven by a reduction in the ggF contamination in categories targeting the VBF process, mainly resulting from the use of the D-optimality criterion in the categorization. An anti-correlation of -37% is observed between the WH and ZH measurements, mainly due to contamination by $qq \rightarrow H\ell\nu$ events in the categories targeting the $pp \rightarrow H\nu\bar{\nu}$ process. This correlation is mitigated by the separation of the $pp \rightarrow H\ell\ell$ and $pp \rightarrow H\nu\bar{\nu}$ processes that is introduced in the analysis categorization. Similarly, $t\bar{t}H$ contamination in the categories targeting tH lead to an anti-correlation of -44% between these two processes.

The largest theoretical systematic uncertainty in these measurements arises from the modelling of the parton showering and underlying event, and its impact on the measured cross-sections ranges from 38% for the tH process to 14% for the VBF process and to 3%–4% for the $gg \rightarrow H$ and WH processes. For the $gg \rightarrow H$ process, the leading experimental systematic uncertainty is the photon energy resolution uncertainty (3%). For the VBF and $t\bar{t}H$ processes, the leading experimental uncertainty is related to the properties of jets and missing transverse momentum, reaching 5.4% for VBF. For other processes, the leading experimental systematic uncertainty is the background modelling uncertainty, ranging from 3.7% for WH to 24% for tH .

An upper limit on the rate of tH production is obtained by treating the normalization of other Higgs boson production processes as nuisance parameters. Using the CL_s method [159], this excludes a tH production

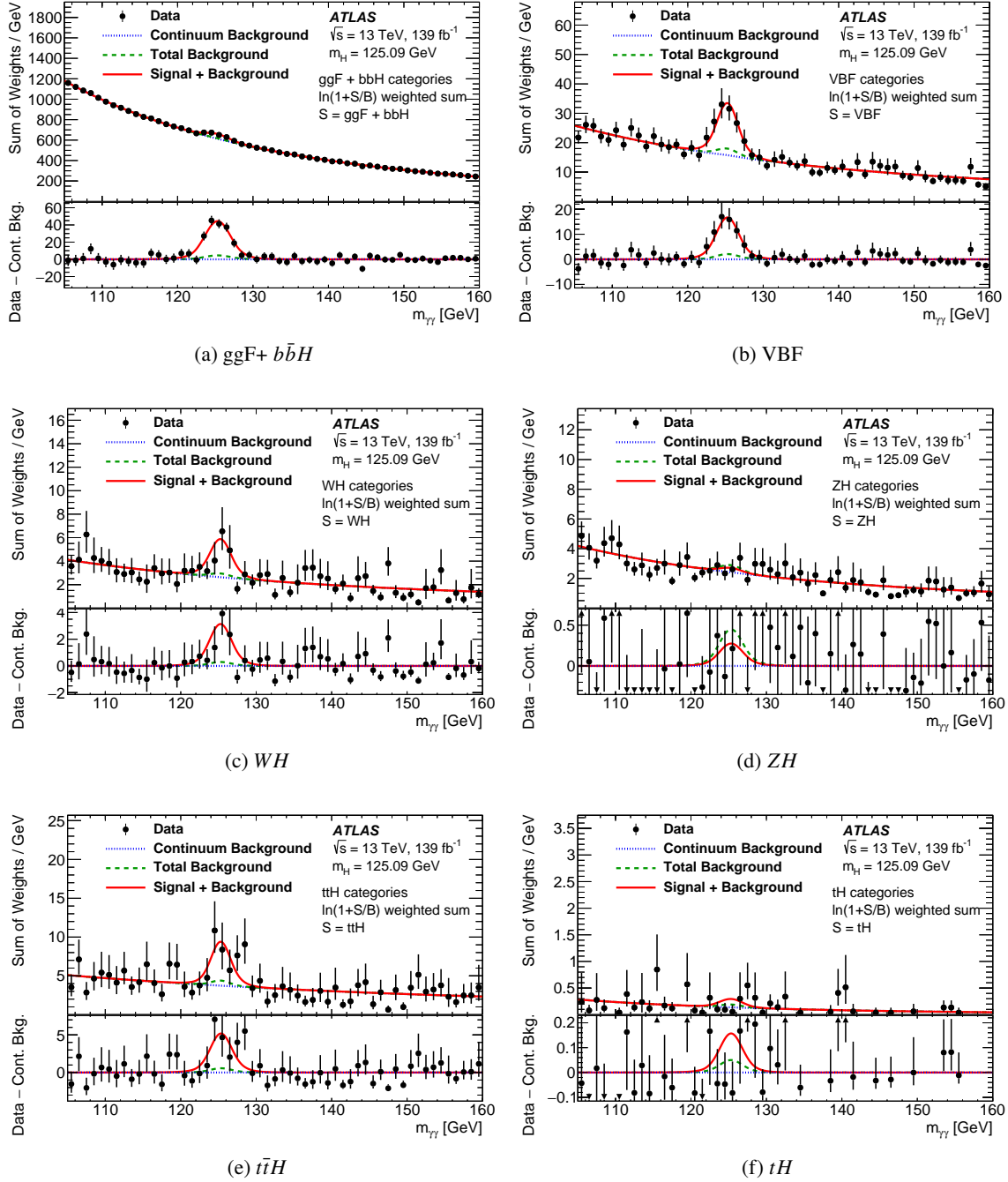


Figure 8: Combined diphoton invariant mass distributions for categories targeting the same production processes. The data (black dots) are weighted by $\ln(1 + S/B)$ where S and B are respectively the expected signal and background yields in the smallest $m_{\gamma\gamma}$ window containing 90% of the signal events. In this calculation, only Higgs boson events from the targeted production processes are considered as signal events. Higgs boson events from other processes as well as the continuum background events are considered as background. The fitted signal-plus-background pdfs from the relevant categories are summed, and represented by a solid line. The blue dotted line represents the weighted sum of the fitted continuum background pdfs, while the dashed line combines the contributions of continuum background and other Higgs boson events. The error bars on the data points are computed following Ref. [158]. The weighted combination of categories with low event counts leads in some cases to data errors that are highly asymmetric and change by large amounts from point to point.

Table 8: Summary of the leading sources of systematic uncertainty in the measurement of the Higgs boson signal strength.

Uncertainty source	$\Delta\mu$ [%]
Theory uncertainties	
Higher-Order QCD Terms	± 3.8
Branching Ratio	± 3.0
Underlying Event and Parton Shower	± 2.5
PDF and α_s	± 2.1
Matrix Element	± 1.0
Modeling of Heavy Flavor Jets in non- $t\bar{t}H$ Processes	$< \pm 1$
Experimental uncertainties	
Photon energy resolution	± 2.8
Photon efficiency	± 2.6
Luminosity	± 1.8
Pile-up	± 1.5
Background modelling	± 1.3
Photon energy scale	$< \pm 1$
Jet/ E_T^{miss}	$< \pm 1$
Flavour tagging	$< \pm 1$
Leptons	$< \pm 1$
Higgs boson mass	$< \pm 1$

rate of 10 times its SM prediction or greater at 95% CL while the expected 95% CL limit is 6.8 times the SM tH production cross-section.

8.4 Cross-sections in STXS regions

A measurement of the cross-sections defined in the STXS scheme is performed using the analysis regions described in Section 5. In order to avoid large uncertainties and large absolute correlations between the measurements, a set of measurement regions is obtained by merging some of the analysis regions as follows:

- For the $gg \rightarrow H$ process, within the phase space of ≥ 2 -jets, $m_{jj} < 350$ GeV, the two regions with $p_T^H < 60$ GeV and $60 \leq p_T^H < 120$ GeV are merged into one region corresponding to $p_T^H < 120$ GeV. Within ≥ 2 -jets, $p_T^H < 200$ GeV, the three bins defined in the m_{jj} variable are merged into a single $m_{jj} > 350$ GeV region. Finally, the $p_T^H > 650$ GeV bin is merged with the neighbouring $450 \leq p_T^H < 650$ GeV bin to form a single region corresponding to $p_T^H \geq 450$ GeV.
- For the $qq' \rightarrow Hqq'$ process, the 0-jet and 1-jet regions, as well as the regions corresponding to $m_{jj} < 60$ GeV and $120 < m_{jj} < 350$ GeV, are combined into a new region, referred to as $qq' \rightarrow Hqq'$, ≤ 1 -jet and VH -veto. The regions corresponding to ≥ 2 -jets, $p_T^H \geq 200$ GeV, $350 < m_{jj} < 1000$ GeV, are merged into a single region.

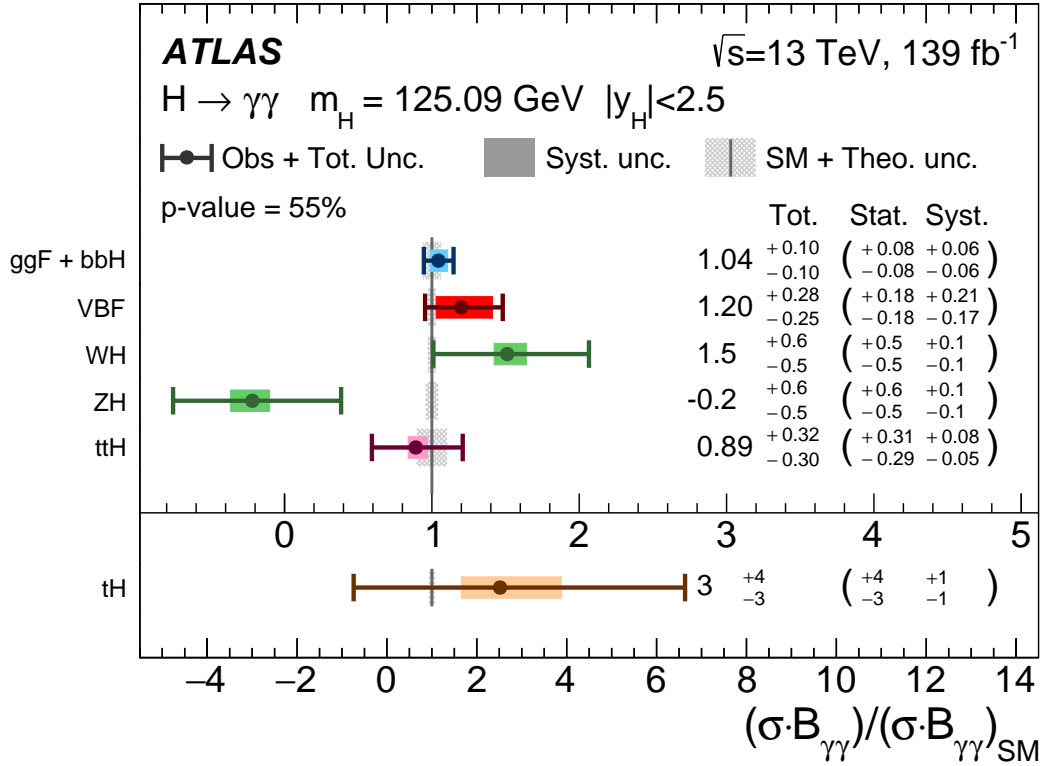


Figure 9: Cross-sections times $H \rightarrow \gamma\gamma$ branching ratio for ggF+ $b\bar{b}H$, VBF, VH , $t\bar{t}H$, and tH production, normalized to their SM predictions. The values are obtained from a simultaneous fit to all categories. The error bars and shaded areas show respectively the total and systematic uncertainties in the measurements. The grey bands show the theory uncertainties in the predictions, including uncertainties due to missing higher-order terms in the perturbative QCD calculations, the PDFs and the value of α_s , as well as the $H \rightarrow \gamma\gamma$ branching ratio uncertainty.

- For both the $q\bar{q}' \rightarrow WH$ and $pp \rightarrow ZH$ processes, only the two regions $p_T^V < 150 \text{ GeV}$ and $p_T^V \geq 150 \text{ GeV}$ are retained, removing the intermediate splits at $p_T^V = 75 \text{ GeV}$ and $p_T^V = 250 \text{ GeV}$. For $pp \rightarrow ZH$ processes, no distinction is made between regions with charged leptons and regions with neutrinos.
- The $tHqb$ and tHW regions are merged into a single tH region.

This scheme is based on the expected analysis sensitivity under the SM hypothesis, independently of the observed data, and is illustrated in Figure 11. The merging reduces the number of regions for which a measurement is reported to 28 in the scheme described above. The 101 categories in which the measurement is performed, described in Section 5.2, remain unchanged. The acceptance factors for merged STXS regions are computed as weighted averages of those for the original STXS regions, with the weights corresponding to the expected cross-sections in the SM. The acceptance uncertainty of the merged STXS region is then calculated from the uncertainties in the acceptance factors and expected cross-sections of the original STXS regions.

Results are shown in Table 10 and Figure 12. The correlation matrix of the measurements is shown in Figure 13. The correlation between most STXS region measurements is small, and the largest correlation is -51% , observed for the measurements of STXS regions $gg \rightarrow H, \geq 2\text{-jets}, m_{jj} \geq 350 \text{ GeV}, p_T^H < 200 \text{ GeV}$ and $qq' \rightarrow Hqq', \geq 2\text{-jets}, 350 \leq m_{jj} < 700 \text{ GeV}, p_T^H < 200 \text{ GeV}$. The Higgs boson production processes

Table 9: Best-fit values and uncertainties for the production cross-sections of the Higgs boson times the $H \rightarrow \gamma\gamma$ branching ratio. The total uncertainties are decomposed into statistical (Stat.) and systematic (Syst.) uncertainties. SM predictions are shown for the cross-section of each production process. These are obtained from the total cross-sections and associated uncertainties reported in Ref. [6], multiplied by an acceptance factor for the region $|y_H| < 2.5$ computed using the Higgs boson simulation samples described in Section 3.2.

Process ($ y_H < 2.5$)	Value [fb]	Uncertainty [fb]			SM pred. [fb]
		Total	Stat.	Syst.	
$ggF+b\bar{b}H$	106	+10 -10	+8 -8	+6 -6	102^{+6}_{-6}
VBF	9.5	+2.2 -1.9	+1.5 -1.4	+1.7 -1.4	$7.9^{+0.2}_{-0.2}$
WH	4.2	+1.5 -1.4	+1.5 -1.4	+0.4 -0.2	$2.8^{+0.1}_{-0.1}$
ZH	-0.4	+1.1 -1.0	+1.1 -1.0	+0.2 -0.3	$1.8^{+0.1}_{-0.1}$
$t\bar{t}H$	1.0	+0.4 -0.3	+0.3 -0.3	+0.1 -0.1	$1.1^{+0.1}_{-0.1}$
tH	0.5	+0.8 -0.6	+0.7 -0.6	+0.3 -0.2	$0.19^{+0.01}_{-0.02}$

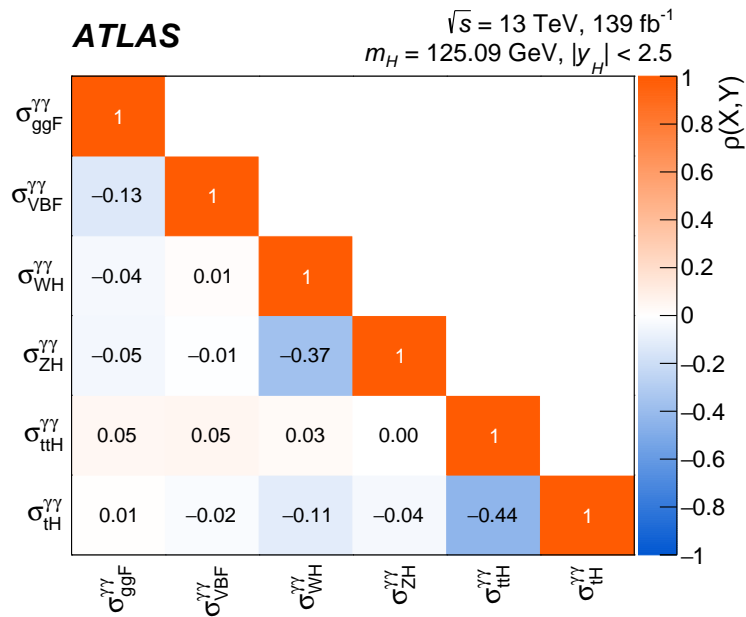


Figure 10: Correlation matrix for the measurement of production cross-sections of the Higgs boson times the $H \rightarrow \gamma\gamma$ branching ratio.

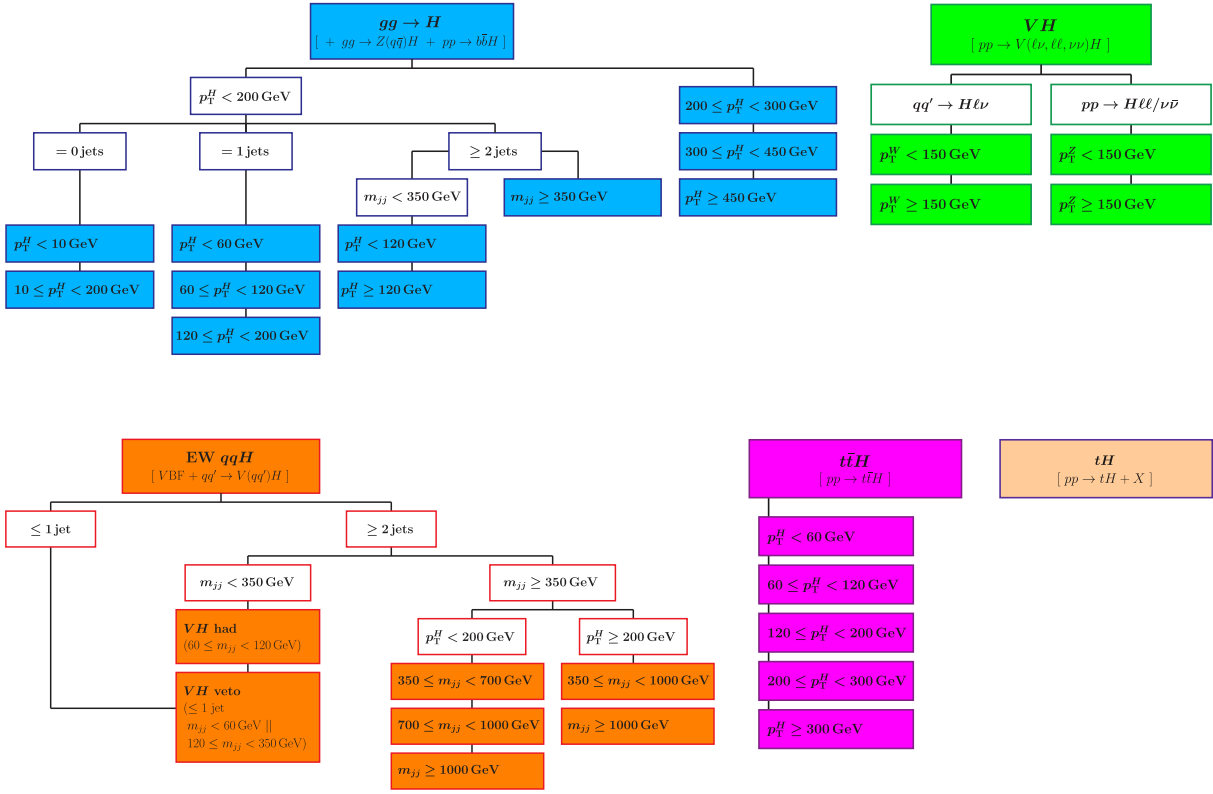


Figure 11: Summary of the 28 regions for which STXS measurements are reported.

in these STXS regions have similar event topologies and are intrinsically difficult to separate. The relative uncertainties in the measurements range from 20% to more than 100%. Smaller uncertainties are associated with the 0-jet and 1-jet regions of $gg \rightarrow H$, as well as the $200 \leq p_T^H < 300$ GeV region of $gg \rightarrow H$ and the $m_{jj} \geq 700$ GeV region of $qq' \rightarrow Hqq'$. Larger uncertainties occur especially in regions of high p_T^H and p_T^V , as well as the low- m_{jj} regions of $qq' \rightarrow Hqq'$. The systematic component of the uncertainties is everywhere smaller than the statistical component, but reaches similar values for the 0-jet regions of $gg \rightarrow H$. No significant deviations from the SM expectation are observed and the p -value for compatibility of the measurements and the SM predictions is 93%. Results in a finer set of 33 STXS measurements regions are also presented in Table 13 of Appendix A.

Table 10: Best-fit values and uncertainties for the production cross-section times $H \rightarrow \gamma\gamma$ branching ratio ($\sigma_i \times B_{\gamma\gamma}$) in each STXS region. The values for the $gg \rightarrow H$ process also include the contributions from $b\bar{b}H$ production. The total uncertainties are decomposed into statistical (Stat.) and systematic (Syst.) uncertainties. The uncertainties for the $pp \rightarrow H\ell\ell/\nu\bar{\nu}$, $p_T^V < 150$ GeV region are truncated at the value for which the model pdf becomes negative. SM predictions [6] are also shown for each quantity with their total uncertainties.

STXS region ($\sigma_i \times B_{\gamma\gamma}$)	Value	Uncertainty [fb]			SM prediction
	[fb]	Total	Stat.	Syst.	[fb]
$gg \rightarrow H$, 0-jet, $p_T^H < 10$ GeV	10	+4 -4	+4 -4	+2 -1	15^{+2}_{-2}
$gg \rightarrow H$, 0-jet, $p_T^H \geq 10$ GeV	58	+9 -8	+7 -7	+5 -4	47^{+4}_{-4}
$gg \rightarrow H$, 1-jet, $p_T^H < 60$ GeV	16	+5 -5	+5 -5	+2 -2	15^{+2}_{-2}
$gg \rightarrow H$, 1-jet, $60 \leq p_T^H < 120$ GeV	11	+4 -3	+3 -3	+2 -2	10^{+1}_{-1}
$gg \rightarrow H$, 1-jet, $120 \leq p_T^H < 200$ GeV	1.6	+0.9 -0.9	+0.9 -0.8	+0.4 -0.2	$1.7^{+0.3}_{-0.3}$
$gg \rightarrow H$, ≥ 2 -jets, $m_{jj} < 350$ GeV, $p_T^H < 120$ GeV	4	+4 -3	+3 -3	+1 -1	7^{+1}_{-1}
$gg \rightarrow H$, ≥ 2 -jets, $m_{jj} < 350$ GeV, $120 \leq p_T^H < 200$ GeV	2.8	+1.0 -1.0	+1.0 -1.0	+0.3 -0.2	$2.1^{+0.5}_{-0.5}$
$gg \rightarrow H$, ≥ 2 -jets, $m_{jj} \geq 350$ GeV, $p_T^H < 200$ GeV	2	+2 -2	+2 -2	+1 -1	$2.0^{+0.5}_{-0.5}$
$gg \rightarrow H$, $200 \leq p_T^H < 300$ GeV	1.6	+0.4 -0.4	+0.4 -0.4	+0.2 -0.1	$1.0^{+0.2}_{-0.2}$
$gg \rightarrow H$, $300 \leq p_T^H < 450$ GeV	0.04	+0.13 -0.11	+0.12 -0.11	+0.03 -0.03	$0.24^{+0.06}_{-0.06}$
$gg \rightarrow H$, $p_T^H \geq 450$ GeV	0.09	+0.06 -0.05	+0.06 -0.05	+0.02 -0.01	$0.04^{+0.01}_{-0.01}$
$qq' \rightarrow Hqq'$, ≤ 1 -jet and VH -veto	6	+6 -5	+6 -5	+2 -1	$6.6^{+0.2}_{-0.2}$
$qq' \rightarrow Hqq'$, VH -had	0.19	+0.85 -0.73	+0.83 -0.71	+0.17 -0.17	$1.16^{+0.04}_{-0.04}$
$qq' \rightarrow Hqq'$, ≥ 2 -jets, $350 \leq m_{jj} < 700$ GeV, $p_T^H < 200$ GeV	1.5	+0.9 -0.7	+0.7 -0.6	+0.6 -0.3	$1.22^{+0.04}_{-0.04}$
$qq' \rightarrow Hqq'$, ≥ 2 -jets, $700 \leq m_{jj} < 1000$ GeV, $p_T^H < 200$ GeV	0.8	+0.5 -0.4	+0.4 -0.3	+0.2 -0.1	$0.58^{+0.02}_{-0.02}$
$qq' \rightarrow Hqq'$, ≥ 2 -jets, $m_{jj} \geq 1000$ GeV, $p_T^H < 200$ GeV	1.2	+0.4 -0.4	+0.3 -0.3	+0.3 -0.2	$1.00^{+0.03}_{-0.03}$
$qq' \rightarrow Hqq'$, ≥ 2 -jets, $350 \leq m_{jj} < 1000$ GeV, $p_T^H \geq 200$ GeV	0.04	+0.12 -0.10	+0.12 -0.10	+0.02 -0.02	$0.167^{+0.005}_{-0.005}$
$qq' \rightarrow Hqq'$, ≥ 2 -jets, $m_{jj} \geq 1000$ GeV, $p_T^H \geq 200$ GeV	0.27	+0.11 -0.09	+0.10 -0.08	+0.05 -0.04	$0.166^{+0.005}_{-0.005}$
$qq \rightarrow H\ell\nu$, $p_T^V < 150$ GeV	1.4	+0.6 -0.6	+0.6 -0.6	+0.1 -0.1	$0.79^{+0.02}_{-0.02}$
$qq \rightarrow H\ell\nu$, $p_T^V \geq 150$ GeV	0.20	+0.13 -0.11	+0.13 -0.11	+0.02 -0.01	$0.121^{+0.005}_{-0.005}$
$pp \rightarrow H\ell\ell/\nu\bar{\nu}$, $p_T^V < 150$ GeV	-0.29	+0.40 -0.08	+0.39 -0.08	+0.07 -0.00	$0.45^{+0.02}_{-0.02}$
$pp \rightarrow H\ell\ell/\nu\bar{\nu}$, $p_T^V \geq 150$ GeV	0.04	+0.10 -0.08	+0.10 -0.08	+0.02 -0.02	$0.09^{+0.01}_{-0.01}$
$t\bar{t}H$, $p_T^H < 60$ GeV	0.22	+0.21 -0.18	+0.21 -0.18	+0.03 -0.01	$0.27^{+0.04}_{-0.04}$
$t\bar{t}H$, $60 \leq p_T^H < 120$ GeV	0.32	+0.23 -0.20	+0.23 -0.20	+0.04 -0.02	$0.40^{+0.05}_{-0.05}$
$t\bar{t}H$, $120 \leq p_T^H < 200$ GeV	0.18	+0.18 -0.15	+0.17 -0.15	+0.04 -0.02	$0.29^{+0.04}_{-0.04}$
$t\bar{t}H$, $200 \leq p_T^H < 300$ GeV	0.14	+0.09 -0.07	+0.09 -0.07	+0.01 -0.01	$0.12^{+0.02}_{-0.02}$
$t\bar{t}H$, $p_T^H \geq 300$ GeV	0.06	+0.05 -0.04	+0.05 -0.04	+0.01 -0.01	$0.06^{+0.01}_{-0.01}$
tH	0.4	+0.8 -0.6	+0.7 -0.6	+0.2 -0.2	$0.19^{+0.01}_{-0.02}$

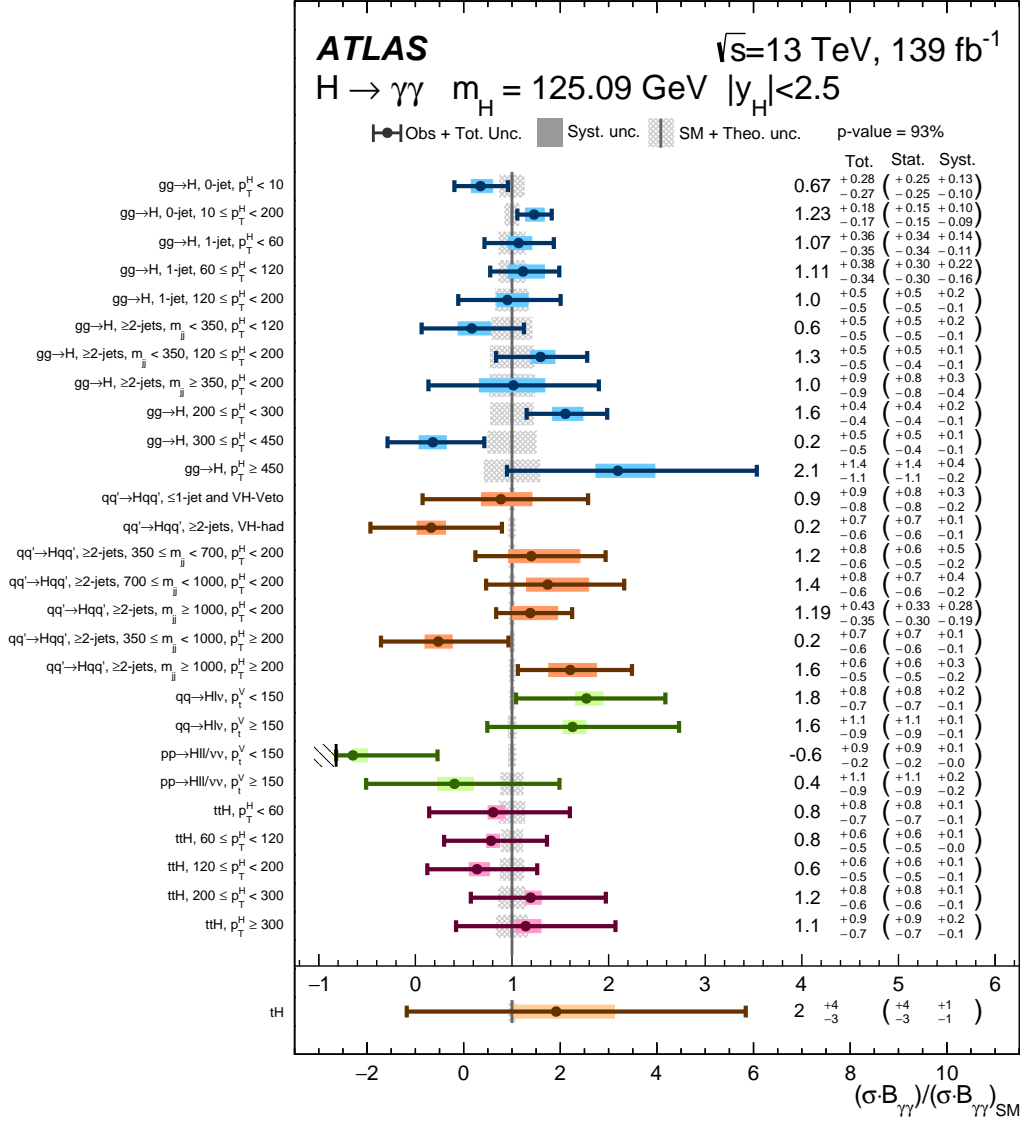


Figure 12: Best-fit values and uncertainties for STXS parameters in each of the 28 regions considered, normalized to their SM predictions. The values for the $gg \rightarrow H$ process also include the contributions from $b\bar{b}H$ production. The error bars and shaded areas show the total and systematic uncertainties in the measurements, respectively. The uncertainties for the $pp \rightarrow H\ell\ell/\nu\bar{\nu}$, $p_T^V < 150$ GeV region are truncated at the value for which the model pdf becomes negative. The grey bands around the vertical line at $\sigma^{\gamma\gamma}/\sigma_{SM}^{\gamma\gamma} = 1$ show the theory uncertainties in the predictions, including uncertainties due to missing higher-order terms in the perturbative QCD calculations, the PDFs and the value of α_s , as well as the $H \rightarrow \gamma\gamma$ branching ratio uncertainty. The p_T and m_{jj} values in the region definitions are indicated in GeV.

ATLAS

$\sqrt{s} = 13 \text{ TeV}, 139 \text{ fb}^{-1}$
 $m_H = 125.09 \text{ GeV}, |y_H| < 2.5$

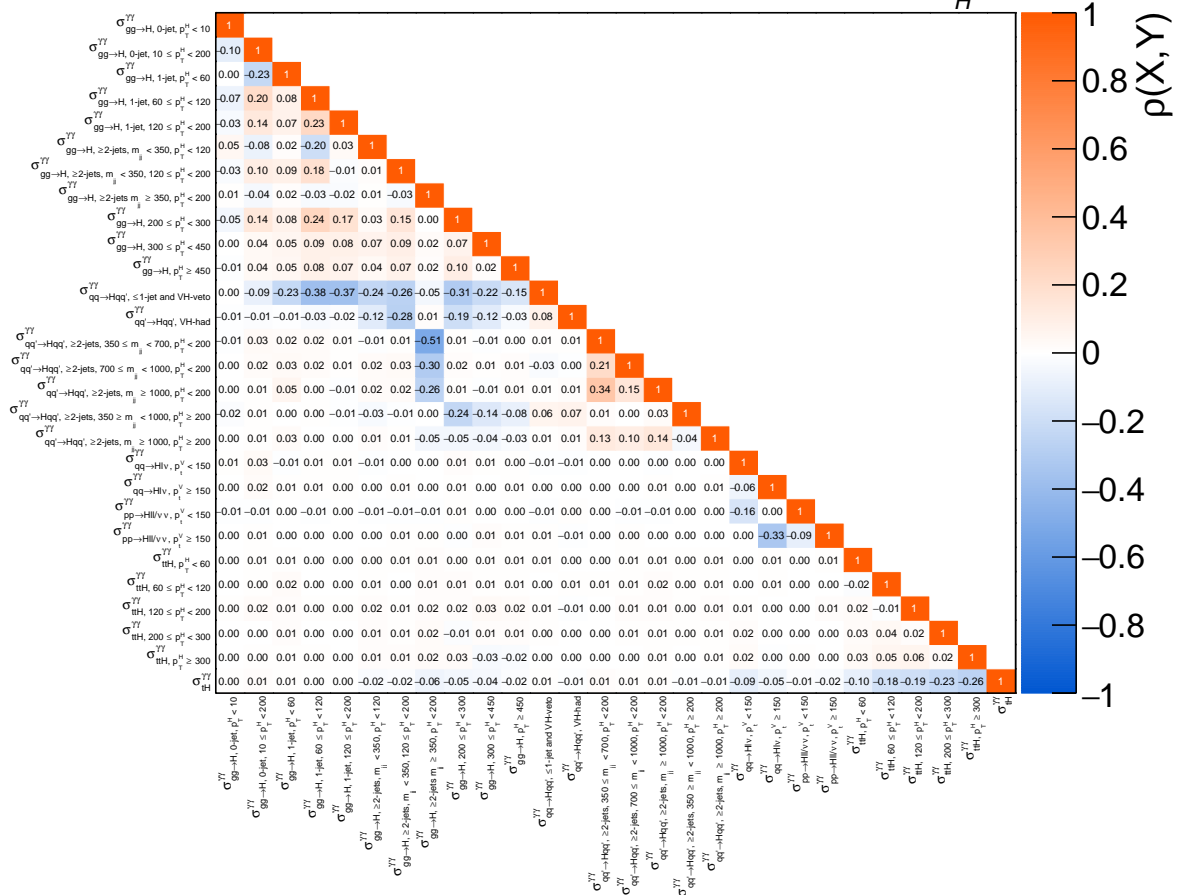


Figure 13: Correlation matrix for the measurement of STXS parameters in each of the 28 regions considered.

9 Interpretation of the results in the κ -framework

Event rates for processes involving Higgs bosons can be expressed in terms of modifiers applied to the SM Higgs boson couplings, based on the leading-order contributions to each process [6]. These coupling modifiers affect Higgs boson production cross-sections and decay partial widths and therefore provide a consistent framework for Higgs boson coupling measurements in both production and decay.

Multiplicative modifiers are introduced for Higgs boson couplings to the W and Z bosons, denoted respectively by κ_W and κ_Z , and for couplings to the charm, bottom and top quarks and muons and τ -leptons, respectively κ_c , κ_b , κ_t , κ_μ and κ_τ . Couplings to other SM particles are assumed to be equal to their SM predictions. Two parameterizations are considered for the $gg \rightarrow H$ and $H \rightarrow \gamma\gamma$ processes:

- A *resolved* parameterization in which they are assumed to proceed through the same loop amplitudes as in the SM at leading order. Their rates are expressed using the modifiers defined above, involving the particles appearing in the loop.
- An *effective* parameterization that makes no assumption about the internal structure of the interactions. Event rates are expressed using modifiers to the effective couplings of the Higgs boson to the gluon and the photon, respectively denoted by κ_g and κ_γ .

The $gg \rightarrow ZH$ loop process is always described in the resolved parameterization. The SM corresponds to the case $\kappa_W = \kappa_Z = \kappa_t = \kappa_b = \kappa_c = \kappa_\tau = \kappa_\mu = 1$, and in addition $\kappa_g = \kappa_\gamma = 1$ when effective parameterizations are used. The κ_Z modifier is assumed to be positive, without loss of generality, since all predictions are invariant under a simultaneous flip of the sign of each κ modifier. Sensitivity to the sign of the other modifiers is obtained through interference between processes involving different combinations of modifiers. These include, in particular, the $H \rightarrow \gamma\gamma$ and $gg \rightarrow H$ loops and the $gg \rightarrow ZH$ and tH processes.

The Higgs boson production cross-section in STXS region i followed by a $H \rightarrow \gamma\gamma$ decay is written in the narrow-width approximation as

$$\sigma_i \cdot B_{\gamma\gamma} = \frac{\sigma_i(\boldsymbol{\kappa}) \cdot \Gamma_{\gamma\gamma}(\boldsymbol{\kappa})}{\Gamma_H(\boldsymbol{\kappa})}$$

where σ_i is the production cross-section in region i , $B_{\gamma\gamma}$ and $\Gamma_{\gamma\gamma}$ are respectively the Higgs boson branching ratio and partial width into the $\gamma\gamma$ final state, and Γ_H is the total width of the Higgs boson. The parameterizations $\sigma_i(\boldsymbol{\kappa})$, $\Gamma_{\gamma\gamma}(\boldsymbol{\kappa})$ and $\Gamma_H(\boldsymbol{\kappa})$ are shown in Table 14 in Appendix B. They are similar to the ones used in Ref. [13], except for the parameterization of the tHW and $tHqb$ processes. These have been updated to reflect the fact that the acceptance factors in each analysis category depend on the κ_t and κ_W modifiers because of changes in the process kinematics caused by interference effects between the different parton-level processes contributing to tHW and $tHqb$. Separate parameterizations are therefore used in each analysis category for tHW and $tHqb$. The Higgs boson total width Γ_H is expressed as a function of the κ modifiers, assuming no contributions from Higgs boson decays other than the ones present in the SM. The SM predictions of $B_{\gamma\gamma}$ and the σ_i are taken from Ref [6]. These include the highest-order available computations in both the QCD and electroweak couplings.

Two specific models of coupling modifications are considered in this section, and two additional models are described in Appendix B. The first model focuses on the κ_t coupling modifier. Two configurations are used for the $gg \rightarrow H$ and $H \rightarrow \gamma\gamma$ loop processes: in the first case, both are described using their resolved parameterization as a function of κ_t ; in the second case, both are described using the effective couplings κ_g and κ_γ . All other κ modifiers are fixed to their SM values, in particular the effect of κ_W in the resolved

parameterization of the $H \rightarrow \gamma\gamma$ loop. These two models also allow the sign of κ_t to be probed, with sensitivity coming from interference effects in certain amplitudes. These occur in the tH and $gg \rightarrow ZH$ processes, as well as in the $H \rightarrow \gamma\gamma$ process when its parameterization is resolved in terms of κ_t and other coupling modifiers.

The negative log-likelihood scans for both configurations are shown in Figure 14. In both cases, good

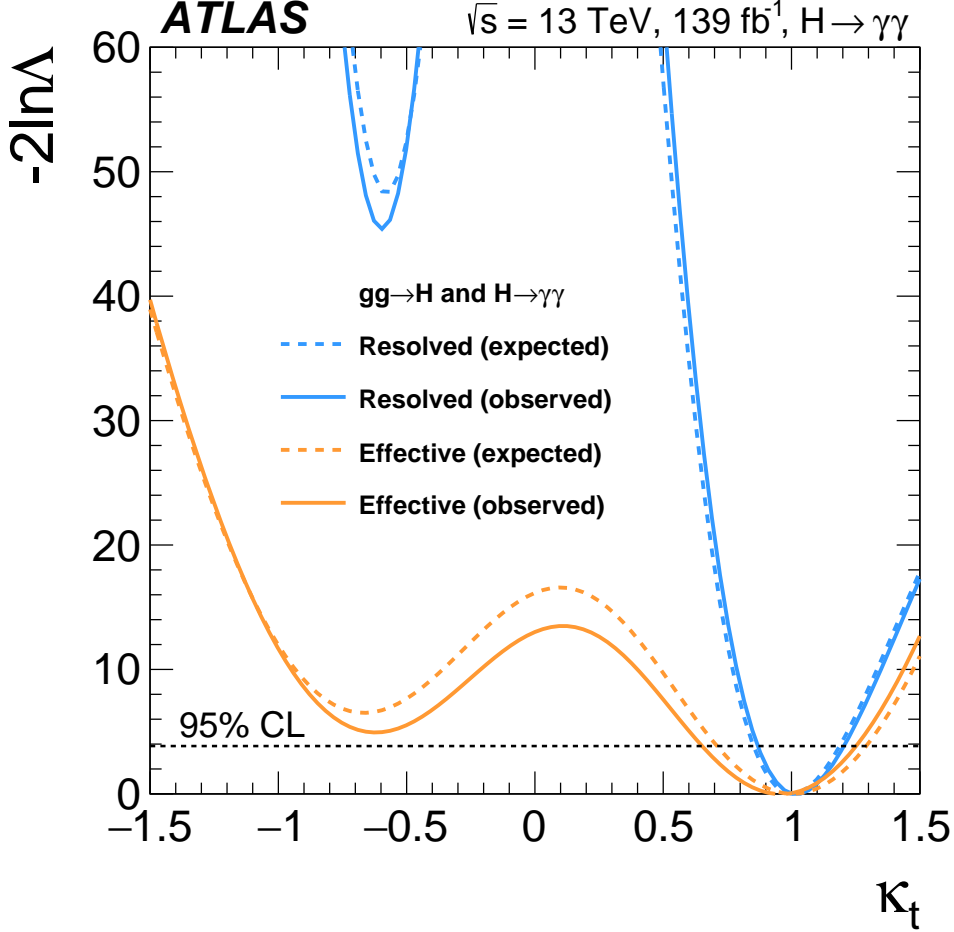


Figure 14: Negative log-likelihood scans as a function of κ_t in a model where other coupling modifiers are fixed to their SM values. The $H \rightarrow \gamma\gamma$ and $gg \rightarrow H$ loops are either parameterized as a function of κ_t (blue) or fixed to their SM expectation (orange). In the latter case, sensitivity to the sign of κ_t is provided by the tH process, and to a lesser degree by the $gg \rightarrow ZH$ process. The solid curves correspond to observed data, and the dotted curves to an Asimov data set generated under the SM hypothesis.

agreement with the SM expectation of $\kappa_t = 1$ is seen. When the $H \rightarrow \gamma\gamma$ and $gg \rightarrow H$ loops are resolved, negative values of κ_t are excluded with a significance of 6.7σ or above. When effective loop couplings are used, an exclusion of 2.2σ or above is observed through the sensitivity provided by the tH process, with a smaller contribution from the $gg \rightarrow ZH$ process. Values of κ_t outside of the range $0.87 < \kappa_t < 1.20$ are excluded at 95% CL in the first case ($0.85 < \kappa_t < 1.19$ expected under the SM hypothesis), as are values outside $0.65 < \kappa_t < 1.25$ in the second case ($0.71 < \kappa_t < 1.29$ expected).

In the second model, the $gg \rightarrow H$ and $H \rightarrow \gamma\gamma$ loop processes are described using the effective modifiers κ_g and κ_γ . Both modifiers are assumed to be positive, since the measurement provides no sensitivity to

their signs. Other modifiers are fixed to their SM values. The measurement in the plane of $(\kappa_g, \kappa_\gamma)$ is shown in Figure 15. The best-fit values are

$$\begin{aligned}\kappa_g &= 1.01^{+0.11}_{-0.09} \\ \kappa_\gamma &= 1.02^{+0.08}_{-0.07}.\end{aligned}$$

A linear correlation coefficient of -79% between the parameters is observed.

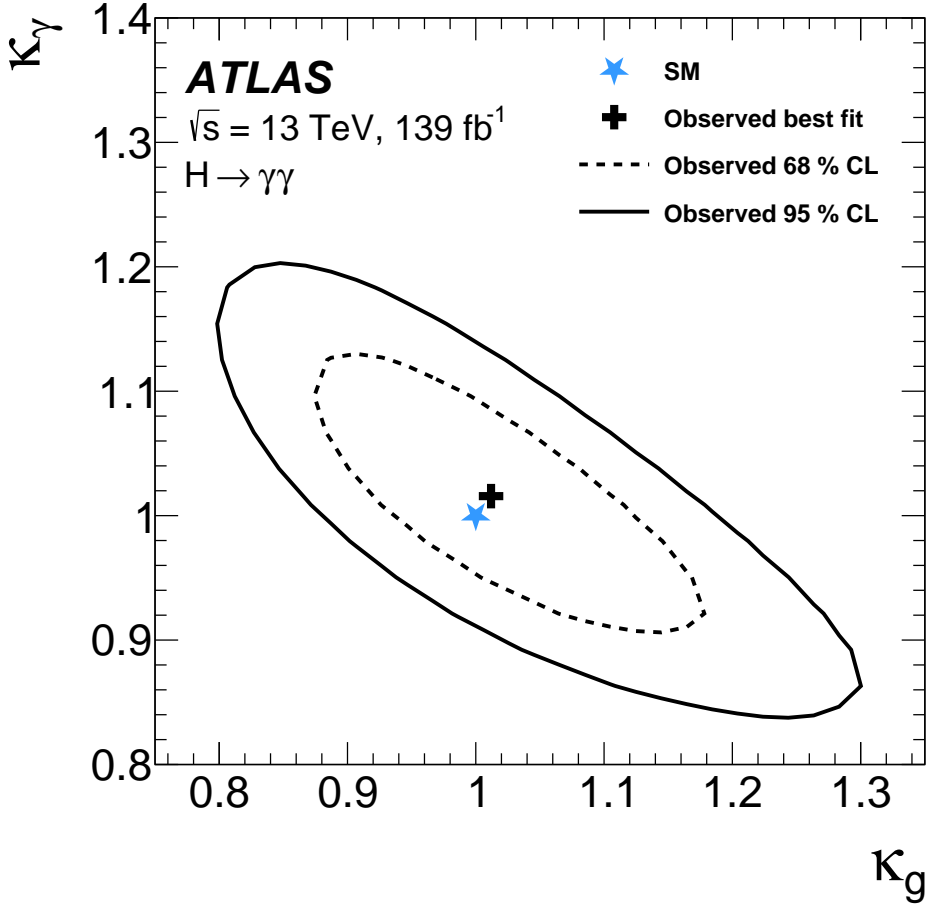


Figure 15: Negative log-likelihood contours at 68% (dashed line) and 95% CL (solid line) in the $(\kappa_g, \kappa_\gamma)$ plane, assuming that all other coupling-strength modifiers take their SM values. All other κ modifiers are fixed to their SM values. The best-fit point is indicated by a cross while the SM prediction is indicated by a star.

10 Interpretation of the results in the Standard Model effective field theory framework

10.1 Interpretation framework

The Standard Model effective field theory (SMEFT) framework provides a model-independent setting to describe deviations from SM predictions. New effective interactions involving Standard Model particles

are introduced in the Lagrangian to describe the effect of physics beyond the SM occurring above a high scale Λ . These interactions are considered order by order in the mass dimension d of the relevant operators, with leading-order effects occurring at $d = 6$ when assuming that the lepton number L and baryon number B are conserved.

The effective Lagrangian up to dimension 6 is written as

$$\mathcal{L} = \mathcal{L}_{\text{SM}} + \sum_k \frac{c_k}{\Lambda^2} O_k$$

where the sum runs over the dimension-6 operators O_k describing effective interactions in the SMEFT. The c_k are the corresponding Wilson coefficients, which are considered as the measurement parameters of the model. Subleading contributions with dimension 8 and above are neglected, and only operators with even CP quantum numbers that conserve B and L are considered. The selected operators are expressed in the Warsaw basis [26, 27]. The $U(3)^5$ -symmetric model of fermion flavour [28] is considered, assuming separate global flavour symmetries for each fermion type over the three fermion generations. In the cases where Wilson coefficients can have complex values, only their real parts are considered. The SM corresponds to all c_k set to 0. The c_k are defined for a scale $\Lambda = 1$ TeV.

The c_k are determined through an interpretation of the STXS results presented in Appendix A. This is achieved by expressing as functions of the c_k the signal-strength parameters

$$\mu_i^{\gamma\gamma} = \frac{\sigma_i \cdot B_{\gamma\gamma}}{\sigma_i^{\text{SM}} \cdot B_{\gamma\gamma}^{\text{SM}}},$$

where i runs over the 33 STXS regions listed in Table 13, and σ_i^{SM} and $B_{\gamma\gamma}^{\text{SM}}$ are the SM predictions for the production cross-section in STXS region i and the $H \rightarrow \gamma\gamma$ branching ratio, respectively. The 33 STXS regions used here correspond to a finer binning than the 28 regions for which results were reported in Section 8.4, and provide better granularity especially at high m_{jj} values in the $gg \rightarrow H$ and $qq' \rightarrow Hqq'$ processes.

SMEFT effects are modelled as single insertions of the operators O_k in each Higgs boson production and decay amplitude. These amplitudes are therefore linear in the c_k , so that the production cross-sections and decay widths are at most quadratic functions of the c_k . The signal strengths are thus written as

$$\mu_i^{\gamma\gamma} = \left(1 + \sum_k A_k^{i \rightarrow H} c_k + \sum_{kl} B_{kl}^{i \rightarrow H} c_k c_l \right) \frac{\left(1 + \sum_k A_k^{H \rightarrow \gamma\gamma} c_k + \sum_{kl} B_{kl}^{H \rightarrow \gamma\gamma} c_k c_l \right)}{\left(1 + \sum_k A_k^\Gamma c_k + \sum_{kl} B_{kl}^\Gamma c_k c_l \right)} \quad (2)$$

where $A_k^{i \rightarrow H}$, $A_k^{H \rightarrow \gamma\gamma}$ and A_k^Γ are respectively the coefficients describing the linear c_k -dependence of the production cross-section σ_i , the partial decay width $\Gamma_{\gamma\gamma}$ and the total width Γ_H . Similarly, the $B_{kl}^{i \rightarrow H}$, $B_{kl}^{H \rightarrow \gamma\gamma}$ and B_{kl}^Γ coefficients describe the quadratic dependence of the same quantities on the c_k .

Two SMEFT parameterizations are considered in the following: a *linear* parameterization including only the effect of the A coefficients and a *linear+quadratic* parameterization including both the A and B terms. In the linear case, Eq. (2) is linearized to first order in the c_k so that

$$\mu_i^{\gamma\gamma} = 1 + \sum_k \left[A_k^{i \rightarrow H} + A_k^{H \rightarrow \gamma\gamma} - A_k^\Gamma \right] c_k. \quad (3)$$

Results are derived using both parameterizations, and their difference is considered to be indicative of the impact of the neglected higher-order terms in the SMEFT expansion.

The values of the A and B coefficients are generally obtained using the SMEFT_{SIM} [28, 160] and SMEFT@NLO [161] programs. The coefficients are obtained by setting SMEFT parameters to non-zero values (one parameter at a time to compute A coefficients, and in pairs to compute B coefficients), and comparing the cross-sections obtained in this case with the ones for all coefficients set to 0. Events corresponding to each STXS region are selected using a RIVET routine [162]. SMEFT@NLO is used to obtain predictions for $gg \rightarrow H$ and $gg \rightarrow ZH$ loop processes, while SMEFT_{SIM} is used for all other processes. The dependence of the Higgs boson total decay width on the SMEFT parameters is computed by considering all decays of the Higgs boson with up to four particles in the final state. The A coefficients for the $H \rightarrow \gamma\gamma$ decay are taken from an analytic calculation [163], which includes NLO electroweak corrections that are not implemented in the programs mentioned above. The coefficients are obtained for the full phase space of the decay, relying on the fact that they are only weakly dependent on acceptance, as discussed below. The B coefficients for the $H \rightarrow \gamma\gamma$ decay are computed using SMEFT_{SIM}.

The SMEFT operators considered in the analysis are shown in Table 11. Initially, 60 operators are considered but only 34 are found to have significant impact in at least one STXS region or on the $H \rightarrow \gamma\gamma$ branching ratio, defined by a value above 0.01 for the corresponding A coefficient. Only these 34 operators are considered in the measurements presented in this paper. The impact of the most relevant SMEFT parameter in the measured STXS regions is summarized in Figure 16. The acceptance and efficiency factors which are applied to the observed event yields to obtain the $\mu_i^{\gamma\gamma}$ parameters, as shown in Eq. (1), can depend on the SMEFT parameters due to modifications of the Higgs signal characteristics within each STXS bin. The effect was studied for the main Warsaw basis operators affecting the measurement, and setting the corresponding Wilson coefficients to 1 individually is generally found to have an impact below 10% on the acceptance and efficiency factors. These changes are therefore neglected in the analysis.

10.2 Measurements of single SMEFT parameters

In the measurements presented in this section, one SMEFT parameter at a time is left free to vary, while the others are fixed to 0 as in the SM. This provides a measure of the sensitivity of the analysis for individual Wilson coefficients in the Warsaw basis, but the restrictive nature of this model limits the applicability of the measurements in probing effects beyond the SM.

The measurement results are summarized in Figure 17, and full results are provided in Table 16 in Appendix C. The SMEFT framework used in this measurement is considered valid only for parameter values of $O(10)$ or less, and confidence intervals that extend outside $|c_k| \leq 20$ are therefore not shown. Uncertainties in the parameter values range from below ± 0.01 to above the $|c_k| = 20$ threshold used to define the region of SMEFT validity. All values are compatible with the SM within measurement uncertainties. For parameters where the sensitivity mainly derives from inclusive event yields, such as c_{HG} , the linear and linear+quadratic parameterizations provide similar results. Conversely, operators with sensitivity to the high- p_T^H bins of the $t\bar{t}H$ or $gg \rightarrow H$ processes and the high- p_T^V regions of $q\bar{q}' \rightarrow VH$ show markedly smaller confidence intervals for the linear+quadratic case than for the linear case. The significant impact of the quadratic terms of the SMEFT parameterization in these cases may be indicative of significant effects from missing higher-order terms in the SMEFT expansion.

Table 11: Wilson coefficients c_i and corresponding dimension-6 SMEFT operators O_i used in this analysis. The notations follow that of Ref. [28]. Hermitian conjugates of non-Hermitian operators are implicitly considered in addition to the expression shown in the table. The operators indicated by a checkmark are the ones included in the measurement, due to having a significant impact on STXS cross-sections or on the $H \rightarrow \gamma\gamma$ branching ratio.

Coeff.	Operator	Incl.	Coeff.	Operator	Incl.
c_G	$f^{ABC} G_\mu^{Av} G_\nu^{B\rho} G_\rho^{C\mu}$	✓	$c_{qq}^{(3)}$	$(\bar{q}_r \gamma_\mu \tau^I q_r)(\bar{q}_s \gamma^\mu \tau^I q_s)$	✓
c_W	$\epsilon^{IJK} W_\mu^{I\nu} W_\nu^{J\rho} W_\rho^{K\mu}$	✓	$c_{qq}^{(3)'}$	$(\bar{q}_r \gamma_\mu \tau^I q_s)(\bar{q}_s \gamma^\mu \tau^I q_r)$	✓
c_H	$(H^\dagger H)^3$		$c_{qq}^{(1)}$	$(\bar{q}_r \gamma_\mu q_r)(\bar{q}_s \gamma^\mu q_s)$	✓
$c_{H\Box}$	$(H^\dagger H)\Box(H^\dagger H)$	✓	$c_{qq}^{(1)'}$	$(\bar{q}_r \gamma_\mu q_s)(\bar{q}_s \gamma^\mu q_r)$	✓
c_{HD}	$(H^\dagger D^\mu H)^*(H^\dagger D_\mu H)$	✓	$c_{lq}^{(3)}$	$(\bar{l}_r \gamma_\mu \tau^I l_r)(\bar{q}_s \gamma^\mu \tau^I q_s)$	
c_{HG}	$H^\dagger H G_{\mu\nu}^A G^{A\mu\nu}$	✓	$c_{lq}^{(1)}$	$(\bar{l}_r \gamma_\mu l_r)(\bar{q}_s \gamma^\mu q_s)$	
c_{HW}	$H^\dagger H W_{\mu\nu}^I W^{I\mu\nu}$	✓	c_{ee}	$(\bar{e}_r \gamma_\mu e_r)(\bar{e}_s \gamma^\mu e_s)$	
c_{HB}	$H^\dagger H B_{\mu\nu} B^{\mu\nu}$	✓	c_{eu}	$(\bar{e}_r \gamma_\mu e_r)(\bar{u}_s \gamma^\mu u_s)$	
c_{HWB}	$H^\dagger \tau^I H W_{\mu\nu}^I B^{\mu\nu}$	✓	c_{ed}	$(\bar{e}_r \gamma_\mu e_r)(\bar{d}_s \gamma^\mu d_s)$	
c_{eH}	$(H^\dagger H)(\bar{l}_p [Y_e^\dagger]_{pq} e_q H)$	✓	c_{uu}	$(\bar{u}_r \gamma_\mu u_r)(\bar{u}_s \gamma^\mu u_s)$	✓
c_{uH}	$(H^\dagger H)(\bar{q}_p [Y_u^\dagger]_{pq} u_q \tilde{H})$	✓	c'_{uu}	$(\bar{u}_r \gamma_\mu u_s)(\bar{u}_s \gamma^\mu u_r)$	✓
c_{dH}	$(H^\dagger H)(\bar{q}_p [Y_d^\dagger]_{pq} d_q H)$	✓	c_{dd}	$(\bar{d}_r \gamma_\mu d_r)(\bar{d}_s \gamma^\mu d_s)$	
c_{eW}	$(\bar{l}_p \sigma^{\mu\nu} [Y_e^\dagger]_{pq} e_q) \tau^I H W_{\mu\nu}^I$		c'_{dd}	$(\bar{d}_r \gamma_\mu d_s)(\bar{d}_s \gamma^\mu d_r)$	
c_{eB}	$(\bar{l}_p \sigma^{\mu\nu} [Y_e^\dagger]_{pq} e_q) H B_{\mu\nu}$		$c_{ud}^{(1)}$	$(\bar{u}_r \gamma_\mu u_r)(\bar{d}_s \gamma^\mu d_s)$	✓
c_{uG}	$(\bar{q}_p \sigma^{\mu\nu} T^A [Y_u^\dagger]_{pq} u_q) \tilde{H} G_{\mu\nu}^A$	✓	$c_{ud}^{(8)}$	$(\bar{u}_r \gamma_\mu T^A u_r)(\bar{d}_s \gamma^\mu T^A d_s)$	✓
c_{uW}	$(\bar{q}_p \sigma^{\mu\nu} [Y_u^\dagger]_{pq} u_q) \tau^I \tilde{H} W_{\mu\nu}^I$	✓	c_{le}	$(\bar{l}_r \gamma_\mu l_r)(\bar{e}_s \gamma^\mu e_s)$	
c_{uB}	$(\bar{q}_p \sigma^{\mu\nu} [Y_u^\dagger]_{pq} u_q) \tilde{H} B_{\mu\nu}$	✓	c_{lu}	$(\bar{l}_r \gamma_\mu l_r)(\bar{u}_s \gamma^\mu u_s)$	
c_{dG}	$(\bar{q}_p \sigma^{\mu\nu} T^A [Y_d^\dagger]_{pq} d_q) H G_{\mu\nu}^A$		c_{ld}	$(\bar{l}_r \gamma_\mu l_r)(\bar{d}_s \gamma^\mu d_s)$	
c_{dW}	$(\bar{q}_p \sigma^{\mu\nu} [Y_d^\dagger]_{pq} d_q) \tau^I H W_{\mu\nu}^I$		c_{qe}	$(\bar{q}_r \gamma_\mu q_r)(\bar{e}_s \gamma^\mu e_s)$	
c_{dB}	$(\bar{q}_p \sigma^{\mu\nu} [Y_d^\dagger]_{pq} d_q) H B_{\mu\nu}$		$c_{qu}^{(1)}$	$(\bar{q}_r \gamma_\mu q_r)(\bar{u}_s \gamma^\mu u_s)$	✓
$c_{Hl}^{(3)}$	$(H^\dagger i \overleftrightarrow{D}_\mu^I H)(\bar{l}_r \tau^I \gamma^\mu l_r)$	✓	$c_{qu}^{(8)}$	$(\bar{q}_r \gamma_\mu T^A q_r)(\bar{u}_s \gamma^\mu T^A u_s)$	✓
$c_{Hl}^{(1)}$	$(H^\dagger i \overleftrightarrow{D}_\mu H)(\bar{l}_r \gamma^\mu l_r)$	✓	$c_{qd}^{(1)}$	$(\bar{q}_r \gamma_\mu q_r)(\bar{d}_s \gamma^\mu d_s)$	✓
c_{He}	$(H^\dagger i \overleftrightarrow{D}_\mu H)(\bar{e}_r \gamma^\mu e_r)$	✓	$c_{qd}^{(8)}$	$(\bar{q}_r \gamma_\mu T^A q_r)(\bar{d}_s \gamma^\mu T^A d_s)$	✓
$c_{Hq}^{(3)}$	$(H^\dagger i \overleftrightarrow{D}_\mu^I H)(\bar{q}_r \tau^I \gamma^\mu q_r)$	✓	c_{ledq}	$(\bar{l}_p^j [Y_l^\dagger]_{pq} e_q)(\bar{d}_r [Y_d]_{rs} q_s^j)$	
$c_{Hq}^{(1)}$	$(H^\dagger i \overleftrightarrow{D}_\mu H)(\bar{q}_r \gamma^\mu q_r)$	✓	$c_{quqd}^{(1)}$	$(\bar{q}_p^j [Y_u^\dagger]_{pq} u_q) \epsilon_{jk} (\bar{q}_r^k [Y_d^\dagger]_{rs} d_s)$	
c_{Hu}	$(H^\dagger i \overleftrightarrow{D}_\mu H)(\bar{u}_r \gamma^\mu u_r)$	✓	$c_{quqd}^{(1)'}$	$(\bar{q}_p^j [Y_d^\dagger]_{ps} u_q) \epsilon_{jk} (\bar{q}_r^k [Y_u^\dagger]_{rq} d_s)$	
c_{Hd}	$(H^\dagger i \overleftrightarrow{D}_\mu H)(\bar{d}_r \gamma^\mu d_r)$	✓	$c_{quqd}^{(8)}$	$(\bar{q}_p^j T^A [Y_u^\dagger]_{pq} u_q) \epsilon_{jk} (\bar{q}_r^k T^A [Y_d^\dagger]_{rs} d_s)$	
c_{Hud}	$(H^\dagger i D_\mu H)(\bar{u}_p \gamma^\mu [Y_u Y_d^\dagger]_{pq} d_q)$		$c_{quqd}^{(8)'}$	$(\bar{q}_p^j T^A [Y_d^\dagger]_{ps} u_q) \epsilon_{jk} (\bar{q}_r^k T^A [Y_u^\dagger]_{rq} d_s)$	
c_{ll}	$(\bar{l}_r \gamma_\mu l_r)(\bar{l}_s \gamma^\mu l_s)$		$c_{lequ}^{(1)}$	$(\bar{l}_p^j [Y_e^\dagger]_{pq} e_q) \epsilon_{jk} (\bar{q}_r^k [Y_u^\dagger]_{rs} u_s)$	
c'_{ll}	$(\bar{l}_r \gamma_\mu l_s)(\bar{l}_s \gamma^\mu l_r)$	✓	$c_{lequ}^{(3)}$	$(\bar{l}_p^j \sigma^{\mu\nu} [Y_e^\dagger]_{ps} e_q) \epsilon_{jk} (\bar{q}_r^k \sigma_{\mu\nu} [Y_u^\dagger]_{rq} u_s)$	

ATLAS Simulation $\sqrt{s}=13$ TeV 139fb^{-1} $H \rightarrow \gamma\gamma$, $m_H = 125.09$ GeV, $\Lambda = 1$ TeV

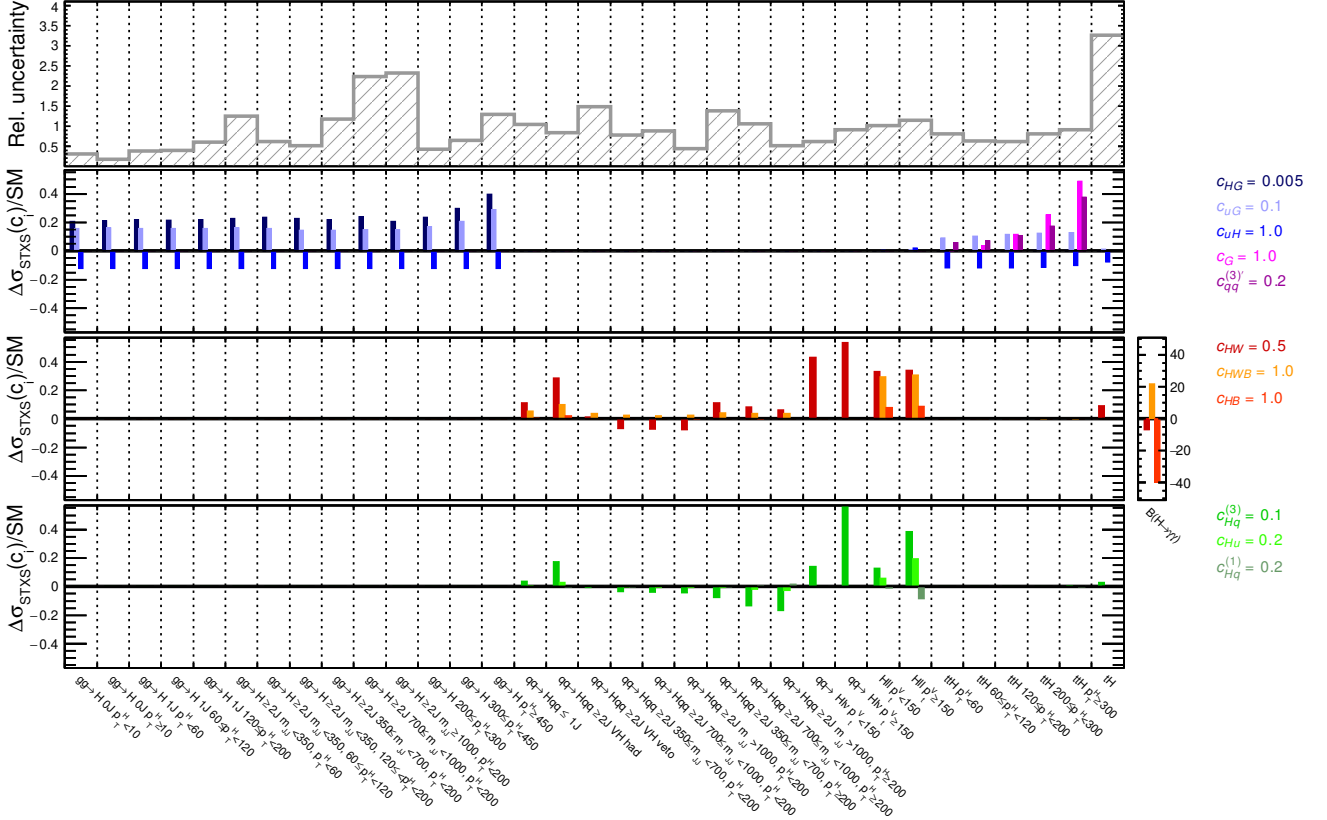


Figure 16: Relative impact of the most relevant SMEFT operators on the STXS regions and $H \rightarrow \gamma\gamma$ decay mode in the linear SMEFT model. Coloured bars indicate the relative impact of SMEFT parameters on the expected cross-section in the corresponding region. The impacts are computed for the parameter values shown on the right, relative to the SM prediction. The parameters are defined for a scale $\Lambda = 1$ TeV. Three sets of operators with similar impacts on the measurement are shown in separate panels: those with impact mainly on the $gg \rightarrow H$ and $t\bar{t}H$ processes (second from top), the $H \rightarrow \gamma\gamma$ decay (third from top), and VBF and VH processes (bottom). The expected total relative uncertainty in the measurement of the signal strength in each STXS region is shown in the top panel, as an indication of the experimental sensitivity of each region. The p_T and m_{jj} values in the region definitions are indicated in GeV, and the 0J, 1J and 2J shorthands refer respectively to the 0-jet, 1-jet and ≥ 2 -jets selections.

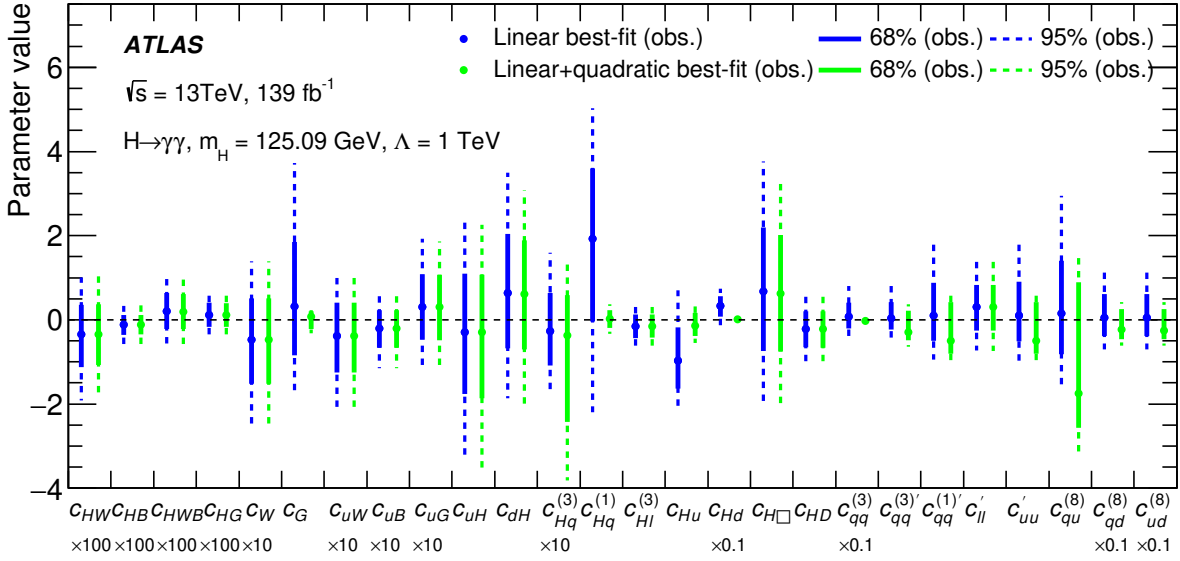


Figure 17: Summary of the 68% CL (solid lines) and 95% CL (dashed lines) intervals for individual measurements of SMEFT parameters observed in data. In each case, SMEFT parameters other than the one measured are fixed to 0. Blue and green curves correspond respectively to the linear and linear+quadratic SMEFT parameterizations. For presentation purposes, some parameters are scaled by a factor indicated below the parameter name. Results are not shown for coefficients c_k where one or more of the intervals extend beyond the $|c_k| \leq 20$ region, which is considered to be the region of validity of the SMEFT framework.

10.3 Simultaneous measurement of SMEFT parameters

In this section, multiple SMEFT parameters are left free to vary simultaneously. The information present in the STXS measurement does not, however, allow constraints to be placed simultaneously on all the SMEFT parameters listed in Table 11. In addition, both the constrained and the unconstrained degrees of freedom generally consist in combinations of parameters, since predictions in each STXS region are affected by multiple SMEFT operators.

Unconstrained directions can be removed from consideration without loss of generality, since the corresponding measurement information is in any case negligible. This allows the number of measurement parameters to be reduced without incurring model-dependence, and also avoids the probing of regions of parameter space beyond the bounds of SMEFT validity that occurs when confidence intervals along unconstrained directions extend beyond these bounds. Finally, this also avoids numerical issues in maximum-likelihood fits, since non-linear minimization algorithms can fail in cases where the local curvature of the likelihood function is too low.

The flat directions are identified by performing a principal component analysis of the information matrix C_{SMEFT}^{-1} of the SMEFT parameter measurement. The information matrix is computed using the linear model with the assumption that the probability distribution function of the STXS measurement is approximately Gaussian. It is obtained as

$$C_{\text{SMEFT}}^{-1} = P^T C_{\text{STXS}}^{-1} P$$

where C_{STXS}^{-1} is the information matrix of the STXS measurement, computed in an Asimov data set generated under the SM hypothesis, and P is the matrix representing the linear relation between the $\mu_i^{\gamma\gamma}$ and the c_k in the linear SMEFT parameterization, with components given by $P_{ik} = A_k^{i \rightarrow H} + A_k^{H \rightarrow \gamma\gamma} - A_k^\Gamma$ in the notation of Eq. (3).

A rotation is then performed to align the measurement parameters with the eigenvectors EV_n of C_{SMEFT}^{-1} . The unconstrained degrees of freedom of the measurement are identified with the eigenvectors corresponding to eigenvalues λ_n of C_{SMEFT}^{-1} with magnitude $\lambda_n < 0.005$. In the limit of a Gaussian measurement, each λ_n is the inverse square of the measurement uncertainty along the direction of the corresponding EV_n , so the threshold for λ_n corresponds to an uncertainty of about 14, which approximately corresponds to the region of SMEFT validity defined previously. The unconstrained EV_n parameters are fixed to 0 in the model, while the remaining 12 EV_n are considered as the measurement parameters. Their components along the c_k SMEFT parameters are shown in Figure 18. The full decomposition is shown in Table 17 of Appendix C.

The EV1 parameter is mainly sensitive to the total event rates; EV2 and EV8 to the difference between the rate of $gg \rightarrow H$ and of the other production modes; EV3 and EV7 to the high- p_T^V regions of the $pp \rightarrow VH$ processes; EV4 and EV5 to the high- p_T^H regions of the $t\bar{t}H$ process; and EV6 to the rate of the $qq' \rightarrow Hqq'$ process. Best-fit values and confidence intervals for each EV_n parameter are shown in Table 12 and

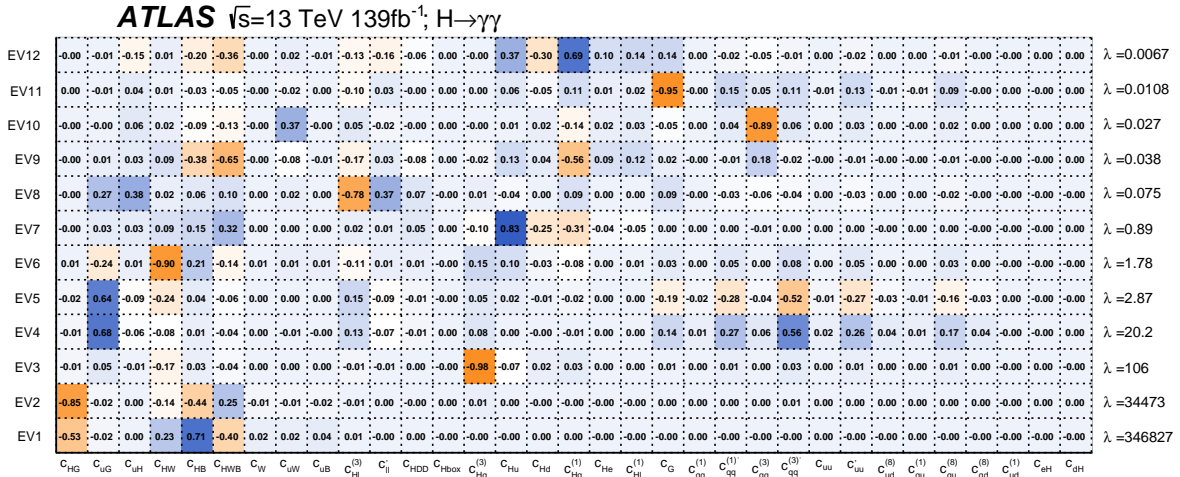


Figure 18: Components of the EV_n parameters (y-axis) along each of the Warsaw-basis Wilson coefficients (x-axis). The EV_n are normalized to unit Euclidean norm. Coefficients below 0.01 are not shown. The Warsaw-basis Wilson coefficients are defined for a scale $\Lambda = 1$ TeV. The information-matrix eigenvalues (λ_n) corresponding to each eigenvector are shown on the right side of the plot.

illustrated in Figure 19. No significant deviation from the SM is observed. In the linear parameterization, expected signal yields can become negative for some values of the SMEFT parameters, leading in some cases to a negative value of the model pdf, which invalidates the profile-likelihood computation. In these cases, the bounds of the confidence intervals are truncated at the point at which the pdf reaches 0. Results in the linear+quadratic parameterization are not affected since the expected signal yields are always positive by construction.

Profile likelihood scans for selected EV_n parameters are shown for illustration in Figure 20. For some parameters, such as EV1, a broad shape is seen in the expected scan in the SM hypothesis for the

linear+quadratic parameterization. This is caused in part by the presence of two degenerate minima, due to the quadratic dependence of the expected yields on the SMEFT parameters. The degeneracy is partially lifted by the fact that the observed data do not exactly correspond to the SM expectation, which leads to narrower profiles in the observed scans. Similar scans are performed for eigenvectors corresponding to unconstrained directions with eigenvalues below 0.01, with the measured EV_n also free to vary in the fits. The scans show that the measurement sensitivity in each of these directions is negligible.

The correlation matrix of the measurement is shown in Figure 21. Non-zero values outside the diagonal are due to differences between the observed results and their expectations, and to the fact that the information matrix used in the principal component analysis is not an exact representation of the measurement, due to non-Gaussian effects. In the linear parameterization, these include in particular the effect of low expected event counts in some categories and the non-linear impact of some systematic uncertainties. In the linear+quadratic case, larger correlations are observed due to the effect of the quadratic terms, which are not considered in the principal component analysis. These correlations also contribute to the larger uncertainties reported in Table 12 for some EV_n parameters in the linear+quadratic parameterization, compared to the linear parameterization, and to the wider contours visible in Figure 20 for the linear+quadratic case. Linear parameterization results including corrections to the propagators of off-shell W and Z bosons, the Higgs bosons and the top quarks, as implemented in the SMEFTsim generator [28] are shown in Appendix C.3.

Table 12: Summary of the EV_n parameter measurements in the linear and linear+quadratic parameterizations. The ranges correspond to 68% CL intervals. All the EV_n parameters are free to vary in the fits. The upper bound of the intervals reported for EV9 and EV12 in the linear parameterization (shown in bold text) are truncated at the value for which the model pdf becomes negative.

Parameter	Linear		Linear+quadratic	
	Value	Uncertainty	Value	Uncertainty
EV1	-0.0008	+0.0017 -0.0018	0.0043	+0.0067 -0.0095
EV2	0.0004	+0.0059 -0.0055	-0.0061	+0.0084 -0.0086
EV3	0.039	+0.095 -0.10	0.035	+0.11 -0.081
EV4	-0.035	+0.25 -0.22	-0.079	+0.29 -0.35
EV5	-0.22	+0.59 -0.62	0.29	+0.30 -0.69
EV6	0.19	+0.81 -0.80	0.011	+0.79 -0.47
EV7	-1.7	+1.0 -0.96	-0.91	+1.2 -0.53
EV8	-0.65	+3.5 -3.2	-1.2	+2.5 -1.0
EV9	7.5	+2.5 -5.2	1.7	+1.4 -1.6
EV10	0.48	+6.7 -8.5	0.42	+0.46 -0.60
EV11	-5.6	+9.4 -9.6	0.045	+0.47 -0.21
EV12	2.6	+12 -13	1.2	+0.81 -1.0

ATLAS $\sqrt{s}=13$ TeV 139fb^{-1} ; $H\rightarrow\gamma\gamma$; SMEFT Interpretation; $\Lambda=1$ TeV

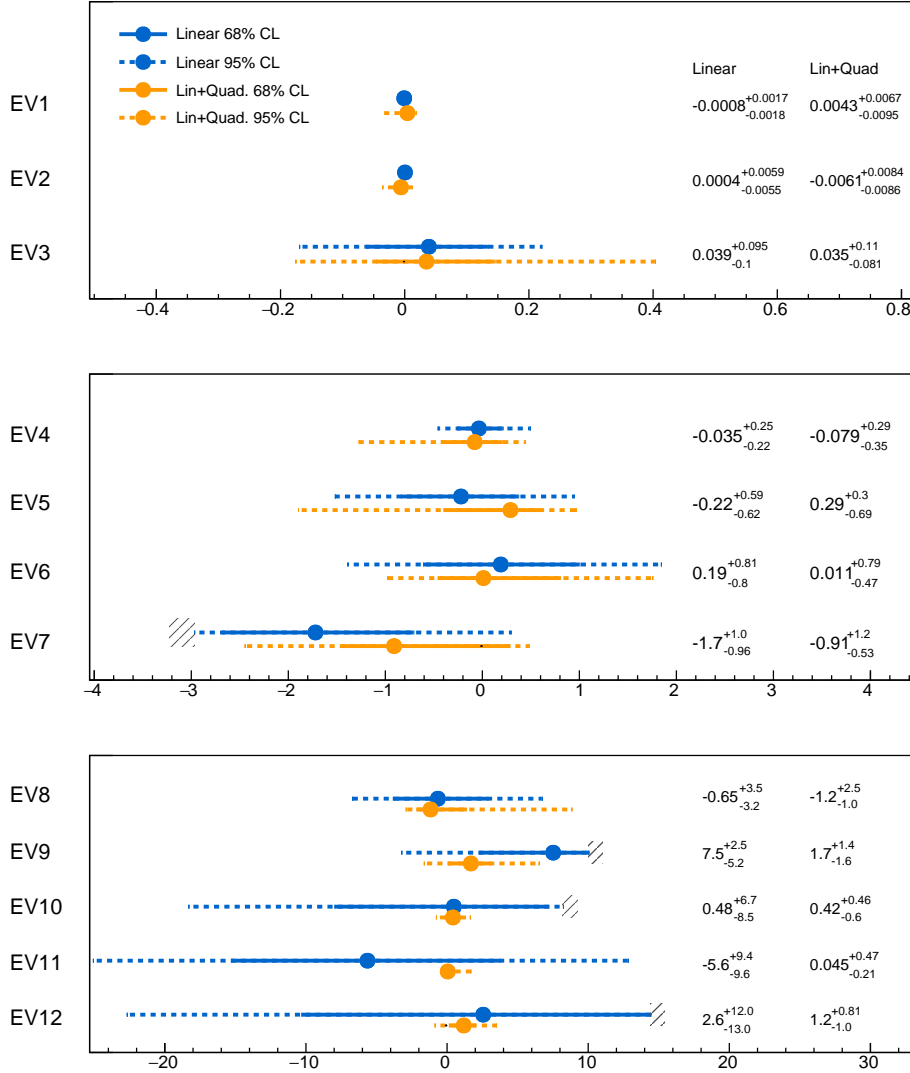


Figure 19: Results of the EV_n parameter measurement in data, in the linear (blue) and linear+quadratic (orange) parameterizations of the SMEFT. All the EV_n parameters are free to vary in the fits. The ranges shown correspond to 68% CL (solid) and 95% CL (dashed) intervals. Cases where the intervals are truncated due to a negative model pdf are indicated by hashes.

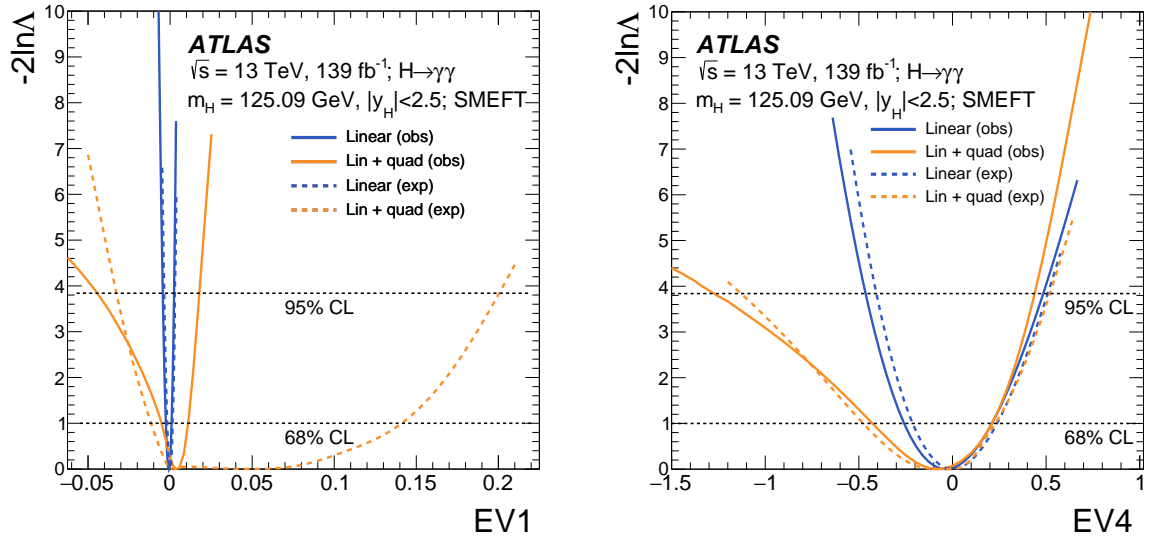


Figure 20: Profile likelihood scans for the measurements of the EV1 (left) and EV4 (right) parameters in data. All measured EV_n parameters are free to vary in the fit. The blue and orange curves correspond respectively to the linear and linear+quadratic parameterizations. The dotted horizontal lines show the $-2 \ln \Lambda = 1$ and $-2 \ln \Lambda = 3.84$ levels that are used to define respectively the 68% CL and 95% CL intervals in the parameters.

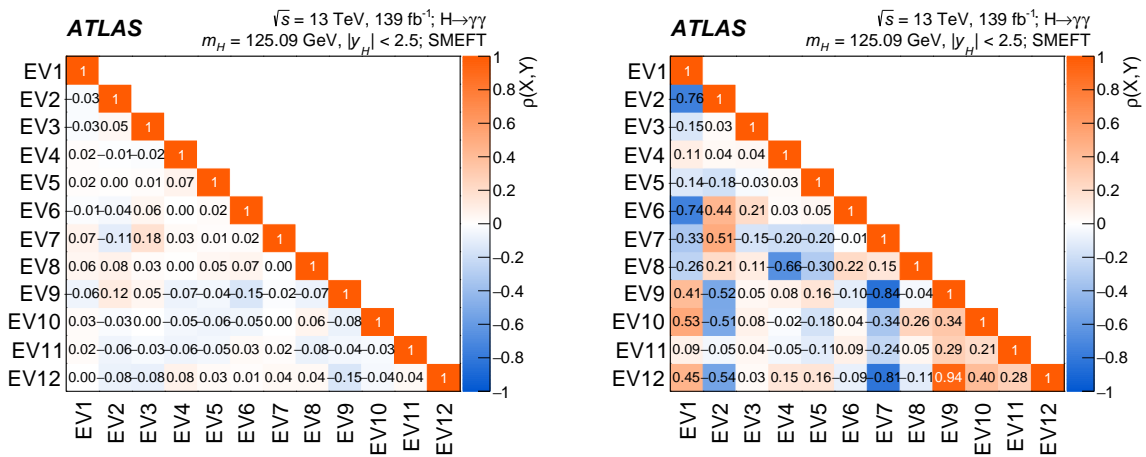


Figure 21: Observed linear correlation coefficients of the EV_n parameters in the linear (left) and linear+quadratic (right) parameterization.

11 Conclusion

Higgs boson production is measured in the diphoton decay channel using 139 fb^{-1} of 13 TeV proton–proton collision data, corresponding to the full data set collected by ATLAS during Run 2 of the LHC.

The overall Higgs boson signal strength relative to its SM prediction is measured to be

$$\mu = 1.04_{-0.09}^{+0.10} = 1.04 \pm 0.06 \text{ (stat.)}_{-0.05}^{+0.06} \text{ (theory syst.)}_{-0.04}^{+0.05} \text{ (exp. syst.)}.$$

in good agreement with the SM.

Cross-sections for $\text{ggF} + b\bar{b}H$, VBF, WH , ZH , $t\bar{t}H$ and tH production are reported, with relative uncertainties of 10% for $\text{ggF} + b\bar{b}H$, 22% for VBF, and 35% for WH and $t\bar{t}H$. An upper limit of ten times the SM prediction is set for the tH process. This represents the most stringent experimental constraint on tH production, superseding the previous ATLAS result from Run 2. A fine-grained description of Higgs boson production is provided by cross-section measurements in 28 phase-space regions defined within the STXS framework, including additional measurements at high values of p_{T}^H and m_{jj} compared to previous analyses. These measurements benefit from significant analysis improvements compared to previous ATLAS results [10]. A detailed classification of selected events into 101 separate categories based on multi-class machine learning techniques is used, and the uncertainties relative to the modeling of the continuum have been reduced through the use of Gaussian kernel smoothing.

Results are interpreted in models of Higgs boson coupling modifiers. All couplings are found to be compatible with their SM values. Sensitivity to the sign of the κ_t modifier to the top quark coupling in the tH process leads to an exclusion of the $\kappa_t < 0$ region with a significance of 2.2σ . An interpretation in the framework of SM effective field theory is used to set constraints on physics effects beyond the SM. Individual Wilson coefficients are measured while fixing the others to 0. A simultaneous measurement of the linear combinations of Wilson coefficients that the STXS measurements are sensitive to is also performed. All results are in agreement with SM expectations.

Appendix

A Additional production mode cross-section and STXS measurement results

Table 13 shows STXS results with a higher granularity than the baseline results presented in Section 8.4. A total of 33 regions are measured, with the following changes compared to the 28 regions in the baseline measurement:

- For the $gg \rightarrow H$ process, within the phase space of ≥ 2 -jets, $m_{jj} < 350$ GeV, the two regions with $p_{\text{T}}^H < 60$ GeV and $60 \leq p_{\text{T}}^H < 120$ GeV are kept separate. The same also applies to the three bins in the m_{jj} variable within the ≥ 2 -jets, $p_{\text{T}}^H < 200$ GeV region, which are not merged. Compared to the STXS analysis regions defined in Section 5.1, the only merging that is performed is that of the $p_{\text{T}}^H > 650$ GeV bin with the neighbouring $450 \leq p_{\text{T}}^H < 650$ GeV bin.
- For the $qq' \rightarrow Hqq'$ process, the 0-jet and 1-jet regions are merged into a single ≤ 1 -jet bin, and the $m_{jj} < 60$ GeV and $120 < m_{jj} < 350$ GeV regions are also combined into a new VH -veto region, but the two sets are not merged together as in the baseline results. The three regions in the m_{jj} variables within ≥ 2 -jets, $p_{\text{T}}^H \geq 200$ GeV, are also not merged.

The correlation matrix of the measurement is shown in Fig. 22.

ATLAS

$\sqrt{s} = 13 \text{ TeV}, 139 \text{ fb}^{-1}$
 $m_H = 125.09 \text{ GeV}, |y_H| < 2.5$

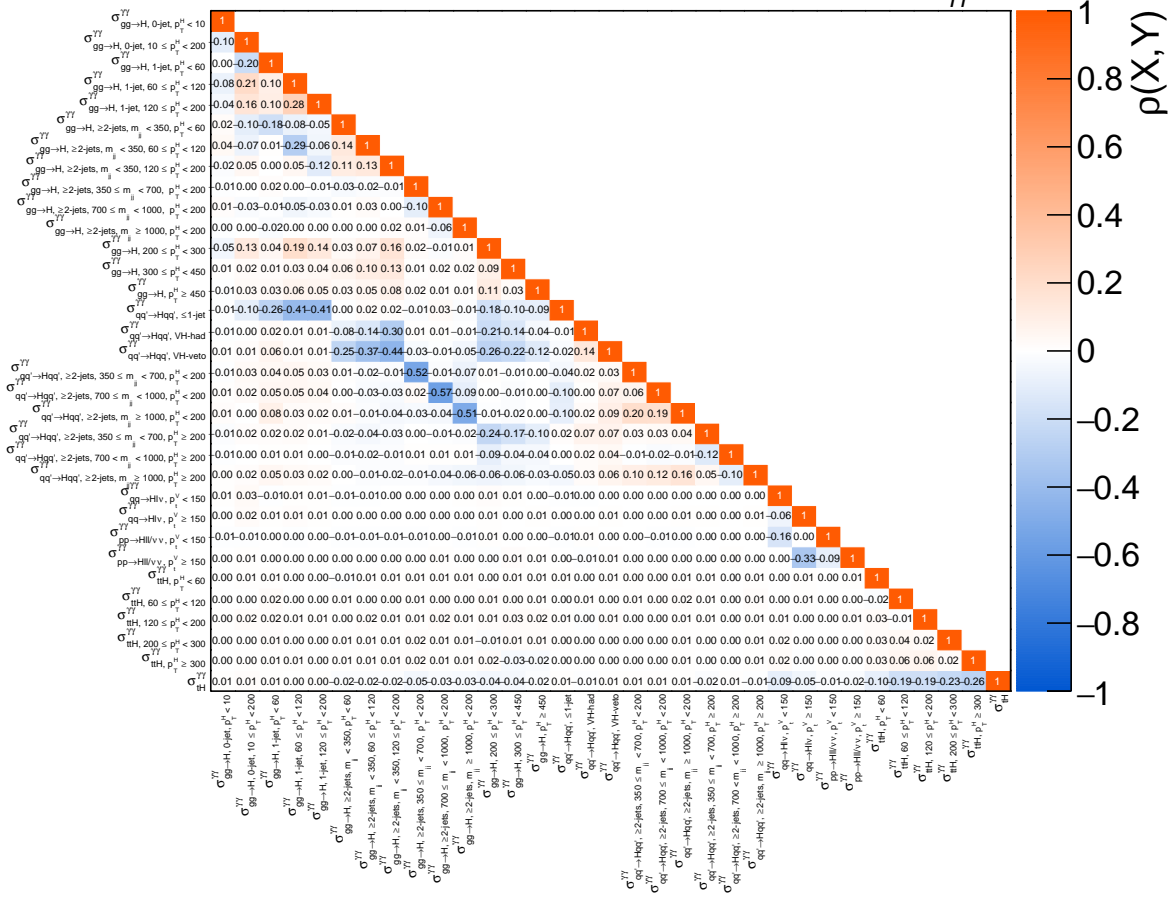


Figure 22: Correlation matrix for the measurement of STXS parameters in each of the 33 regions considered.

Table 13: Best-fit values and uncertainties for the production cross-section times $H \rightarrow \gamma\gamma$ branching ratio ($\sigma_i \times B_{\gamma\gamma}$) in each STXS region. The values for the $gg \rightarrow H$ process also include the contributions from $b\bar{b}H$ production. The total uncertainties are decomposed into components for data statistics (Stat.) and systematic uncertainties (Syst.). SM predictions [6] are also shown for each quantity with their total uncertainties.

STXS region ($\sigma_i \times B_{\gamma\gamma}$)	Value [fb]	Uncertainty [fb]			SM prediction [fb]
		Total	Stat.	Syst.	
$gg \rightarrow H$, 0-jet, $p_T^H < 10$ GeV	10	+4 -4	+4 -4	+2 -1	15^{+2}_{-2}
$gg \rightarrow H$, 0-jet, $p_T^H \geq 10$ GeV	59	+9 -8	+7 -7	+5 -4	47^{+4}_{-4}
$gg \rightarrow H$, 1-jet, $p_T^H < 60$ GeV	17	+6 -5	+5 -5	+2 -2	15^{+2}_{-2}
$gg \rightarrow H$, 1-jet, $60 \leq p_T^H < 120$ GeV	13	+4 -4	+3 -3	+2 -2	10^{+1}_{-1}
$gg \rightarrow H$, 1-jet, $120 \leq p_T^H < 200$ GeV	1.9	+1.0 -0.9	+0.9 -0.9	+0.4 -0.2	$1.7^{+0.3}_{-0.3}$
$gg \rightarrow H$, ≥ 2 -jets, $m_{jj} < 350$ GeV, $p_T^H < 60$ GeV	0.3	+3.1 -2.9	+2.9 -2.8	+1.1 -0.5	$2.7^{+0.6}_{-0.6}$
$gg \rightarrow H$, ≥ 2 -jets, $m_{jj} < 350$ GeV, $60 \leq p_T^H < 120$ GeV	1.3	+2.5 -2.5	+2.4 -2.4	+0.7 -0.6	$4.1^{+0.9}_{-0.9}$
$gg \rightarrow H$, ≥ 2 -jets, $m_{jj} < 350$ GeV, $120 \leq p_T^H < 200$ GeV	2.2	+1.1 -1.1	+1.1 -1.0	+0.3 -0.2	$2.1^{+0.5}_{-0.5}$
$gg \rightarrow H$, ≥ 2 -jets, $350 \leq m_{jj} < 700$ GeV, $p_T^H < 200$ GeV	2.7	+1.6 -1.5	+1.5 -1.5	+0.5 -0.3	$1.4^{+0.3}_{-0.3}$
$gg \rightarrow H$, ≥ 2 -jets, $700 \leq m_{jj} < 1000$ GeV, $p_T^H < 200$ GeV	-0.2	+0.7 -0.8	+0.7 -0.7	+0.2 -0.3	$0.3^{+0.10}_{-0.10}$
$gg \rightarrow H$, ≥ 2 -jets, $m_{jj} \geq 1000$ GeV, $p_T^H < 200$ GeV	-0.3	+0.6 -0.6	+0.6 -0.5	+0.2 -0.2	$0.28^{+0.08}_{-0.08}$
$gg \rightarrow H$, $200 \leq p_T^H < 300$ GeV	1.5	+0.5 -0.4	+0.4 -0.4	+0.2 -0.1	$1.0^{+0.2}_{-0.2}$
$gg \rightarrow H$, $300 \leq p_T^H < 450$ GeV	0.01	+0.13 -0.12	+0.13 -0.11	+0.03 -0.04	$0.24^{+0.06}_{-0.06}$
$gg \rightarrow H$, $p_T^H \geq 450$ GeV	0.08	+0.06 -0.05	+0.06 -0.05	+0.02 -0.01	$0.04^{+0.01}_{-0.01}$
$qq' \rightarrow Hqq'$, ≤ 1 -jet	0.7	+4.9 -4.4	+4.8 -4.2	+1.2 -1.4	$4.9^{+0.2}_{-0.2}$
$qq' \rightarrow Hqq'$, VH -veto	4	+3 -3	+3 -2	+1 -1	$1.67^{+0.05}_{-0.05}$
$qq' \rightarrow Hqq'$, VH -had	0.4	+0.9 -0.8	+0.9 -0.7	+0.2 -0.2	$1.16^{+0.04}_{-0.04}$
$qq' \rightarrow Hqq'$, ≥ 2 -jets, $350 \leq m_{jj} < 700$ GeV, $p_T^H < 200$ GeV	1.2	+0.9 -0.7	+0.8 -0.7	+0.5 -0.2	$1.22^{+0.04}_{-0.04}$
$qq' \rightarrow Hqq'$, ≥ 2 -jets, $700 \leq m_{jj} < 1000$ GeV, $p_T^H < 200$ GeV	1.1	+0.6 -0.5	+0.5 -0.4	+0.4 -0.2	$0.58^{+0.02}_{-0.02}$
$qq' \rightarrow Hqq'$, ≥ 2 -jets, $m_{jj} \geq 1000$ GeV, $p_T^H < 200$ GeV	1.4	+0.5 -0.4	+0.4 -0.4	+0.4 -0.2	$1.00^{+0.03}_{-0.03}$
$qq' \rightarrow Hqq'$, ≥ 2 -jets, $350 \leq m_{jj} < 700$ GeV, $p_T^H \geq 200$ GeV	0.12	+0.15 -0.12	+0.15 -0.12	+0.03 -0.03	$0.100^{+0.003}_{-0.003}$
$qq' \rightarrow Hqq'$, ≥ 2 -jets, $700 \leq m_{jj} < 1000$ GeV, $p_T^H \geq 200$ GeV	-0.009	+0.057 -0.041	+0.057 -0.041	+0.006 -0.008	$0.067^{+0.002}_{-0.002}$
$qq' \rightarrow Hqq'$, ≥ 2 -jets, $m_{jj} \geq 1000$ GeV, $p_T^H \geq 200$ GeV	0.28	+0.11 -0.09	+0.10 -0.09	+0.05 -0.04	$0.166^{+0.005}_{-0.005}$
$qq \rightarrow H\ell\nu$, $p_T^V < 150$ GeV	1.4	+0.6 -0.6	+0.6 -0.6	+0.1 -0.1	$0.79^{+0.02}_{-0.02}$
$qq \rightarrow H\ell\nu$, $p_T^V \geq 150$ GeV	0.20	+0.13 -0.11	+0.13 -0.11	+0.02 -0.01	$0.121^{+0.005}_{-0.005}$
$pp \rightarrow H\ell\ell/\nu\bar{\nu}$, $p_T^V < 150$ GeV	-0.29	+0.40 -0.07	+0.39 -0.07	+0.07 -0.00	$0.45^{+0.02}_{-0.02}$
$pp \rightarrow H\ell\ell/\nu\bar{\nu}$, $p_T^V \geq 150$ GeV	0.04	+0.10 -0.08	+0.10 -0.08	+0.02 -0.02	$0.09^{+0.01}_{-0.01}$
$t\bar{t}H$, $p_T^H < 60$ GeV	0.21	+0.21 -0.18	+0.21 -0.18	+0.03 -0.01	$0.27^{+0.04}_{-0.04}$
$t\bar{t}H$, $60 \leq p_T^H < 120$ GeV	0.32	+0.23 -0.20	+0.23 -0.20	+0.04 -0.02	$0.40^{+0.05}_{-0.05}$
$t\bar{t}H$, $120 \leq p_T^H < 200$ GeV	0.18	+0.18 -0.15	+0.17 -0.15	+0.04 -0.02	$0.29^{+0.04}_{-0.04}$
$t\bar{t}H$, $200 \leq p_T^H < 300$ GeV	0.14	+0.09 -0.07	+0.09 -0.07	+0.01 -0.01	$0.12^{+0.02}_{-0.02}$
$t\bar{t}H$, $p_T^H \geq 300$ GeV	0.06	+0.05 -0.04	+0.05 -0.04	+0.01 -0.01	$0.06^{+0.01}_{-0.01}$
tH	0.36	+0.76 -0.60	+0.72 -0.57	+0.24 -0.17	$0.19^{+0.01}_{-0.02}$

B Additional κ -framework interpretations

B.1 Parameterization of STXS cross-section parameters and the $H \rightarrow \gamma\gamma$ branching ratio

Table 14 presents the modifiers that are applied to the STXS cross-section parameters σ_i , the partial decay widths $\Gamma_{\gamma\gamma}$, Γ_{gg} and $\Gamma_{Z\gamma}$ of the $H \rightarrow \gamma\gamma$, $H \rightarrow gg$ and $H \rightarrow Z\gamma$ decays, respectively, and the total width Γ_H . The symbols Γ_{gg}^{SM} and $\Gamma_{Z\gamma}^{\text{SM}}$ denote the SM predictions for Γ_{gg} and $\Gamma_{Z\gamma}$ respectively. Modifiers for the $gg \rightarrow H$ and $H \rightarrow \gamma\gamma$ loop processes are given either in terms of the effective modifiers κ_g and κ_γ or a resolved parameterization in terms of the modifiers to tree-level Higgs boson couplings, as specified in the description of each model. The total width Γ_H is expressed as a function of the κ modifiers, assuming no contributions from Higgs boson decays other than the ones present in the SM, except in the model in Appendix B.3 in which an effective description in terms of the κ_H modifier is used instead.

Table 14: Parameterization of Higgs boson production cross-sections σ_i , the partial decay widths $\Gamma_{\gamma\gamma}$, Γ_{gg} and $\Gamma_{Z\gamma}$ of the $H \rightarrow \gamma\gamma$, $H \rightarrow gg$ and $H \rightarrow Z\gamma$ decays, respectively, and the total width Γ_H , normalized to their SM values, as functions of the coupling-strength modifiers κ . The coefficients for $\sigma(tHW)$ and $\sigma(tHqb)$ include acceptance effects that differ between analysis categories as described in the text. Other coefficients are derived following the methodology in Refs. [6, 164].

Production cross-section	Main interference	Effective modifier	Resolved modifier
$\sigma(\text{ggF})$	t - b	κ_g^2	$1.040 \kappa_t^2 + 0.002 \kappa_b^2 - 0.038 \kappa_t \kappa_b - 0.005 \kappa_t \kappa_c$
$\sigma(\text{VBF})$	-	-	$0.733 \kappa_W^2 + 0.267 \kappa_Z^2$
$\sigma(q\bar{q} \rightarrow ZH)$	-	-	κ_Z^2
$\sigma(gg \rightarrow ZH)$	t - Z	-	$2.456 \kappa_Z^2 + 0.456 \kappa_t^2 - 1.903 \kappa_Z \kappa_t$ $- 0.011 \kappa_Z \kappa_b + 0.003 \kappa_t \kappa_b$
$\sigma(WH)$	-	-	κ_W^2
$\sigma(t\bar{t}H)$	-	-	κ_t^2
$\sigma(tHW)$	t - W	-	$A \kappa_t^2 + B \kappa_W^2 + C \kappa_t \kappa_W$, category-dependent
$\sigma(tHqb)$	t - W	-	$A \kappa_t^2 + B \kappa_W^2 + C \kappa_t \kappa_W$, category-dependent
$\sigma(b\bar{b}H)$	-	-	κ_b^2
Partial and total decay widths			
$\Gamma_{\gamma\gamma}$	t - W	κ_γ^2	$1.589 \kappa_W^2 + 0.072 \kappa_t^2 - 0.674 \kappa_W \kappa_t + 0.009 \kappa_W \kappa_\tau$ $+ 0.008 \kappa_W \kappa_b - 0.002 \kappa_t \kappa_b - 0.002 \kappa_t \kappa_\tau$
Γ_{gg}	t - b	κ_g^2	$1.111 \kappa_t^2 + 0.012 \kappa_b^2 - 0.123 \kappa_t \kappa_b$
$\Gamma_{Z\gamma}$	t - W	-	$1.118 \kappa_W^2 + 0.004 \kappa_t^2 - 0.125 \kappa_W \kappa_t + 0.003 \kappa_W \kappa_b$
Γ_H	-	κ_H^2	$0.581 \kappa_b^2 + 0.215 \kappa_W^2 + 0.063 \kappa_\tau^2$ $+ 0.026 \kappa_Z^2 + 0.029 \kappa_c^2 + 0.0023 \kappa_\gamma^2$ $+ 0.0004 \kappa_s^2 + 0.00022 \kappa_\mu^2$ $+ 0.082 (\Gamma_{gg}/\Gamma_{gg}^{\text{SM}})$ $+ 0.0015 (\Gamma_{Z\gamma}/\Gamma_{Z\gamma}^{\text{SM}})$

B.2 Parameterization with universal coupling modifiers to weak gauge bosons and fermions

In this model, two universal coupling modifiers are considered: $\kappa_V = \kappa_W = \kappa_Z$ which modifies Higgs boson couplings to gauge bosons, and $\kappa_F = \kappa_t = \kappa_b = \kappa_c = \kappa_\tau = \kappa_\mu$, modifying couplings to fermions. The $gg \rightarrow H$, $H \rightarrow \gamma\gamma$ and $gg \rightarrow ZH$ loops are described using their resolved parameterizations as a function of κ_V and κ_F . The measurement in the plane of (κ_V, κ_F) is shown in Figure 23. Only the region $\kappa_F > 0$ is considered, since $\kappa_F < 0$ was excluded with a significance larger than 4σ in analyses of the

Run 1 data set [165]. The best-fit values in data are

$$\begin{aligned}\kappa_V &= 1.02^{+0.06}_{-0.05} \\ \kappa_F &= 1.00^{+0.16}_{-0.13}.\end{aligned}$$

A linear correlation coefficient of 77% between the parameters is observed.

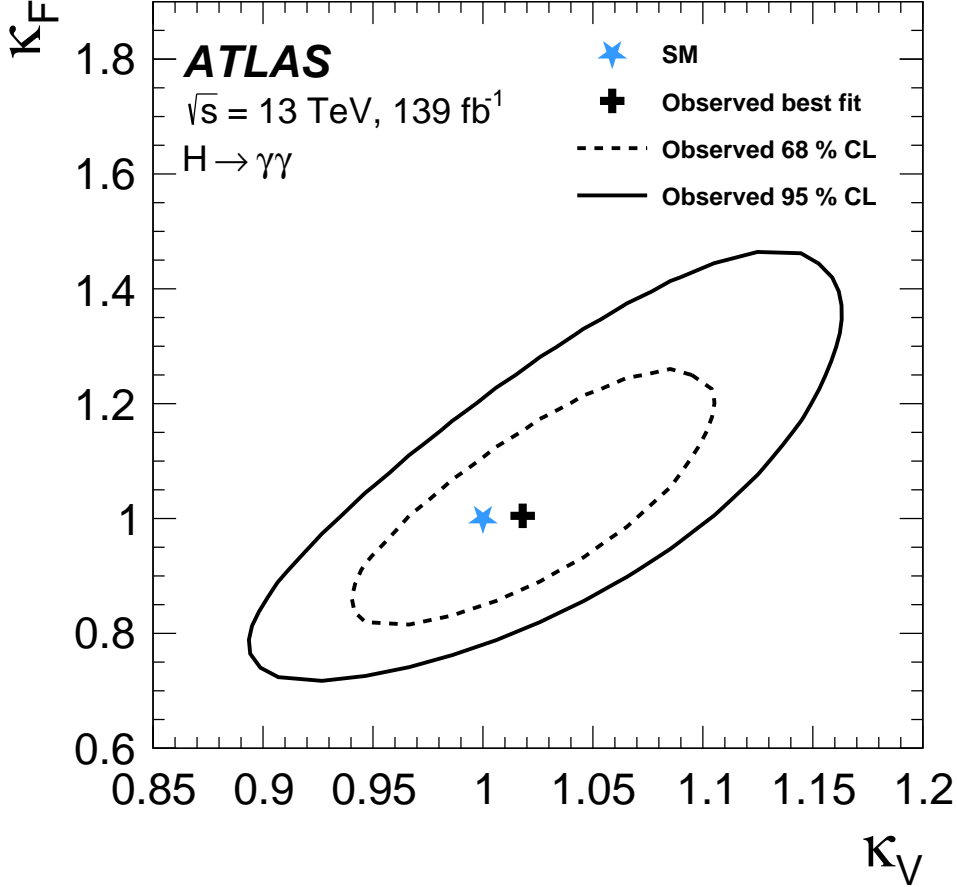


Figure 23: Negative log-likelihood contours at 68% CL (dashed line) and 95% CL (solid line) in the (κ_V, κ_F) plane of modifiers applied to Higgs boson couplings to gauge bosons (κ_V) and fermions (κ_F). Loop processes and the Higgs boson total width Γ_H are parameterized as a function of κ_V and κ_F . The best-fit point is indicated by a cross, and the SM prediction by a star.

B.3 Generic parameterization using ratios of coupling modifiers

In this model, the effective parameterization of the $gg \rightarrow H$ and $H \rightarrow \gamma\gamma$ processes is used, and a common coupling modifier $\kappa_V = \kappa_W = \kappa_Z$ is introduced for couplings to both W and Z bosons. The κ_τ parameter is fixed to 1 and $\kappa_b = \kappa_t$ is assumed. The total width of the Higgs boson is expressed using the effective parameterization $\Gamma_H = \kappa_H^2 \Gamma_H^{\text{SM}}$, where Γ_H^{SM} is the SM value of the width and κ_H is a coupling modifier.

The measurement parameters are

$$\begin{aligned}\kappa_{g\gamma} &= \kappa_g \kappa_\gamma / \kappa_H \\ \lambda_{Vg} &= \kappa_V / \kappa_g \\ \lambda_{tg} &= \kappa_t / \kappa_g,\end{aligned}$$

the first corresponding to the modifier for the $gg \rightarrow H \rightarrow \gamma\gamma$ process, which is taken as a reference, and the others two to ratios of coupling modifiers that can be measured without assumptions about the total width of the Higgs boson. The λ_{tg} parameter is allowed to take positive or negative values, while the other two parameters are positive by construction. Results are shown in Table 15. The negative log-likelihood scan of the λ_{tg} parameter is shown in Figure 24. Sensitivity to the sign of λ_{tg} is provided by the tH and $gg \rightarrow ZH$ processes, and leads to exclusion of the region $\lambda_{tg} < 0$ with a significance of 2.1σ .

Table 15: Best-fit values and uncertainties in the coupling-modifier ratio model. The second column expresses the measured parameters in terms of the coupling modifiers. The SM corresponds to $\kappa_{g\gamma} = \lambda_{tg} = \lambda_{Vg} = 1$.

Parameter	Definition in terms of κ modifiers	Result
$\kappa_{g\gamma}$	$\kappa_g \kappa_\gamma / \kappa_H$	1.02 ± 0.06
λ_{Vg}	κ_V / κ_g	1.01 ± 0.11
λ_{tg}	κ_t / κ_g	$0.95^{+0.15}_{-0.16}$

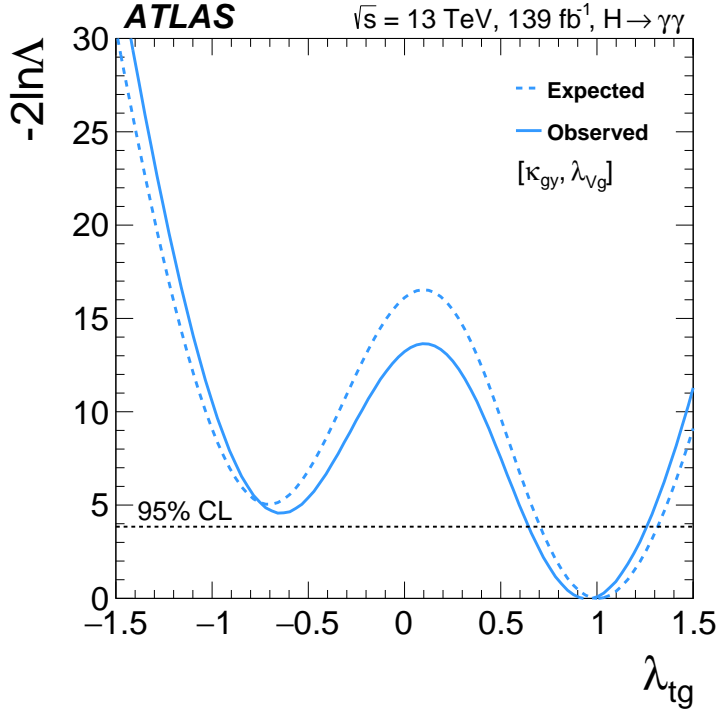


Figure 24: Negative log-likelihood scan as a function of $\lambda_{tg} = \kappa_t/\kappa_g$ in the coupling-modifier ratio model described in the text. The solid curve corresponds to observed data, and the dotted curve to an Asimov data set generated under the SM hypothesis.

C Effective field theory interpretation

C.1 Measurement of single SMEFT parameters

This appendix presents the complete results of the single-parameter SMEFT measurements described in Section 10.2, and illustrated in Figure 17. The SMEFT parameters corresponding to each operator in Table 11 are individually measured, in each case while fixing the other SMEFT parameters to 0 as in the SM. Confidence intervals at 68% and 95% CL are computed both in observed data and in an Asimov data set generated under the SM hypothesis. Results for the parameters c_k are reported in Table 16, except those where the confidence intervals extend beyond the region $|c_k| \leq 20$ where the SMEFT framework is considered valid.

Table 16: Measurement results for each SMEFT parameter individually, obtained from profile-likelihood scans in which other SMEFT parameters are fixed to 0. Confidence intervals at 68% and 95% CL are reported in data (observed) and in an Asimov dataset generated under the SM hypothesis (expected). Results in the linear and linear+quadratic SMEFT parameterizations are shown, for a scale $\Lambda = 1$ TeV. Confidence intervals for each parameter c_k are reported, except if they extend beyond the $|c_k| \leq 20$ region where the SMEFT framework is considered valid.

Parameter	Observed					Expected				
	linear			linear+quadratic		linear		linear+quadratic		
	Value	Uncertainty		Value	Uncertainty		Uncertainty		Uncertainty	
		68% CL	95% CL		68% CL	95% CL	68% CL	95% CL	68% CL	95% CL
c_{HW}	-0.0035	+0.0071 -0.0077	+0.014 -0.016	-0.0034	+0.0071 -0.0073	+0.014 -0.014	+0.0070 -0.0075	+0.013 -0.015	+0.0072 -0.0072	+0.014 -0.014
c_{HB}	-0.0011	+0.0023 -0.0025	+0.0044 -0.0050	-0.0011	+0.0023 -0.0023	+0.0046 -0.0046	+0.0022 -0.0024	+0.0043 -0.0049	+0.0023 -0.0023	+0.0046 -0.0046
c_{HWB}	0.0020	+0.0044 -0.0042	+0.0090 -0.0079	0.0019	+0.0042 -0.0041	+0.0083 -0.0081	+0.0043 -0.0041	+0.0088 -0.0077	+0.0042 -0.0042	+0.0083 -0.0082
c_{HG}	0.0011	+0.0030 -0.0028	+0.0062 -0.0053	0.0011	+0.0029 -0.0028	+0.0059 -0.0055	+0.0030 -0.0027	+0.0061 -0.0052	+0.0029 -0.0028	+0.0059 -0.0054
c_W	-0.047	+0.098 -0.11	+0.19 -0.21	-0.047	+0.098 -0.11	+0.19 -0.21	+0.096 -0.10	+0.18 -0.21	+0.096 -0.10	+0.18 -0.21
c_G	0.32	+1.5 -1.2	+3.4 -2.0	0.077	+0.13 -0.30	+0.22 -0.40	+1.5 -1.1	+3.4 -1.9	+0.18 -0.20	+0.28 -0.30
c_{uW}	-0.039	+0.080 -0.087	+0.15 -0.18	-0.039	+0.080 -0.087	+0.15 -0.18	+0.079 -0.083	+0.15 -0.17	+0.079 -0.083	+0.15 -0.17
c_{uB}	-0.021	+0.043 -0.046	+0.082 -0.094	-0.021	+0.043 -0.046	+0.082 -0.094	+0.042 -0.045	+0.080 -0.092	+0.042 -0.045	+0.080 -0.092
c_{uG}	0.030	+0.078 -0.078	+0.16 -0.14	0.030	+0.077 -0.078	+0.16 -0.15	+0.079 -0.074	+0.16 -0.14	+0.078 -0.075	+0.16 -0.14
c_{uH}	-0.29	+1.4 -1.5	+2.7 -3.0	-0.30	+1.4 -1.6	+2.6 -3.3	+1.4 -1.5	+2.7 -3.0	+1.4 -1.5	+2.5 -3.3
c_{dH}	0.63	+1.4 -1.3	+2.9 -2.5	0.61	+1.3 -1.3	+2.5 -2.7	+1.4 -1.3	+2.8 -2.4	+1.3 -1.4	+2.5 -2.7
c_{eH}	5.8	+13 -12	-	1.9	+5.6 -5.7	+8.9 -8.9	+13 -12	-	+9.1 -5.2	+12 -8.4
$c_{Hq}^{(3)}$	-0.027	+0.091 -0.081	+0.19 -0.15	-0.037	+0.096 -0.21	+0.17 -0.34	+0.10 -0.089	+0.20 -0.17	+0.085 -0.12	+0.16 -0.29
$c_{Hq}^{(1)}$	1.9	+1.7 -2.0	+3.1 -4.1	0.029	+0.20 -0.22	+0.35 -0.37	+2.0 -2.3	+3.6 -4.8	+0.30 -0.28	+0.44 -0.41
$c_{Hl}^{(3)}$	-0.15	+0.28 -0.28	+0.52 -0.58	-0.15	+0.28 -0.28	+0.52 -0.58	+0.26 -0.28	+0.50 -0.57	+0.26 -0.28	+0.50 -0.57
$c_{Hl}^{(1)}$	-	-	-	4.4	+6.8 -6.9	+12 -12	+13 -15	+16 -7.8	+16 -7.8	-
c_{Hu}	-0.97	+0.79 -0.67	+1.7 -1.2	-0.14	+0.30 -0.24	+0.51 -0.41	+0.96 -0.82	+2.0 -1.5	+0.32 -0.43	+0.49 -0.61
c_{Hd}	3.4	+2.2 -2.6	+4.0 -5.4	0.070	+0.33 -0.36	+0.55 -0.60	+2.7 -3.1	+4.9 -6.5	+0.51 -0.44	+0.73 -0.67
$c_{H\Box}$	0.68	+1.5 -1.4	+3.1 -2.7	0.63	+1.4 -1.4	+2.7 -2.7	+1.5 -1.4	+3.0 -2.6	+1.4 -1.4	+2.8 -2.9
c_{HD}	-0.21	+0.42 -0.44	+0.79 -0.91	-0.21	+0.42 -0.45	+0.79 -0.93	+0.41 -0.43	+0.77 -0.88	+0.40 -0.43	+0.76 -0.89
$c_{qq}^{(3)}$	0.72	+3.4 -2.8	+7.3 -5.0	-0.20	+0.55 -0.18	+0.69 -0.32	+3.2 -2.6	+6.8 -4.7	+0.29 -0.31	+0.43 -0.46
$c_{qq}^{(3) \prime}$	0.042	+0.37 -0.28	+0.83 -0.50	-0.30	+0.52 -0.19	+0.67 -0.34	+0.38 -0.29	+0.84 -0.49	+0.21 -0.44	+0.36 -0.60
$c_{qq}^{(1)}$	2.0	+14 -11	-	-0.20	+0.69 -0.30	+0.90 -0.52	+14 -11	+0.44 -	+0.44 -0.45	+0.67 -0.68
$c_{qq}^{(1) \prime}$	0.097	+0.79 -0.60	+1.7 -1.0	-0.50	+0.92 -0.31	+1.2 -0.57	+0.79 -0.61	+1.8 -1.0	+0.39 -0.73	+0.66 -1.0
c_{ll}^{\prime}	0.30	+0.53 -0.56	+1.1 -1.0	0.30	+0.52 -0.56	+1.1 -1.0	+0.55 -0.51	+1.1 -0.98	+0.54 -0.51	+1.1 -0.99
c_{uu}	1.4	+13 -9.9	-	-0.25	+0.85 -0.37	+1.1 -0.64	+13 -9.9	+0.53 -0.56	+0.81 -0.56	+0.81 -0.84
c_{uu}^{\prime}	0.098	+0.80 -0.61	+1.8 -1.1	-0.50	+0.92 -0.31	+1.2 -0.57	+0.81 -0.61	+1.8 -1.1	+0.39 -0.72	+0.66 -1.0
$c_{qu}^{(1)}$	-	-	-	-0.30	+1.1 -0.48	+1.4 -0.81	-	+0.68 -0.70	+1.0 -1.0	+1.0 -1.0
$c_{qu}^{(8)}$	0.15	+1.3 -0.97	+2.8 -1.7	-1.8	+2.6 -0.82	+3.3 -1.5	+1.3 -0.97	+2.8 -1.7	+0.84 -2.3	+1.5 -3.0
$c_{qd}^{(1)}$	-	-	-	0.75	+0.94 -2.4	+1.7 -3.2	-	+1.5 -1.5	+2.3 -2.3	+2.3 -2.3
$c_{qd}^{(8)}$	0.53	+5.5 -4.3	+12 -7.5	-2.3	+4.8 -2.3	+6.4 -3.9	+5.6 -4.3	+12 -7.5	+2.4 -4.1	+4.0 -5.8
$c_{ud}^{(1)}$	-	-	-	0.75	+0.93 -2.4	+1.7 -3.1	-	+1.5 -1.5	+2.3 -2.3	+2.3 -2.3
$c_{ud}^{(8)}$	0.53	+5.5 -4.3	+12 -7.5	-2.5	+5.1 -2.0	+6.7 -3.6	+5.6 -4.4	+12 -7.6	+2.4 -4.1	+4.0 -5.7

C.2 Simultaneous measurement of SMEFT parameters

This appendix presents the complete results of the simultaneous measurement of SMEFT parameters described in Section 10.3, shown in part in Table 12 and illustrated in Figure 19. The measurement parameters EV_n are shown in Table 17. Confidence intervals at 68% and 95% CL for the EV_n parameters defined in Table 17 are computed both in observed data and in an Asimov data set generated under the SM hypothesis. Results for the linear SMEFT parameterization are shown in Table 18 and for the linear+quadratic parameterization in Table 19.

Table 17: Measurement directions corresponding to the 12 largest eigenvalues of the Fisher information matrix of the SMEFT interpretation of the STXS measurement, shown as a decomposition in terms of Wilson coefficients in the Warsaw basis. The information matrix is obtained from the covariance matrix C_{STXS}^{-1} of the STXS measurement, computed using an Asimov data set generated in the SM hypothesis, propagated to the SMEFT measurement using the linear parameterization. Each linear combination is normalized to unit Euclidean norm. Only Wilson coefficients with a coefficient larger than 0.01 are shown.

Eigenvalue	Eigenvector
350000	$-0.53c_{HG} - 0.02c_{uG} + 0.23c_{HW} + 0.71c_{HB} - 0.4c_{HWB} + 0.02c_W + 0.02c_{uW} + 0.04c_{uB}$
34000	$-0.85c_{HG} - 0.02c_{uG} - 0.14c_{HW} - 0.44c_{HB} + 0.25c_{HWB} - 0.01c_W - 0.01c_{uW} - 0.02c_{uB} + 0.01c_{Hq}^{(3)}$
110	$-0.01c_{HG} + 0.05c_{uG} - 0.17c_{HW} + 0.03c_{HB} - 0.04c_{HWB} - 0.01c_{Hl}^{(3)} - 0.98c_{Hq}^{(3)} - 0.07c_{Hu} + 0.02c_{Hd} + 0.03c_{Hq}^{(1)} + 0.01c_{qq}^{(1)'} + 0.03c_{qq}^{(3)'} + 0.01c'_{uu}$
20	$-0.01c_{HG} + 0.68c_{uG} - 0.06c_{uH} - 0.08c_{HW} + 0.01c_{HB} - 0.04c_{HWB} + 0.13c_{Hl}^{(3)} - 0.07c'_{ll} - 0.01c_{HD} + 0.08c_{Hq}^{(3)} + 0.14c_G + 0.01c_{qq}^{(1)} + 0.27c_{qq}^{(1)'} + 0.06c_{qq}^{(3)} + 0.56c_{qq}^{(3)'} + 0.02c_{uu} + 0.26c'_{uu} + 0.04c_{ud}^{(8)} + 0.17c_{qu}^{(8)} + 0.04c_{qd}^{(8)}$
2.9	$-0.02c_{HG} + 0.64c_{uG} - 0.09c_{uH} - 0.24c_{HW} + 0.04c_{HB} - 0.06c_{HWB} + 0.15c_{Hl}^{(3)} - 0.09c'_{ll} - 0.01c_{HD} + 0.05c_{Hq}^{(3)} + 0.02c_{Hu} - 0.02c_{Hq}^{(1)} - 0.19c_G - 0.02c_{qq}^{(1)} - 0.28c_{qq}^{(1)'} - 0.04c_{qq}^{(3)} - 0.52c_{qq}^{(3)'} - 0.01c_{uu} - 0.27c'_{uu} - 0.03c_{ud}^{(8)} - 0.16c_{qu}^{(8)} - 0.03c_{qd}^{(8)}$
1.8	$-0.24c_{uG} + 0.01c_{uH} - 0.9c_{HW} + 0.21c_{HB} - 0.14c_{HWB} + 0.01c_{uB} - 0.11c_{Hl}^{(3)} + 0.01c_{HD} + 0.15c_{Hq}^{(3)} + 0.1c_{Hu} - 0.03c_{Hd} - 0.08c_{Hq}^{(1)} + 0.03c_G + 0.05c_{qq}^{(1)'} + 0.08c_{qq}^{(3)'} + 0.05c'_{uu} + 0.03c_{qu}^{(8)}$
0.89	$+0.03c_{uG} + 0.03c_{uH} + 0.09c_{HW} + 0.15c_{HB} + 0.32c_{HWB} + 0.02c_{Hl}^{(3)} + 0.01c'_{ll} + 0.05c_{HD} - 0.1c_{Hq}^{(3)} + 0.83c_{Hu} - 0.25c_{Hd} - 0.31c_{Hq}^{(1)} - 0.04c_{He} - 0.05c_{Hl}^{(1)}$
0.075	$+0.27c_{uG} + 0.38c_{uH} + 0.02c_{HW} + 0.06c_{HB} + 0.1c_{HWB} + 0.02c_{uW} - 0.78c_{Hl}^{(3)} + 0.37c'_{ll} + 0.07c_{HD} + 0.01c_{Hq}^{(3)} - 0.04c_{Hu} + 0.09c_{Hq}^{(1)} + 0.09c_G - 0.03c_{qq}^{(1)'} - 0.06c_{qq}^{(3)} - 0.04c_{qq}^{(3)'} - 0.03c'_{uu} - 0.02c_{qu}^{(8)}$
0.038	$+0.01c_{uG} + 0.03c_{uH} + 0.09c_{HW} - 0.38c_{HB} - 0.65c_{HWB} - 0.08c_{uW} - 0.17c_{Hl}^{(3)} + 0.03c'_{ll} - 0.08c_{HD} - 0.02c_{Hq}^{(3)} + 0.13c_{Hu} + 0.04c_{Hd} - 0.56c_{Hq}^{(1)} + 0.09c_{He} + 0.12c_{Hl}^{(1)} + 0.02c_G + 0.18c_{qq}^{(3)} - 0.02c_{qq}^{(3)'}$
0.027	$+0.06c_{uH} + 0.02c_{HW} - 0.09c_{HB} - 0.13c_{HWB} + 0.37c_{uW} + 0.05c_{Hl}^{(3)} - 0.02c'_{ll} + 0.02c_{Hd} - 0.14c_{Hq}^{(1)} + 0.02c_{He} + 0.03c_{Hl}^{(1)} - 0.05c_G + 0.04c_{qq}^{(1)'} - 0.89c_{qq}^{(3)} + 0.06c_{qq}^{(3)'} + 0.03c'_{uu} + 0.02c_{qu}^{(8)}$
0.011	$+0.04c_{uH} - 0.03c_{HB} - 0.05c_{HWB} - 0.02c_{uW} - 0.1c_{Hl}^{(3)} + 0.03c'_{ll} + 0.06c_{Hu} - 0.05c_{Hd} + 0.11c_{Hq}^{(1)} + 0.01c_{He} + 0.02c_{Hl}^{(1)} - 0.95c_G + 0.15c_{qq}^{(1)'} + 0.05c_{qq}^{(3)} + 0.11c_{qq}^{(3)'} + 0.13c'_{uu} - 0.01c_{qu}^{(1)} + 0.09c_{qu}^{(8)}$
0.0067	$-0.01c_{uG} - 0.15c_{uH} + 0.01c_{HW} - 0.2c_{HB} - 0.36c_{HWB} + 0.02c_{uW} - 0.13c_{Hl}^{(3)} - 0.16c'_{ll} - 0.06c_{HD} + 0.37c_{Hu} - 0.3c_{Hd} + 0.69c_{Hq}^{(1)} + 0.1c_{He} + 0.14c_{Hl}^{(1)} + 0.14c_G - 0.02c_{qq}^{(1)'} - 0.05c_{qq}^{(3)} - 0.01c_{qq}^{(3)'} - 0.02c'_{uu} - 0.01c_{qu}^{(8)}$

Table 18: Measured values of the EV_n parameters in data (observed) and in an Asimov data set generated under the SM hypothesis (expected). The linear SMEFT parameterization is used. Numbers in bold script indicate that the uncertainty band is truncated at the value for which the model pdf becomes negative.

Model parameter	Observed		Expected		
	Value	Uncertainty		Uncertainty	
		68% CL	95% CL	68% CL	95% CL
EV1	-0.0008	+0.0017 -0.0018	+0.0032 -0.0037	+0.0016 -0.0018	+0.0031 -0.0036
EV2	0.000	± 0.006	+0.012 -0.010	+0.006 -0.005	+0.011 -0.010
EV3	0.04	± 0.10	+0.18 -0.21	+0.09 -0.10	+0.18 -0.20
EV4	-0.04	+0.25 -0.22	+0.5 -0.4	+0.24 -0.21	+0.5 -0.4
EV5	-0.2	± 0.6	+1.2 -1.3	± 0.6	+1.1 -1.3
EV6	0.2	± 0.8	+1.7 -1.6	+0.8 -0.7	± 1.5
EV7	-1.7	± 1.0	+2.0 -1.3	+1.1 -1.0	+2.2 -2.1
EV8	-0.7	+3.5 -3.2	+7 -6	+3.9 -3.4	+8 -7
EV9	7.5	+2.5 -5.2	+2.5 -11	+5 -5	+10 -11
EV10	0	+7 -9	+8 -19	+5 -7	+9 -16
EV11	-6	+9 -10	+18 -19	± 10	± 19
EV12	3	+12 -13	+12 -25	± 12	± 24

Table 19: Measured values of the EV_n parameters in data (observed) and in an Asimov data set generated under the SM hypothesis (expected). The linear+quadratic SMEFT parameterization is used.

Model parameter	Observed		Expected		
	Value	Uncertainty		Uncertainty	
		68% CL	95% CL	68% CL	95% CL
EV1	0.004	+0.007 -0.010	+0.014 -0.049	+0.14 -0.01	+0.20 -0.03
EV2	-0.006	+0.008 -0.009	+0.017 -0.030	+0.006 -0.095	+0.014 -0.16
EV3	0.04	+0.11 -0.08	+0.37 -0.21	+0.14 -0.11	+0.40 -0.27
EV4	-0.08	+0.29 -0.35	+0.5 -1.2	+0.23 -0.48	+0.5 -1.1
EV5	0.29	+0.30 -0.69	+0.7 -2.2	+0.5 -0.6	+0.9 -1.7
EV6	0.0	+0.8 -0.5	+1.7 -1.0	+0.9 -0.7	+2.2 -1.2
EV7	-0.9	+1.2 -0.5	+1.4 -1.5	+0.7 -1.7	+1.2 -3.3
EV8	-1.2	+2.5 -1.0	+10 -1.8	+3.1 -1.7	+9.0 -2.4
EV9	1.7	+1.4 -1.6	+4.8 -3.3	+3.9 -1.8	+8.4 -2.9
EV10	0.4	+0.5 -0.6	± 1.2	+0.9 -0.5	+1.8 -0.8
EV11	0.05	+0.47 -0.21	+1.6 -0.5	+0.7 -0.4	+1.8 -0.6
EV12	1.2	+0.8 -1.0	+2.3 -2.1	+2.4 -1.1	+4.8 -1.8

C.3 Results including SMEFT propagator corrections

This appendix presents results similar to those in Section 10, but with SMEFT corrections applied to the mass and width parameters of off-shell SM particles, as implemented in the SMEFT_{SIM} generator [28]. These corrections are applied to the propagators of the W and Z boson, the Higgs boson and the top quark in each process, at first order in the SMEFT. These corrections are only available for the linear SMEFT parameterization.

Table 20 shows the observed results with the propagator corrections included, for comparison with the ones in Table 18. The EV_n parameters are defined in the same way as for the baseline linear parameterization. Differences from the baseline results are visible in the measurement of EV_3 , due to the impact of W and Z propagator corrections on the $q\bar{q}' \rightarrow VH$ processes. Small changes in the principal components of the measurements due to the propagator corrections also lead to changes in the uncertainties in other parameters, in particular EV_1 . This also leads to generally larger correlations between the measurements than in the baseline linear parameterization, as shown in Figure 25.

Table 20: Observed values of the EV_n parameters in data together with their 68% CL and 95% CL intervals in data for the linear SMEFT parameterization including corrections to the W , Z , Higgs boson and top quark propagators as described in the text. Numbers in bold script indicate that the uncertainty band is truncated at the value for which the probability distribution function of the fit becomes negative.

Model parameter	Value	Uncertainty	
		68% CL	95% CL
EV1	0.0001	+0.0031 -0.0038	+0.006 -0.007
EV2	0.000	± 0.006	+0.012 -0.010
EV3	0.05	± 0.12	+0.22 -0.26
EV4	-0.03	+0.25 -0.23	+0.5 -0.4
EV5	-0.2	± 0.6	+1.2 -1.3
EV6	0.2	± 0.8	+1.7 -1.6
EV7	-2.0	+1.1 -0.9	+2.2 -0.9
EV8	-0.5	+3.4 -3.2	+7 -6
EV9	8.2	+2.5 -5.8	+2.5 -12
EV10	1	+7 -9	+8 -19
EV11	-5	+9 -10	+18 -19
EV12	4	+12 -13	+13 -25

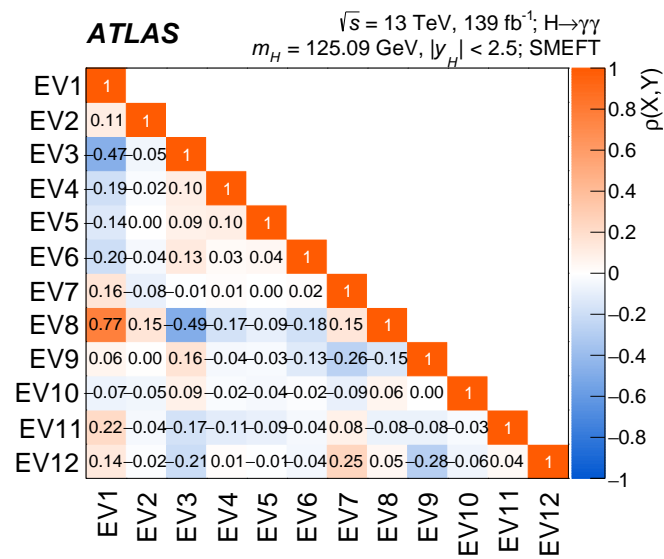


Figure 25: Observed linear correlation coefficients of the EV_n parameters in the linear SMEFT parameterization including corrections to W , Z , Higgs boson and top quark propagators.

References

- [1] ATLAS Collaboration, *Observation of a new particle in the search for the Standard Model Higgs boson with the ATLAS detector at the LHC*, *Phys. Lett. B* **716** (2012) 1, arXiv: [1207.7214 \[hep-ex\]](#).
- [2] CMS Collaboration, *Observation of a new boson at a mass of 125 GeV with the CMS experiment at the LHC*, *Phys. Lett. B* **716** (2012) 30, arXiv: [1207.7235 \[hep-ex\]](#).
- [3] F. Englert and R. Brout, *Broken Symmetry and the Mass of Gauge Vector Mesons*, *Phys. Rev. Lett.* **13** (1964) 321.
- [4] P. W. Higgs, *Broken Symmetries and the Masses of Gauge Bosons*, *Phys. Rev. Lett.* **13** (1964) 508.
- [5] G. Guralnik, C. Hagen and T. Kibble, *Global Conservation Laws and Massless Particles*, *Phys. Rev. Lett.* **13** (1964) 585.
- [6] LHC Higgs Cross Section Working Group (D. de Florian et al.), *Handbook of LHC Higgs Cross Sections: 4. Deciphering the Nature of the Higgs Sector*, 2016, arXiv: [1610.07922 \[hep-ph\]](#).
- [7] ATLAS Collaboration, *Measurement of Higgs boson production in the diphoton decay channel in pp collisions at center-of-mass energies of 7 and 8 TeV with the ATLAS detector*, *Phys. Rev. D* **90** (2014) 112015, arXiv: [1408.7084 \[hep-ex\]](#).
- [8] ATLAS Collaboration, *Measurements of fiducial and differential cross sections for Higgs boson production in the diphoton decay channel at $\sqrt{s} = 8$ TeV with ATLAS*, *JHEP* **09** (2014) 112, arXiv: [1407.4222 \[hep-ex\]](#).
- [9] ATLAS Collaboration, *Measurement of the Higgs boson mass from the $H \rightarrow \gamma\gamma$ and $H \rightarrow ZZ^* \rightarrow 4\ell$ channels in pp collisions at center-of-mass energies of 7 and 8 TeV with the ATLAS detector*, *Phys. Rev. D* **90** (2014) 052004, arXiv: [1406.3827 \[hep-ex\]](#).
- [10] ATLAS Collaboration, *Measurements of Higgs boson properties in the diphoton decay channel with 36fb^{-1} of pp collision data at $\sqrt{s} = 13$ TeV with the ATLAS detector*, *Phys. Rev. D* **98** (2018) 052005, arXiv: [1802.04146 \[hep-ex\]](#).
- [11] ATLAS Collaboration, *Measurement of the Higgs boson mass in the $H \rightarrow ZZ^* \rightarrow 4\ell$ and $H \rightarrow \gamma\gamma$ channels with $\sqrt{s} = 13$ TeV pp collisions using the ATLAS detector*, *Phys. Lett. B* **784** (2018) 345, arXiv: [1806.00242 \[hep-ex\]](#).
- [12] ATLAS Collaboration, *Study of the spin and parity of the Higgs boson in diboson decays with the ATLAS detector*, *Eur. Phys. J. C* **75** (2015) 476, arXiv: [1506.05669 \[hep-ex\]](#), Erratum: *Eur. Phys. J. C* **76** (2016) 152.
- [13] ATLAS Collaboration, *Combined measurements of Higgs boson production and decay using up to 80fb^{-1} of proton–proton collision data at $\sqrt{s} = 13$ TeV collected with the ATLAS experiment*, *Phys. Rev. D* **101** (2020) 012002, arXiv: [1909.02845 \[hep-ex\]](#).
- [14] ATLAS Collaboration, *Study of the CP properties of the interaction of the Higgs boson with top quarks using top quark associated production of the Higgs boson and its decay into two photons with the ATLAS detector at the LHC*, *Phys. Rev. Lett.* **125** (2020) 061802, arXiv: [2004.04545 \[hep-ex\]](#).

- [15] CMS Collaboration, *A measurement of the Higgs boson mass in the diphoton decay channel*, *Phys. Lett. B* **805** (2020) 135425, arXiv: [2002.06398 \[hep-ex\]](#).
- [16] CMS Collaboration, *Combined measurements of Higgs boson couplings in proton–proton collisions at $\sqrt{s} = 13$ TeV*, *Eur. Phys. J. C* **79** (2019) 421, arXiv: [1809.10733 \[hep-ex\]](#).
- [17] CMS Collaboration, *Measurement of inclusive and differential Higgs boson production cross sections in the diphoton decay channel in proton–proton collisions at $\sqrt{s} = 13$ TeV*, *JHEP* **01** (2019) 183, arXiv: [1807.03825 \[hep-ex\]](#).
- [18] CMS Collaboration, *Measurements of Higgs boson properties in the diphoton decay channel in proton–proton collisions at $\sqrt{s} = 13$ TeV*, *JHEP* **11** (2018) 185, arXiv: [1804.02716 \[hep-ex\]](#).
- [19] CMS Collaboration, *Measurements of $t\bar{t}H$ Production and the CP Structure of the Yukawa Interaction between the Higgs Boson and Top Quark in the Diphoton Decay Channel*, *Phys. Rev. Lett.* **125** (2020) 061801, arXiv: [2003.10866 \[hep-ex\]](#).
- [20] ATLAS Collaboration, *Luminosity determination in pp collisions at $\sqrt{s} = 13$ TeV using the ATLAS detector at the LHC*, ATLAS-CONF-2019-021, 2019, URL: <https://cds.cern.ch/record/2677054>.
- [21] G. Avoni et al., *The new LUCID-2 detector for luminosity measurement and monitoring in ATLAS*, *JINST* **13** (2018) P07017.
- [22] M. Frate, K. Cranmer, S. Kalia, A. Vandenberg-Rodes and D. Whiteson, *Modeling Smooth Backgrounds and Generic Localized Signals with Gaussian Processes*, (2017), arXiv: [1709.05681 \[physics.data-an\]](#).
- [23] J. Andersen et al., ‘Les Houches 2015: Physics at TeV Colliders Standard Model Working Group Report’, *9th Les Houches Workshop on Physics at TeV Colliders*, 2016, arXiv: [1605.04692 \[hep-ph\]](#).
- [24] N. Berger et al., *Simplified Template Cross Sections - Stage 1.1*, (2019), arXiv: [1906.02754 \[hep-ph\]](#).
- [25] S. Amoroso et al., ‘Les Houches 2019: Physics at TeV Colliders: Standard Model Working Group Report’, *11th Les Houches Workshop on Physics at TeV Colliders: PhysTeV Les Houches*, 2020, arXiv: [2003.01700 \[hep-ph\]](#).
- [26] W. Buchmüller and D. Wyler, *Effective lagrangian analysis of new interactions and flavour conservation*, *Nucl. Phys. B* **268** (1986) 621.
- [27] B. Grzadkowski, M. Iskrzynski, M. Misiak and J. Rosiek, *Dimension-six terms in the Standard Model Lagrangian*, *JHEP* **10** (2010) 085, arXiv: [1008.4884 \[hep-ph\]](#).
- [28] I. Brivio, *SMEFTsim 3.0 — a practical guide*, *JHEP* **04** (2021) 073, arXiv: [2012.11343 \[hep-ph\]](#).
- [29] ATLAS Collaboration, *The ATLAS Experiment at the CERN Large Hadron Collider*, *JINST* **3** (2008) S08003.

- [30] ATLAS Collaboration, *ATLAS Insertable B-Layer Technical Design Report*, ATLAS-TDR-19, 2010, URL: <https://cds.cern.ch/record/1291633>,
ATLAS Insertable B-Layer Technical Design Report Addendum, ATLAS-TDR-19-ADD-1, 2012, URL: <https://cds.cern.ch/record/1451888>.
- [31] B. Abbott et al., *Production and integration of the ATLAS Insertable B-Layer*, *JINST* **13** (2018) T05008, arXiv: [1803.00844](https://arxiv.org/abs/1803.00844) [[physics.ins-det](#)].
- [32] ATLAS Collaboration, *Performance of the ATLAS trigger system in 2015*, *Eur. Phys. J. C* **77** (2017) 317, arXiv: [1611.09661](https://arxiv.org/abs/1611.09661) [[hep-ex](#)].
- [33] ATLAS Collaboration, *The ATLAS Collaboration Software and Firmware*, ATL-SOFT-PUB-2021-001, 2021, URL: <https://cds.cern.ch/record/2767187>.
- [34] ATLAS Collaboration, *ATLAS data quality operations and performance for 2015–2018 data-taking*, *JINST* **15** (2020) P04003, arXiv: [1911.04632](https://arxiv.org/abs/1911.04632) [[physics.ins-det](#)].
- [35] ATLAS Collaboration, *Performance of electron and photon triggers in ATLAS during LHC Run 2*, *Eur. Phys. J. C* **80** (2020) 47, arXiv: [1909.00761](https://arxiv.org/abs/1909.00761) [[hep-ex](#)].
- [36] S. Alioli, P. Nason, C. Oleari and E. Re, *A general framework for implementing NLO calculations in shower Monte Carlo programs: the POWHEG BOX*, *JHEP* **06** (2010) 043, arXiv: [1002.2581](https://arxiv.org/abs/1002.2581) [[hep-ph](#)].
- [37] P. Nason, *A New method for combining NLO QCD with shower Monte Carlo algorithms*, *JHEP* **11** (2004) 040, arXiv: [hep-ph/0409146](https://arxiv.org/abs/hep-ph/0409146).
- [38] S. Frixione, P. Nason and C. Oleari, *Matching NLO QCD computations with parton shower simulations: the POWHEG method*, *JHEP* **11** (2007) 070, arXiv: [0709.2092](https://arxiv.org/abs/0709.2092) [[hep-ph](#)].
- [39] H. B. Hartanto, B. Jäger, L. Reina and D. Wackerroth, *Higgs boson production in association with top quarks in the POWHEG BOX*, *Phys. Rev. D* **91** (2015) 094003, arXiv: [1501.04498](https://arxiv.org/abs/1501.04498) [[hep-ph](#)].
- [40] K. Hamilton, P. Nason and G. Zanderighi, *MINLO: multi-scale improved NLO*, *JHEP* **10** (2012) 155, arXiv: [1206.3572](https://arxiv.org/abs/1206.3572) [[hep-ph](#)].
- [41] J. M. Campbell et al., *NLO Higgs boson production plus one and two jets using the POWHEG BOX, MadGraph4 and MCFM*, *JHEP* **07** (2012) 092, arXiv: [1202.5475](https://arxiv.org/abs/1202.5475) [[hep-ph](#)].
- [42] K. Hamilton, P. Nason, C. Oleari and G. Zanderighi, *Merging H/W/Z + 0 and 1 jet at NLO with no merging scale: a path to parton shower + NNLO matching*, *JHEP* **05** (2013) 082, arXiv: [1212.4504](https://arxiv.org/abs/1212.4504) [[hep-ph](#)].
- [43] S. Catani and M. Grazzini, *Next-to-Next-to-Leading-Order Subtraction Formalism in Hadron Collisions and its Application to Higgs-boson Production at the Large Hadron Collider*, *Phys. Rev. Lett.* **98** (2007) 222002, arXiv: [hep-ph/0703012](https://arxiv.org/abs/hep-ph/0703012) [[hep-ph](#)].
- [44] G. Bozzi, S. Catani, D. de Florian and M. Grazzini, *Transverse-momentum resummation and the spectrum of the Higgs boson at the LHC*, *Nucl. Phys. B* **737** (2006) 73, arXiv: [hep-ph/0508068](https://arxiv.org/abs/hep-ph/0508068) [[hep-ph](#)].
- [45] D. de Florian, G. Ferrera, M. Grazzini and D. Tommasini, *Transverse-momentum resummation: Higgs boson production at the Tevatron and the LHC*, *JHEP* **11** (2011) 064, arXiv: [1109.2109](https://arxiv.org/abs/1109.2109) [[hep-ph](#)].

- [46] J. Butterworth et al., *PDF4LHC recommendations for LHC Run II*, *J. Phys. G* **43** (2016) 023001, arXiv: [1510.03865 \[hep-ph\]](#).
- [47] J. Alwall et al., *The automated computation of tree-level and next-to-leading order differential cross sections, and their matching to parton shower simulations*, *JHEP* **07** (2014) 079, arXiv: [1405.0301 \[hep-ph\]](#).
- [48] P. Artoisenet, R. Frederix, O. Mattelaer and R. Rietkerk, *Automatic spin-entangled decays of heavy resonances in Monte Carlo simulations*, *JHEP* **03** (2013) 015, arXiv: [1212.3460 \[hep-ph\]](#).
- [49] S. Frixione, E. Laenen, P. Motylinski, C. White and B. R. Webber, *Single-top hadroproduction in association with a W boson*, *JHEP* **07** (2008) 029, arXiv: [0805.3067 \[hep-ph\]](#).
- [50] F. Demartin, B. Maier, F. Maltoni, K. Mawatari and M. Zaro, *tWH associated production at the LHC*, *Eur. Phys. J. C* **77** (2017) 34, arXiv: [1607.05862 \[hep-ph\]](#).
- [51] T. Sjöstrand, S. Mrenna and P. Z. Skands, *A brief introduction to PYTHIA 8.1*, *Comput. Phys. Commun.* **178** (2008) 852, arXiv: [0710.3820 \[hep-ph\]](#).
- [52] T. Sjöstrand et al., *An introduction to PYTHIA 8.2*, *Comput. Phys. Commun.* **191** (2015) 159, arXiv: [1410.3012 \[hep-ph\]](#).
- [53] ATLAS Collaboration, *Measurement of the Z/ γ^* boson transverse momentum distribution in pp collisions at $\sqrt{s} = 7$ TeV with the ATLAS detector*, *JHEP* **09** (2014) 145, arXiv: [1406.3660 \[hep-ex\]](#).
- [54] D. J. Lange, *The EvtGen particle decay simulation package*, *Nucl. Instrum. Meth. A* **462** (2001) 152.
- [55] J. Bellm et al., *Herwig 7.1 Release Note*, (2017), arXiv: [1705.06919 \[hep-ph\]](#).
- [56] J. Bellm et al., *Herwig 7.0/Herwig++ 3.0 release note*, *Eur. Phys. J. C* **76** (2016) 196, arXiv: [1512.01178 \[hep-ph\]](#).
- [57] R. Frederix and S. Frixione, *Merging meets matching in MC@NLO*, *JHEP* **12** (2012) 061, arXiv: [1209.6215 \[hep-ph\]](#).
- [58] ATLAS Collaboration, *ATLAS Pythia 8 tunes to 7 TeV data*, ATL-PHYS-PUB-2014-021, 2014, URL: <https://cds.cern.ch/record/1966419>.
- [59] J. R. Andersen et al., *Handbook of LHC Higgs Cross Sections: 3. Higgs Properties*, (2013), ed. by S. Heinemeyer, C. Mariotti, G. Passarino and R. Tanaka, arXiv: [1307.1347 \[hep-ph\]](#).
- [60] ATLAS and CMS Collaborations, *Combined Measurement of the Higgs Boson Mass in pp Collisions at $\sqrt{s} = 7$ and 8 TeV with the ATLAS and CMS Experiments*, *Phys. Rev. Lett.* **114** (2015) 191803, arXiv: [1503.07589 \[hep-ex\]](#).
- [61] C. Anastasiou et al., *High precision determination of the gluon fusion Higgs boson cross-section at the LHC*, *JHEP* **05** (2016) 058, arXiv: [1602.00695 \[hep-ph\]](#).
- [62] C. Anastasiou, C. Duhr, F. Dulat, F. Herzog and B. Mistlberger, *Higgs Boson Gluon-Fusion Production in QCD at Three Loops*, *Phys. Rev. Lett.* **114** (2015) 212001, arXiv: [1503.06056 \[hep-ph\]](#).

- [63] F. Dulat, A. Lazopoulos and B. Mistlberger, *iHixs 2 – Inclusive Higgs cross sections*, *Comput. Phys. Commun.* **233** (2018) 243, arXiv: [1802.00827 \[hep-ph\]](#).
- [64] R. V. Harlander and K. J. Ozeren, *Finite top mass effects for hadronic Higgs production at next-to-next-to-leading order*, *JHEP* **11** (2009) 088, arXiv: [0909.3420 \[hep-ph\]](#).
- [65] R. V. Harlander and K. J. Ozeren, *Top mass effects in Higgs production at next-to-next-to-leading order QCD: Virtual corrections*, *Phys. Lett. B* **679** (2009) 467, arXiv: [0907.2997 \[hep-ph\]](#).
- [66] R. V. Harlander, H. Mantler, S. Marzani and K. J. Ozeren, *Higgs production in gluon fusion at next-to-next-to-leading order QCD for finite top mass*, *Eur. Phys. J. C* **66** (2010) 359, arXiv: [0912.2104 \[hep-ph\]](#).
- [67] A. Pak, M. Rogal and M. Steinhauser, *Finite top quark mass effects in NNLO Higgs boson production at LHC*, *JHEP* **02** (2010) 025, arXiv: [0911.4662 \[hep-ph\]](#).
- [68] S. Actis, G. Passarino, C. Sturm and S. Uccirati, *NLO electroweak corrections to Higgs boson production at hadron colliders*, *Phys. Lett. B* **670** (2008) 12, arXiv: [0809.1301 \[hep-ph\]](#).
- [69] S. Actis, G. Passarino, C. Sturm and S. Uccirati, *NNLO computational techniques: The cases $H \rightarrow \gamma\gamma$ and $H \rightarrow gg$* , *Nucl. Phys. B* **811** (2009) 182, arXiv: [0809.3667 \[hep-ph\]](#).
- [70] M. Bonetti, K. Melnikov and L. Tancredi, *Higher order corrections to mixed QCD-EW contributions to Higgs boson production in gluon fusion*, *Phys. Rev. D* **97** (2018) 056017, arXiv: [1801.10403 \[hep-ph\]](#), Erratum: *Phys. Rev. D* **97** (2018) 099906.
- [71] U. Aglietti, R. Bonciani, G. Degrossi and A. Vicini, *Two-loop light fermion contribution to Higgs production and decays*, *Phys. Lett. B* **595** (2004) 432, arXiv: [hep-ph/0404071](#).
- [72] ATLAS Collaboration, *Measurement of the Higgs boson coupling properties in the $H \rightarrow ZZ^* \rightarrow 4\ell$ decay channel at $\sqrt{s} = 13$ TeV with the ATLAS detector*, *JHEP* **03** (2018) 095, arXiv: [1712.02304 \[hep-ex\]](#).
- [73] E. Bagnaschi, G. Degrossi, P. Slavich and A. Vicini, *Higgs production via gluon fusion in the POWHEG approach in the SM and in the MSSM*, *JHEP* **02** (2012) 088, arXiv: [1111.2854 \[hep-ph\]](#).
- [74] K. Hamilton, P. Nason and G. Zanderighi, *Finite quark-mass effects in the NNLOPS POWHEG+MiNLO Higgs generator*, *JHEP* **05** (2015) 140, arXiv: [1501.04637 \[hep-ph\]](#).
- [75] M. Ciccolini, A. Denner and S. Dittmaier, *Strong and electroweak corrections to the production of Higgs + 2 jets via weak interactions at the LHC*, *Phys. Rev. Lett.* **99** (2007) 161803, arXiv: [0707.0381 \[hep-ph\]](#).
- [76] M. Ciccolini, A. Denner and S. Dittmaier, *Electroweak and QCD corrections to Higgs production via vector-boson fusion at the LHC*, *Phys. Rev. D* **77** (2008) 013002, arXiv: [0710.4749 \[hep-ph\]](#).

- [77] P. Bolzoni, F. Maltoni, S.-O. Moch and M. Zaro, *Higgs Boson Production via Vector-Boson Fusion at Next-to-Next-to-Leading Order in QCD*, *Phys. Rev. Lett.* **105** (2010) 011801, arXiv: [1003.4451 \[hep-ph\]](#).
- [78] O. Brein, R. V. Harlander and T. J. E. Zirke, *vh@nnlo – Higgs Strahlung at hadron colliders*, *Comput. Phys. Commun.* **184** (2013) 998, arXiv: [1210.5347 \[hep-ph\]](#).
- [79] R. V. Harlander, J. Klappert, S. Liebler and L. Simon, *vh@nnlo-v2: new physics in Higgs Strahlung*, *JHEP* **05** (2018) 089, arXiv: [1802.04817 \[hep-ph\]](#).
- [80] O. Brein, A. Djouadi and R. Harlander, *NNLO QCD corrections to the Higgs-strahlung processes at hadron colliders*, *Phys. Lett. B* **579** (2004) 149, arXiv: [hep-ph/0307206](#).
- [81] O. Brein, R. Harlander, M. Wiesemann and T. Zirke, *Top-quark mediated effects in hadronic Higgs-Strahlung*, *Eur. Phys. J. C* **72** (2012) 1868, arXiv: [1111.0761 \[hep-ph\]](#).
- [82] L. Altenkamp, S. Dittmaier, R. V. Harlander, H. Rzehak and T. J. E. Zirke, *Gluon-induced Higgs-strahlung at next-to-leading order QCD*, *JHEP* **02** (2013) 078, arXiv: [1211.5015 \[hep-ph\]](#).
- [83] R. V. Harlander, A. Kulesza, V. Theeuwes and T. Zirke, *Soft gluon resummation for gluon-induced Higgs Strahlung*, *JHEP* **11** (2014) 082, arXiv: [1410.0217 \[hep-ph\]](#).
- [84] A. Denner, S. Dittmaier, S. Kallweit and A. Mück, *HAWK 2.0: A Monte Carlo program for Higgs production in vector-boson fusion and Higgs strahlung at hadron colliders*, *Comput. Phys. Commun.* **195** (2015) 161, arXiv: [1412.5390 \[hep-ph\]](#).
- [85] M. L. Ciccolini, S. Dittmaier and M. Krämer, *Electroweak radiative corrections to associated WH and ZH production at hadron colliders*, *Phys. Rev. D* **68** (2003) 073003, arXiv: [hep-ph/0306234 \[hep-ph\]](#).
- [86] W. Beenakker et al., *NLO QCD corrections to $t\bar{t}H$ production in hadron collisions*, *Nucl. Phys. B* **653** (2003) 151, arXiv: [hep-ph/0211352](#).
- [87] S. Dawson, C. Jackson, L. Orr, L. Reina and D. Wackerth, *Associated Higgs production with top quarks at the large hadron collider: NLO QCD corrections*, *Phys. Rev. D* **68** (2003) 034022, arXiv: [hep-ph/0305087](#).
- [88] Y. Zhang, W.-G. Ma, R.-Y. Zhang, C. Chen and L. Guo, *QCD NLO and EW NLO corrections to $t\bar{t}H$ production with top quark decays at hadron collider*, *Phys. Lett. B* **738** (2014) 1, arXiv: [1407.1110 \[hep-ph\]](#).
- [89] S. Frixione, V. Hirschi, D. Pagani, H.-S. Shao and M. Zaro, *Electroweak and QCD corrections to top-pair hadroproduction in association with heavy bosons*, *JHEP* **06** (2015) 184, arXiv: [1504.03446 \[hep-ph\]](#).
- [90] S. Dawson, C. Jackson, L. Reina and D. Wackerth, *Exclusive Higgs boson production with bottom quarks at hadron colliders*, *Phys. Rev. D* **69** (2004) 074027, arXiv: [hep-ph/0311067](#).
- [91] S. Dittmaier, M. Krämer and M. Spira, *Higgs radiation off bottom quarks at the Tevatron and the CERN LHC*, *Phys. Rev. D* **70** (2004) 074010, arXiv: [hep-ph/0309204](#).

- [92] R. Harlander, M. Krämer and M. Schumacher, *Bottom-quark associated Higgs-boson production: reconciling the four- and five-flavour scheme approach*, 2011, arXiv: [1112.3478 \[hep-ph\]](#).
- [93] F. Demartin, F. Maltoni, K. Mawatari and M. Zaro, *Higgs production in association with a single top quark at the LHC*, *Eur. Phys. J. C* **75** (2015) 267, arXiv: [1504.00611 \[hep-ph\]](#).
- [94] A. Djouadi, J. Kalinowski and M. Spira, *HDECAY: a program for Higgs boson decays in the Standard Model and its supersymmetric extension*, *Comput. Phys. Commun.* **108** (1998) 56, arXiv: [hep-ph/9704448](#).
- [95] M. Spira, *QCD Effects in Higgs Physics*, *Fortsch. Phys.* **46** (1998) 203, arXiv: [hep-ph/9705337](#).
- [96] A. Djouadi, M. M. Mühlleitner and M. Spira, *Decays of supersymmetric particles: The Program SUSY-HIT (SUSpect-SdecaY-Hdecay-InTerface)*, *Acta Phys. Polon. B* **38** (2007) 635, arXiv: [hep-ph/0609292](#).
- [97] A. Bredenstein, A. Denner, S. Dittmaier and M. M. Weber, *Radiative corrections to the semileptonic and hadronic Higgs-boson decays $H \rightarrow WW/ZZ \rightarrow 4$ fermions*, *JHEP* **02** (2007) 080, arXiv: [hep-ph/0611234](#).
- [98] A. Bredenstein, A. Denner, S. Dittmaier and M. M. Weber, *Precise predictions for the Higgs-boson decay $H \rightarrow WW/ZZ \rightarrow 4$ leptons*, *Phys. Rev. D* **74** (2006) 013004, arXiv: [hep-ph/0604011](#).
- [99] A. Bredenstein, A. Denner, S. Dittmaier and M. M. Weber, *Precision calculations for the Higgs decays $H \rightarrow ZZ/WW \rightarrow 4$ leptons*, *Nucl. Phys. Proc. Suppl.* **160** (2006) 131, arXiv: [hep-ph/0607060](#).
- [100] E. Bothmann et al., *Event generation with Sherpa 2.2*, *SciPost Phys.* **7** (2019) 034, arXiv: [1905.09127 \[hep-ph\]](#).
- [101] T. Gleisberg and S. Höche, *Comix, a new matrix element generator*, *JHEP* **12** (2008) 039, arXiv: [0808.3674 \[hep-ph\]](#).
- [102] F. Buccioni et al., *OpenLoops 2*, *Eur. Phys. J. C* **79** (2019) 866, arXiv: [1907.13071 \[hep-ph\]](#).
- [103] F. Cascioli, P. Maierhöfer and S. Pozzorini, *Scattering Amplitudes with Open Loops*, *Phys. Rev. Lett.* **108** (2012) 111601, arXiv: [1111.5206 \[hep-ph\]](#).
- [104] A. Denner, S. Dittmaier and L. Hofer, *COLLIER: A fortran-based complex one-loop library in extended regularizations*, *Comput. Phys. Commun.* **212** (2017) 220, arXiv: [1604.06792 \[hep-ph\]](#).
- [105] S. Schumann and F. Krauss, *A Parton shower algorithm based on Catani-Seymour dipole factorisation*, *JHEP* **03** (2008) 038, arXiv: [0709.1027 \[hep-ph\]](#).
- [106] S. Höche, F. Krauss, M. Schönherr and F. Siegert, *A critical appraisal of NLO+PS matching methods*, *JHEP* **09** (2012) 049, arXiv: [1111.1220 \[hep-ph\]](#).
- [107] S. Höche, F. Krauss, M. Schönherr and F. Siegert, *QCD matrix elements + parton showers: The NLO case*, *JHEP* **04** (2013) 027, arXiv: [1207.5030 \[hep-ph\]](#).
- [108] S. Catani, F. Krauss, B. R. Webber and R. Kuhn, *QCD Matrix Elements + Parton Showers*, *JHEP* **11** (2001) 063, arXiv: [hep-ph/0109231](#).

- [109] S. Höche, F. Krauss, S. Schumann and F. Siegert, *QCD matrix elements and truncated showers*, *JHEP* **05** (2009) 053, arXiv: [0903.1219 \[hep-ph\]](#).
- [110] F. Siegert, *A practical guide to event generation for prompt photon production with Sherpa*, *J. Phys. G* **44** (2017) 044007, arXiv: [1611.07226 \[hep-ph\]](#).
- [111] S. Frixione, *Isolated photons in perturbative QCD*, *Phys. Lett. B* **429** (1998) 369, arXiv: [hep-ph/9801442](#).
- [112] R. D. Ball et al., *Parton distributions for the LHC run II*, *JHEP* **04** (2015) 040, arXiv: [1410.8849 \[hep-ph\]](#).
- [113] R. D. Ball et al., *Parton distributions with LHC data*, *Nucl. Phys. B* **867** (2013) 244, arXiv: [1207.1303 \[hep-ph\]](#).
- [114] ATLAS Collaboration, *The Pythia 8 A3 tune description of ATLAS minimum bias and inelastic measurements incorporating the Donnachie–Landshoff diffractive model*, ATL-PHYS-PUB-2016-017, 2016, URL: <https://cds.cern.ch/record/2206965>.
- [115] ATLAS Collaboration, *The ATLAS Simulation Infrastructure*, *Eur. Phys. J. C* **70** (2010) 823, arXiv: [1005.4568 \[physics.ins-det\]](#).
- [116] GEANT4 Collaboration, S. Agostinelli et al., *GEANT4 – a simulation toolkit*, *Nucl. Instrum. Meth. A* **506** (2003) 250.
- [117] ATLAS Collaboration, *The simulation principle and performance of the ATLAS fast calorimeter simulation FastCaloSim*, ATL-PHYS-PUB-2010-013, 2010, URL: <https://cds.cern.ch/record/1300517>.
- [118] C. Anastasiou, R. Boughezal and F. Petriello, *Mixed QCD-electroweak corrections to Higgs boson production in gluon fusion*, *JHEP* **04** (2009) 003, arXiv: [0811.3458 \[hep-ph\]](#).
- [119] A. Denner, S. Dittmaier, S. Kallweit and A. Mück, *Electroweak corrections to Higgs-strahlung off W/Z bosons at the Tevatron and the LHC with HAWK*, *JHEP* **03** (2012) 075, arXiv: [1112.5142 \[hep-ph\]](#).
- [120] ATLAS Collaboration, *Electron and photon performance measurements with the ATLAS detector using the 2015–2017 LHC proton–proton collision data*, *JINST* **14** (2019) P12006, arXiv: [1908.00005 \[hep-ex\]](#).
- [121] M. Cacciari, G. P. Salam and G. Soyez, *The Catchment Area of Jets*, *JHEP* **04** (2008) 005, arXiv: [0802.1188 \[hep-ph\]](#).
- [122] M. Cacciari, G. P. Salam and S. Sapeta, *On the characterisation of the underlying event*, *JHEP* **04** (2010) 065, arXiv: [0912.4926 \[hep-ph\]](#).
- [123] ATLAS Collaboration, *Measurement of the photon identification efficiencies with the ATLAS detector using LHC Run-1 data*, *Eur. Phys. J. C* **76** (2016) 666, arXiv: [1606.01813 \[hep-ex\]](#).
- [124] ATLAS Collaboration, *Measurement of the inclusive isolated prompt photon cross section in pp collisions at $\sqrt{s} = 7$ TeV with the ATLAS detector*, *Phys. Rev. D* **83** (2011) 052005, arXiv: [1012.4389 \[hep-ex\]](#).
- [125] ATLAS Collaboration, *Reconstruction of primary vertices at the ATLAS experiment in Run 1 proton–proton collisions at the LHC*, *Eur. Phys. J. C* **77** (2017) 332, arXiv: [1611.10235 \[hep-ex\]](#).

- [126] ATLAS Collaboration, *Jet reconstruction and performance using particle flow with the ATLAS Detector*, *Eur. Phys. J. C* **77** (2017) 466, arXiv: [1703.10485 \[hep-ex\]](#).
- [127] ATLAS Collaboration, *Topological cell clustering in the ATLAS calorimeters and its performance in LHC Run 1*, *Eur. Phys. J. C* **77** (2017) 490, arXiv: [1603.02934 \[hep-ex\]](#).
- [128] M. Cacciari, G. P. Salam and G. Soyez, *The anti- k_t jet clustering algorithm*, *JHEP* **04** (2008) 063, arXiv: [0802.1189 \[hep-ph\]](#).
- [129] M. Cacciari, G. P. Salam and G. Soyez, *FastJet user manual*, *Eur. Phys. J. C* **72** (2012) 1896, arXiv: [1111.6097 \[hep-ph\]](#).
- [130] ATLAS Collaboration, *Jet energy scale and resolution measured in proton–proton collisions at $\sqrt{s} = 13$ TeV with the ATLAS detector*, *Eur. Phys. J. C* **81** (2020) 689, arXiv: [2007.02645 \[hep-ex\]](#).
- [131] ATLAS Collaboration, *Performance of pile-up mitigation techniques for jets in pp collisions at $\sqrt{s} = 8$ TeV using the ATLAS detector*, *Eur. Phys. J. C* **76** (2016) 581, arXiv: [1510.03823 \[hep-ex\]](#).
- [132] ATLAS Collaboration, *Forward jet vertex tagging using the particle flow algorithm*, ATL-PHYS-PUB-2019-026, 2019, URL: <https://cds.cern.ch/record/2683100>.
- [133] ATLAS Collaboration, *ATLAS b-jet identification performance and efficiency measurement with $t\bar{t}$ events in pp collisions at $\sqrt{s} = 13$ TeV*, *Eur. Phys. J. C* **79** (2019) 970, arXiv: [1907.05120 \[hep-ex\]](#).
- [134] ATLAS Collaboration, *Muon reconstruction and identification efficiency in ATLAS using the full Run 2 pp collision data set at $\sqrt{s} = 13$ TeV*, *Eur. Phys. J. C* **81** (2021) 578, arXiv: [2012.00578 \[hep-ex\]](#).
- [135] ATLAS Collaboration, *Performance of missing transverse momentum reconstruction with the ATLAS detector using proton–proton collisions at $\sqrt{s} = 13$ TeV*, *Eur. Phys. J. C* **78** (2018) 903, arXiv: [1802.08168 \[hep-ex\]](#).
- [136] ATLAS Collaboration, *Search for Higgs boson pair production in the two bottom quarks plus two photons final state in pp collisions at $\sqrt{s} = 13$ TeV with the ATLAS detector*, (), arXiv: [2112.11876 \[hep-ex\]](#).
- [137] G. Ke et al., ‘LightGBM: A Highly Efficient Gradient Boosting Decision Tree’, *Advances in Neural Information Processing Systems 30*, ed. by I. Guyon et al., Curran Associates, Inc., 2017 3146, URL: <http://papers.nips.cc/paper/6907-lightgbm-a-highly-efficient-gradient-boosting-decision-tree.pdf>.
- [138] D. V. Lindley, *On a Measure of the Information Provided by an Experiment*, *Ann. Math. Statist.* **27** (1956) 986.
- [139] G. Cowan, K. Cranmer, E. Gross and O. Vitells, *Asymptotic formulae for likelihood-based tests of new physics*, *Eur. Phys. J. C* **71** (2011) 1554, arXiv: [1007.1727 \[physics.data-an\]](#), Erratum: *Eur. Phys. J. C* **73** (2013) 2501.
- [140] J. Campbell, M. Carena, R. Harnik and Z. Liu, *Interference in the $gg \rightarrow h \rightarrow \gamma\gamma$ On-Shell Rate and the Higgs Boson Total Width*, *Phys. Rev. Lett.* **119** (2017) 181801, arXiv: [1704.08259 \[hep-ph\]](#), Erratum: *Phys. Rev. Lett.* **119** (2017) 181801.

- [141] L. J. Dixon and Y. Li, *Bounding the Higgs Boson Width Through Interferometry*, *Phys. Rev. Lett.* **111** (2013) 111802, arXiv: [1305.3854 \[hep-ph\]](#).
- [142] M. Oreglia, *A Study of the Reactions $\psi' \rightarrow \gamma\gamma\psi$, Appendix D*, (1980), URL: <https://www.slac.stanford.edu/cgi-bin/getdoc/slac-r-236.pdf>.
- [143] ATLAS Collaboration, *Search for Scalar Diphoton Resonances in the Mass Range 65–600 GeV with the ATLAS Detector in pp Collision Data at $\sqrt{s} = 8$ TeV*, *Phys. Rev. Lett.* **113** (2014) 171801, arXiv: [1407.6583 \[hep-ex\]](#).
- [144] ATLAS Collaboration, *Measurement of the production cross section of pairs of isolated photons in pp collisions at 13 TeV with the ATLAS detector*, *JHEP* **11** (2021) 169, arXiv: [2107.09330 \[hep-ex\]](#).
- [145] Bernstein, S., *Démonstration du Théorème de Weierstrass fondée sur le calcul des Probabilités*, *Comm. Soc. Math. Kharkov* **13** (1912) 1.
- [146] A. Wald, *Sequential Tests of Statistical Hypotheses*, *Ann. Math. Stat.* **16** (1945) 117.
- [147] ATLAS Collaboration, *Measurement of the Inelastic Proton–Proton Cross Section at $\sqrt{s} = 13$ TeV with the ATLAS Detector at the LHC*, *Phys. Rev. Lett.* **117** (2016) 182002, arXiv: [1606.02625 \[hep-ex\]](#).
- [148] X. Liu and F. Petriello, *Reducing theoretical uncertainties for exclusive Higgs-boson plus one-jet production at the LHC*, *Phys. Rev. D* **87** (2013) 094027, arXiv: [1303.4405 \[hep-ph\]](#).
- [149] I. W. Stewart, F. J. Tackmann, J. R. Walsh and S. Zuberi, *Jet p_T Resummation in Higgs Production at NNLL' + NNLO*, *Phys. Rev. D* **89** (2014) 054001, arXiv: [1307.1808 \[hep-ph\]](#).
- [150] R. Boughezal, X. Liu, F. Petriello, F. J. Tackmann and J. R. Walsh, *Combining resummed Higgs predictions across jet bins*, *Phys. Rev. D* **89** (2014) 074044, arXiv: [1312.4535 \[hep-ph\]](#).
- [151] I. W. Stewart and F. J. Tackmann, *Theory uncertainties for Higgs and other searches using jet bins*, *Phys. Rev. D* **85** (2012) 034011, arXiv: [1107.2117 \[hep-ph\]](#).
- [152] S. Gangal and F. J. Tackmann, *Next-to-leading-order uncertainties in Higgs+2 jets from gluon fusion*, *Phys. Rev. D* **87** (2013) 093008, arXiv: [1302.5437 \[hep-ph\]](#).
- [153] ATLAS Collaboration, *Measurements of the Higgs boson inclusive and differential fiducial cross sections in the 4ℓ decay channel at $\sqrt{s} = 13$ TeV*, *Eur. Phys. J. C* **80** (2020) 942, arXiv: [2004.03969 \[hep-ex\]](#).
- [154] ATLAS Collaboration, *Measurements of fiducial cross-sections for $t\bar{t}$ production with one or two additional b -jets in pp collisions at $\sqrt{s} = 8$ TeV using the ATLAS detector*, *Eur. Phys. J. C* **76** (2016) 11, arXiv: [1508.06868 \[hep-ex\]](#).
- [155] ATLAS Collaboration, *Measurements of the production cross-section for a Z boson in association with b -jets in proton–proton collisions at $\sqrt{s} = 13$ TeV with the ATLAS detector*, *JHEP* **07** (2020) 044, arXiv: [2003.11960 \[hep-ex\]](#).
- [156] ATLAS Collaboration, *Measurement of the cross-section for W boson production in association with b -jets in pp collisions at $\sqrt{s} = 7$ TeV with the ATLAS detector*, *JHEP* **06** (2013) 084, arXiv: [1302.2929 \[hep-ex\]](#).

- [157] The ATLAS and CMS Collaborations and The LHC Higgs Combination Group, *Procedure for the LHC Higgs boson search combination in Summer 2011*, tech. rep., CERN, 2011, URL: <http://cds.cern.ch/record/1379837>.
- [158] G. Bohm and G. Zech, *Introduction to statistics and data analysis for physicists*, DESY, 2010, ISBN: 9783935702416, URL: http://www-library.desy.de/preparch/books/vstatmp_engl.pdf.
- [159] A. L. Read, *Presentation of search results: the CL_S technique*, *J. Phys. G* **28** (2002) 2693.
- [160] I. Brivio, Y. Jiang and M. Trott, *The SMEFTsim package, theory and tools*, *JHEP* **12** (2017) 070, arXiv: [1709.06492](https://arxiv.org/abs/1709.06492) [[hep-ph](#)].
- [161] C. Degrande et al., *Automated one-loop computations in the standard model effective field theory*, *Phys. Rev. D* **103** (2021) 096024, arXiv: [2008.11743](https://arxiv.org/abs/2008.11743) [[hep-ph](#)].
- [162] *STXS Classification package*, URL: <https://gitlab.cern.ch/LHCHIGGSXS/LHCHXSWG2/STXS/Classification>.
- [163] S. Dawson and P. P. Giardino, *Electroweak corrections to Higgs boson decays to $\gamma\gamma$ and W^+W^- in standard model EFT*, *Phys. Rev. D* **98** (2018) 095005, arXiv: [1807.11504](https://arxiv.org/abs/1807.11504) [[hep-ph](#)].
- [164] J. R. Andersen et al., *Handbook of LHC Higgs Cross Sections: 3. Higgs Properties*, (2013), ed. by S. Heinemeyer, C. Mariotti, G. Passarino and R. Tanaka, arXiv: [1307.1347](https://arxiv.org/abs/1307.1347) [[hep-ph](#)].
- [165] ATLAS and CMS Collaborations, *Measurements of the Higgs boson production and decay rates and constraints on its couplings from a combined ATLAS and CMS analysis of the LHC pp collision data at $\sqrt{s} = 7$ and 8 TeV*, *JHEP* **08** (2016) 045, arXiv: [1606.02266](https://arxiv.org/abs/1606.02266) [[hep-ex](#)].